DYNAMIC PROPERTIES OF CARBONATES AND APPLICATIONS TO CRATERING PROCESSES

Thesis by

Joana Marija Vizgirda

In Partial Fulfillment of the Requirements

for the Degree of

Doctor of Philosophy

California Institute of Technology

Pasadena, California

1982

(Submitted June 5, 1981)

ACKNOWLEDGEMENTS

I express my appreciation to Thomas J. Ahrens for providing unique opportunities for carrying out this research, and for his continual interest and support. For his whole-hearted concern and encouragement, I sincerely thank Pol Duwez.

I owe thanks to many Division faculty members, especially George Rossman for his helpful advice and Heinz Lowenstam for his boundless enthusiasm. For the many pleasant, profitable and inspiring interactions with members of the shock wave group, in particular, Mark Boslough, Ken-ichi Kondo, and J. Peter Watt, I am extremely grateful. The experiments presented here were made possible by the expert assistance of past and present members of the shock lab - Warren Ginn, Jim Long, Mike Long, Chuck Manning and Ron Smith. I especially thank Epaprodito Gelle for his reliable, meticulous and diligent assistance throughout the entire period of my research. Mickey McConnell has been of enormous help in many ways - careful sample preparation, efficient thesis typing, and patience, understanding and cheerful good humor, even under pressure.

This project was initiated with the help of Byron Ristvet, who has provided continuing and valuable advice and assistance. I thank Jay Melosh for his interest in the progress of this work and for many helpful discussions. Many interesting discussions with Robert Couch and David Roddy are much appreciated. Fred Tsay assisted with the ESR study and Sunney Chan provided ESR facilities. I thank Joe Wysocki for his expert help with the X-ray portion of this work.

The Defense Nuclear Agency and the National Aeronautics and Space

Administration are acknowledged for providing financial support.

ABSTRACT

The response of carbonate minerals and rocks under shock compression is investigated using equation of state, shock metamorphism, and crater morphology studies. Coralline limestone samples from Cactus Crater, a nuclear explosion crater on Runit Island in Eniwetok Atoll, are used in the investigations of shock deformation as well as the crater structural study. Carbonate minerals and rocks shocked in the laboratory to known dynamic stress levels are used to calibrate shock pressures in the Cactus samples.

Very low shock pressure deformation effects are detected in the explosively and laboratory shocked samples by two bulk sample techniques: electron spin resonance (ESR) and powder X-ray diffraction. According to ESR studies on calcite from Cactus Crater samples, peak shock pressures of 4.5 ± 0.5 GPa were experienced by the material beneath the crater. Aragonite peak broadening analyses of powder X-ray diffraction spectra allows differentiation between two modes of material deformation, mosaicism (or reduction of crystallite size) and strain; both of these effects are detected in Cactus and in laboratory shocked samples. According to the X-ray analysis, peak pressures of 3 ± 1.5 GPa were experienced by the Cactus samples. A phase transition model, based on the variation of mosaicism and strain effects with shock pressure, is proposed. According to this model, residual strain in aragonite increases (crystallite size remaining approximately the same) until a threshold pressure of 8 to 10 GPa, corresponding to a phase transition, is reached; release from shock states above this pressure results in a discontinuous decrease in crystallite size and strain.

The diagenetic high to low magnesium calcite transition boundary occurring in the immediate subsurface of Runit Island is used as a stratigraphic tracer to determine structural features beneath Cactus Crater, including the amount of permanent downward displacement, the presence of a 10 m thick breccia lens which is disturbed and extensively mixed in-situ, and a possible central uplift feature. Applying the Bingham plastic model to Cactus Crater gives a yield strength of approximately 1 bar for the shock-wave engulfed limestone rock; this value is similar to the yield strength of many clays, and suggests a partially liquefied state for the water-saturated limestone immediately after passage of the shock wave.

The first aragonite Hugoniot equation of state data are presented. A Hugoniot elastic limit at 2.5±0.8 GPa and a phase transition at 6.5±1.5 GPa are observed. Above 10 GPa, the aragonite and calcite Hugoniots are approximately coincident, suggesting the transformation of both $CaCO_3$ polymorphs to the same high pressure phase. Release adiabats centered at shock pressures above 18 GPa yield pressure-density isentropes which suggest possible dissociation, i.e. CO_2 release, during the decompression process. These experimental data disagree with theoretical calculations, which predict incipient vaporization upon release from shock pressures of 55 and 33 GPa on the aragonite and calcite Hugoniots, respectively. Results from release adiabat experiments on calcite agree with the aragonite data and suggest vaporization upon unloading from shock pressures of approximately 37 GPa; a mass balance calculation using the experimental calcite release paths indicates that 45% of the $CaCO_3$ has dissociated upon release to 0.2 GPa pressures.

TABLE OF CONTENTS

Chapter 1

INTRODUCTION

In order to thoroughly understand the nature of meteorite impact and explosion processes on the Earth's surface, a fundamental comprehension of the behaviour of minerals and rocks under shock compression is needed. Although natural impacts have occurred indiscriminately with respect to target surface lithology, cratering studies have concentrated on impacts formed in silicate rocks, particularly those of igneous origin. Few studies have considered clastic sedimentary and carbonate rocks as target media for impact processes, and, in particular, there are very few investigations of shock metamorphism of porous and water-saturated rocks. This thesis addresses the problem of shock behaviour of carbonate minerals and impact mechanics of carbonate rocks. The approach used involves investigations of carbonate shock metamorphism and equations of state, and studies of carbonate crater morphology.

Motivation for this study is provided by the numerous natural craters occurring in carbonate rocks; of over 90 sites with either associated meteorite fragments or evidence of impact metamorphism, approximately 30 are entirely or partly in carbonate rocks (Dence, 1972; Grieve and Robertson, 1979). Although they share many features with craters in crystalline terrain, such as

raised rims, central peaks, breccia lenses, etc., craters in carbonate (and sedimentary in general) rocks differ in several aspects, notably, in their lack of impact melts (Kieffer and Simonds,1980). Shatter cones, radially striated conical fracture surfaces diagnostic of impact structures, are particularly abundant and display especially well-defined striations in dense, fine-grained carbonate rocks (Milton, 1977); it is not yet understood, however, how these features are formed. Although shock metamorphic features such as anomalous extinction, microfractures, and shock-induced twinning, have been documented in carbonate minerals from Flynn Creek and Wells Creek Craters in Tennessee and West Hawk Lake Crater in Manitoba (Roddy, 1968; Short and Bunch, 1968), no systematic studies of these features have been carried out. Also, shock induced plastic deformation, as indicated by asterism and line-broadening in Debye-Scherrer X-ray patterns of calcite and dolomite crystals, has been observed in samples from Wells Creek, Sierra Madera (Texas), Steinheim (Germany) and Decaturville (Missouri) structures (Dachille et al., 1968). Such observations on shocked carbonate materials are, however, infrequent. They are also almost entirely qualitative; no empirical correlation scheme linking observable deformation features with shock pressures had previously been devised.

The dominant obstacle in shock deformation studies is that of preservation, or rather lack of it. Because carbonate minerals readily dissolve and recrystallize, the likelihood of observing shock features increases with decreasing age of the crater. Fortunately, there exist several very recent explosion craters in

carbonate rocks, produced during the nuclear testing program conducted by the United States in the 1950's at the Pacific atolls of Eniwetok and Bikini. These craters provide another advantage, in that their approximate energies of formation are known, thus providing constraints on the pressure levels deduced from shock metamorphism studies of samples from the testing sites.

Cactus Crater, one of the smallest of the explosion craters formed in the testing program, is the object of several chapters of this thesis, and will briefly be introduced here. Cactus is located on the northern corner of Runit Island, one of the windward islands of Eniwetok, a South Pacific atoll situated approximately half-way between New Guinea and the Hawaiian Islands. It was formed May 6, 1958 by an 18 kiloton nuclear explosion detonated 0.9 m above mean sea level. It has a diameter of 105.5 m and a central depth relative to mean sea level of 10.4 m. Geologic and geophysical investigations of Cactus Crater were conducted in 1973-1974 during Project EXPOE, and included drilling operations, seismic studies, aerial photography, and topographic surveying. Overland boreholes were drilled parallel and orthogonal to the elongated outline of Runit Island, and two overwater drilling operations were conducted inside the crater itself. The geology of Runit Island is characterized by nearly 1400 m of coralline limestone deposited since Eocene time on a subsiding volcanic base. Details of the geology are presented where such information is needed, particularly in Chapters 3 and 5. For a more detailed description, see Ristvet et al., (1978).

Cactus Crater samples are used in electron spin resonance (on

calcite) and powder X-ray diffraction (on aragonite) studies discussed in Chapters 3 and 4, respectively. Both these investigative techniques offer the advantage of being easily applied to the very fine-grained, generally unwieldly Cactus coral samples. In addition, being bulk sample methods, they provide statistically valid estimates of average pressures experienced by the material. Estimates obtained from, say, microscopic observation of deformation features in several grains can misrepresent shock pressure histories. Coral samples shocked in the laboratory to known pressure levels are used to calibrate the explosively deformed samples. Using the electron spin resonance, or ESR, technique, which is more sensitive to low deformation stresses, peak pressures of 4.5 ± 0.5 GPa are estimated for the most heavily shocked Cactus samples. Although the powder X-ray diffraction method does not provide the resolution in permanent strain and, hence, in pressure calibration afforded by ESR, it offers some physical insight into the nature of the shock deformation recorded in minerals, specifically in aragonite. In particular, it distinguishes between mosaicism and strain effects, and, by recording their variation with pressure, suggests an aragonite phase transition occurring between $\sim$8 and $\sim$10 GPa. Using this technique, peak pressures of 3 ± 1.5 GPa are estimated for the Cactus samples. Thus, using two different techniques on two different Cactus sample minerals, a satisfactory agreement in estimated peak shock pressures is achieved.

Cactus Crater is also the object of the morphologic study presented in Chapter 5. The fortuitous occurrence of the high to

low magnesium calcite diagenetic transition boundary in the immediate subsurface of the cratered vicinity allows definition, or, at least, the strong suggestion, of the following structural features: depression beneath the crater, a 10 m thick breccia lens fractured and mixed in situ, and a central uplift. The observations of vigorous mixing of the breccia lens and complex crater morphologic features are unexpected in a crater as small as Cactus, and suggest that substrate lithology is a critical determining factor in the cratering process.

The first Hugoniot equation of state data for aragonite shocked to 40 GPa are presented in this thesis. The low pressure part of the shock compression curve is similar to that of calcite, both in the low value of its Hugoniot elastic limit ($\sim$2 GPa) and in the existence of phase transitions; at least one, and possibly two transitions occur at pressures below 10 GPa on the aragonite Hugoniot. Thus the equation of state data support the phase changes speculated on the basis of X-ray powder diffraction analysis in Chapter 4. Above 10 GPa, the calcite and aragonite Hugoniots are indistinguishable, suggesting transformations of both polymorphs to the same high pressure phase. The very shallow release adiabats above 18 GPa suggest partial vaporization occurring upon release from these Hugoniot pressures. According to theoretical calculations, however, incipient vaporization does not occur until Hugoniot pressures of 55 GPa. The calcite release adiabat investigation, presented in Chapter 7, is motivated by these provocative aragonite results, and serves, in fact, to support partial vaporization of carbonate minerals upon release

from below theoretically predicted Hugoniot pressures. Such vapor production at relatively low pressures certainly has an effect on impact and explosion cratering processes, and may help to explain the turbulent nature of the structural deformation of Cactus Crater described in Chapter 5. In addition, these release adiabat results have potential (not exploited here) for use in models of atmospheric evolution by impact induced volatile production.

Apart from their contribution to the impact and explosion cratering problem, several topics presented in this thesis are of intrinsic mineralogical and sedimentological interest. The observation of low pressure phase transitions in aragonite, and the existence of analogous transitions (i.e. also low pressure) in calcite, together with the coincidence of the calcite and aragonite Hugoniots at higher pressures, suggests parallel evolution of these polymorphs to a common high pressure phase. Confirmation of such an evolutionary sequence, and determination of the detailed nature of these transitions await static high pressure investigations. The model proposed in Chapter 4, attributing the pattern of shock induced mosaicism and strain deformation to non-recoverable phase transitions undergone by aragonite at high pressures, suggests an intriguing potential for interactive shock equation of state and recovery studies of phase transitions. This model need not be limited to the $CaCO_3$ system, and, in fact, the X-ray technique may prove valuable in detecting non-recoverable phase transitions in many other minerals. The determination of the high to low Mg calcite transition (Chapter 5) as an abrupt discontinuity (outside the cratered area) was not an

intentional effort, but is an important contribution to the field of carbonate diagenesis. Also, the observed discrepancy between empirically and theoretically determined X-ray calibration curves for the high and low magnesium calcite concentrations suggests a fundamental difference in the crystal character of these two types of calcite, and merits further investigation.

The thesis consists of three basic parts: investigation of shock deformation effects in carbonate minerals and rocks (Chapters 3 and 4), a structural study of Cactus Crater (Chapter 5), and a Hugoniot equation of state study of the shock compression and isentropic release properties of aragonite and calcite (Chapters 6 and 7). Generally, these chapters can be considered self-contained. A brief introduction to basic shock wave physics is presented in Chapter 2, and most of the background material on Runit Island geology is contained in Chapter 3.

References

Dachille, F., P. Gigl and P. Y.Simons, Experimental and analytical studies of crystalline damage useful for the recognition of impact structures. In Shock Metamorphism of Natural Materials, eds. B. M. French and N. M. Short, pp. 555-569, Mono Book Corp., 1968.

Dence, M. R., The nature and significance of terrestrial impact structures, 24th Int. Geol. Congr. Sect. 15, 77-89, 1972.

Grieve, R.A.F. and P. B. Robertson, The terrestrial cratering record 1. Current status of observations, Icarus, 38, p. 212-229, 1979.

Kieffer, S. W. and C. H. Simonds, The role of volatiles in the impact cratering process, Rev. Geophys. and Space Phys., 18, 143-181, 1980.

Milton, D. J., Shatter cones - an outstanding problem in shock mechanics, In Impact and Explosion Cratering, eds. D. J. Roddy, R. O. Pepin, and R. B. Merrill, pp. 703-714, Pergamon Press, 1977.

Ristvet, B. L., E. L. Tremba, R. F. Couch, J. A. Fetzer, E. R. Goter, D. R. Walter and V. P. Wendland, Geologic and Geophysical Investigations of the Eniwetok Nuclear Craters, Air Force Weapons Laboratory, Final Report, 1978.

Roddy, D. J., The Flynn Creek Crater, Tennessee, In Shock Metamorphism of Natural Materials, eds. B. M. French and N. M. Short, pp. 291-322, Mono Book Corp., 1968.

Short, N. M. and T. E. Bunch, A worldwide inventory of features characteristic of rocks associated with presumed meteorite impact structures, In Shock Metamorphism of Natural Materials, eds. B. M. French and N. M. Short, pp. 255-266, Mono Book Corp., 1968.

CHAPTER 2

BASIC PRINCIPLES OF SHOCK WAVES IN SOLIDS

In this chapter, a few of the basic principles of shock wave propagation in solid materials are introduced; emphasis is placed on concepts, such as two-wave structures and release adiabats, useful in the reading of future chapters. For a more thorough treatment of the subject, the reader is referred to such comprehensive works as Courant and Friedrichs (1948), Bradley (1962) and Zel'dovich and Raizer (1966).

The sudden acceleration of a solid material, either by a meteorite impact or by a chemical or nuclear explosion, produces a stress wave travelling at velocities greater than the bulk sound speed. Because the compressibility of a solid generally decreases with increasing pressure, this stress wave steepens to a shock front, or shock wave, which represents a discontinuity in the density, pressure and internal energy of the material. Although an idealized shock profile is sharply discontinuous, the actual profile is of a finite width, dependent on material viscosity and thermal conductivity. In addition to these effects, phase transitions and an overtaking rarefaction wave can complicate the shock profile. Because the sound velocity is greater in the compressed material behind the shock front, the rarefaction wave is able to travel faster than the shock wave and thus overtake it. Fig. 2-1 diagramatically depicts a simplified shock front, i.e., without phase transition and rarefaction wave effects, in the distance-pressure plane.

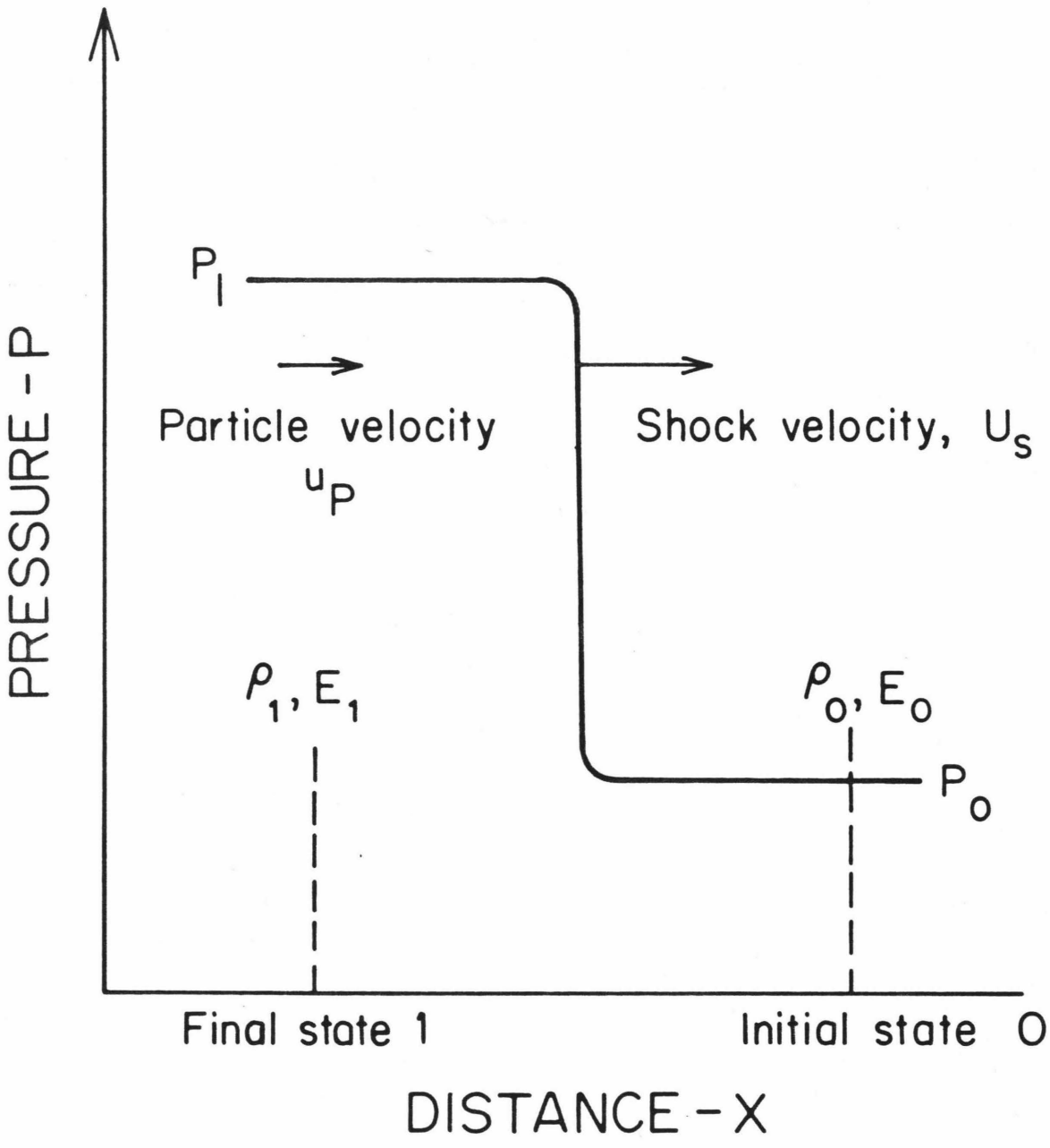

Figure 2-1. Schematic profile of a steady shock wave traveling at velocity U_s into material with an initial state, ρ_o, P_o and E_o, and raising it to a final state, ρ_1, P_1 and E_1, with a particle velocity, u_p.

For practical experimental purposes, the shock front is considered to be a steady surface of discontinuity between a uniform, unshocked and a uniform, shocked state. Assuming that the material behind the shock front behaves hydrodynamically, the conservation equations of mass, momentum and energy can be applied, allowing determination of the density, pressure and internal energy state behind the shock front. In Fig. 2-1, consider a material initially at rest with a density, pressure and internal energy of ρ_o, P_o and E_o, respectively. Passage of a shock wave with a velocity U_s accelerates the material to a particle velocity u_p and raises the initial condition to ρ_1, P_1 and E_1 according to the equations:

of conservation of mass: $$\rho_o U_s = \rho_1 (U_s - u_p) \tag{2-1}$$

momentum: $$P_1 - P_o = \rho_o U_s u_p \tag{2-2}$$

and energy: $$P_1 u_p = \frac{1}{2} \rho_o U_s u_p^2 + \rho_o U_s (E_1 - E_o) \tag{2-3}$$

Since the initial conditions, ρ_o, P_o and E_o, are generally known, determining any two of the five parameters applicable to the final state allows a complete characterization of that state. Rearranging and combining Eqs. (2-1) to (2-3), leads to the familiar Rankine-Hugoniot relations:

$$U_s = \sqrt{\frac{\rho_1 (P_1 - P_o)}{\rho_o (P_1 - P_o)}} \tag{2-4}$$

$$u_p = \sqrt{(P_1 - P_o)\left(\frac{1}{\rho_o} - \frac{1}{\rho_1}\right)} \tag{2-5}$$

$$E_1 - E_o = \frac{1}{2} (P_o + P_1) \left(\frac{1}{\rho_o} - \frac{1}{\rho_1}\right) \qquad (2\text{-}6)$$

The locus of pressure-density (or pressure-volume) states achieved by shock compression of a particular material is referred to as the Hugoniot of that material. Although the shock compression process is adiabatic, it involves irreversible work and is, therefore non-isentropic. A hypothetical Hugoniot curve is compared to two other hypothetical compression curves (the isentrope and the isotherm) in Fig. 2-2. In this figure, the thermodynamic path of a material shock compressed to a density ρ_1 is represented by a line connecting the initial and final states, called the Rayleigh line; the triangular shaded area beneath the Rayleigh line represents the internal energy increase due to shock compression, given by Eq. (2-6). Clearly, this internal energy rise is greater than that incurred during the other compressive paths, as represented by the area,

$$\int P dV \text{ (or } -\int \frac{P}{\rho^2} d\rho),$$

under either the isentrope or the isotherm. The larger amount of irreversible heating during the shock process results in less compression along the Hugoniot relative to the other compression curves, at the same pressure.

The hydrodynamic shock compression model discussed in the previous paragraphs is strictly true only at high pressures, where material is characterized by fluid behaviour. At lower pressures, material strength effects and phase transitions produce non-uniform conditions and complicate the shock front. The following treatment specifically

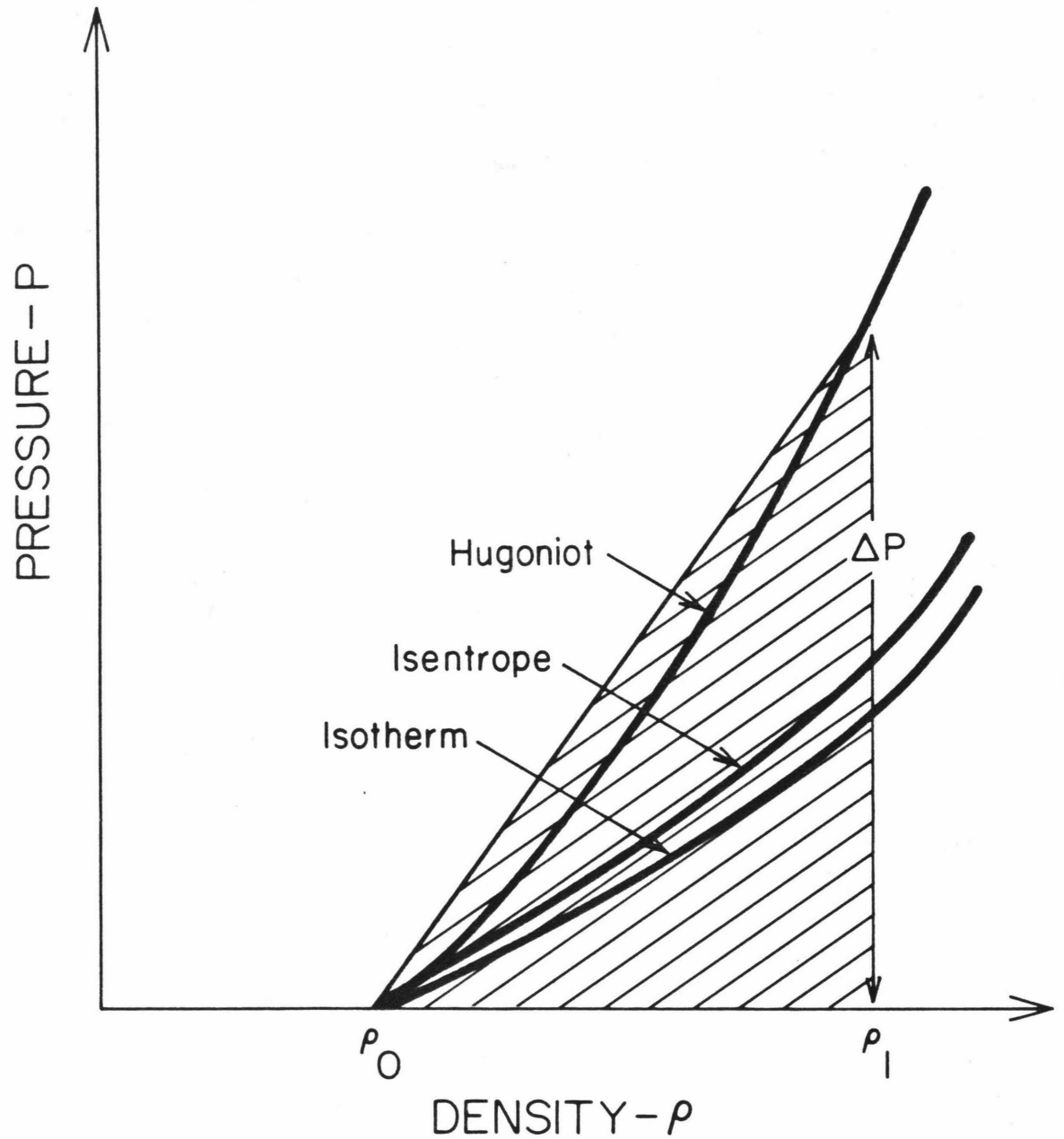

Figure 2-2. Diagram comparing shock Hugoniot with isothermal and isentropic compression curves. Shaded area represents internal energy increase due to shock compression: $\frac{1}{2}(\Delta P)(\frac{1}{\rho_o} - \frac{1}{\rho_1})$.

considers the elastic to plastic transition, but the derived instability condition also holds for phase transitions in the plastic regime. As depicted in Fig. 2-3, the elastic to plastic transition is characterized by a cusp in the Hugoniot separating the lower pressure elastic regime, governed by a linear stress-strain relationship, from the higher pressure plastic regime. This yield point is termed the Hugoniot elastic limit, or HEL. At pressures below the HEL, a single elastic wave is stable, and at pressures greater than P_2, i.e., at Hugoniot points joined by a single Rayleigh line, a single plastic wave is stable. For final peak pressures P_x, such that $P_1 < P_x < P_2$, both an elastic and a plastic wave are formed. In this region, the elastic wave travels with a velocity

$$\sqrt{\frac{\rho_1}{\rho_o}\frac{(P_1-P_o)}{(\rho_1-\rho_o)}} \quad ,$$

which is greater than

$$\sqrt{\frac{\rho_x}{\rho_1}\frac{(P_x-P_1)}{(\rho_x-\rho_1)}} \quad ,$$

the velocity of the plastic wave. Note that these velocities are proportional to the slope of the Rayleigh lines in the elastic and plastic regions. Thus, the condition for the instability of a single shock wave is:

$$\frac{\rho_x}{\rho_1}\frac{(P_x-P_1)}{(\rho_x-\rho_1)} < \frac{\rho_1}{\rho_o}\frac{(P_1-P_o)}{(\rho_1-\rho_o)} \qquad (2\text{-}7)$$

As mentioned earlier, this instability condition also holds for phase transitions.

The rarefaction process that brings shocked material back to ambient pressures is assumed to be both adiabatic and isentropic. A

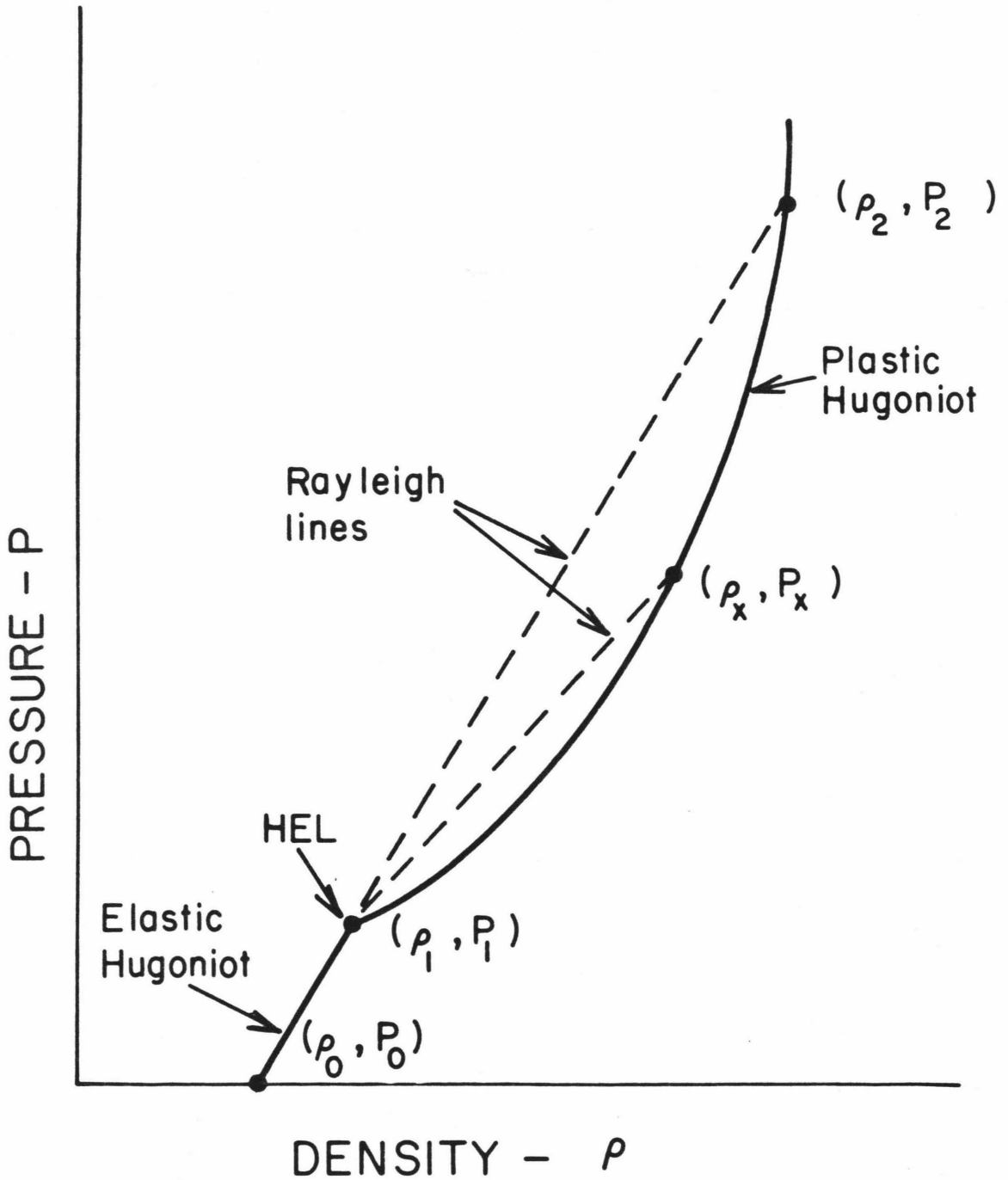

Figure 2-3. Characteristic Hugoniot of a material with a Hugoniot elastic limit, HEL. A two-wave structure will be observed for final pressures between P_1 and P_2.

variety of release paths are possible; three are schematically drawn in Fig. 2-4. Proceeding from right to left, i.e., from the steepest to the shallowest decompression path, the following phenomena are suggested by the release adiabats: complete retention of a shock-induced high pressure phase upon release to ambient pressures, retention of the high pressure phase along part of the release adiabat with reversion to a density lower than the starting zero-pressure density (possibly, in the case of silicates, indicating glass formation) upon complete release, and formation of a low density, possibly vapor-containing, phase along the entire release adiabat. The integral area, PdV, under these release adiabats represents energy taken up by the material upon expansion. The difference between this energy and that introduced upon shock compression (Eq. 2-6), is proportional to the post-shock temperature. Experimental determination of release adiabats is discussed in Ahrens et al. (1969); the method presented in that work is applied to release adiabat determinations for aragonite and calcite in Chapters 6 and 7.

The methods used in estimating temperatures along the Hugoniot, and entropies along the release adiabats are presented in Chapter 6, and will not be repeated here. Experimental details of recovery and equation of state experiments are described in Chapter 3 and Chapters 6 and 7, respectively; references to more detailed presentations of experimental methods are also cited in these chapters.

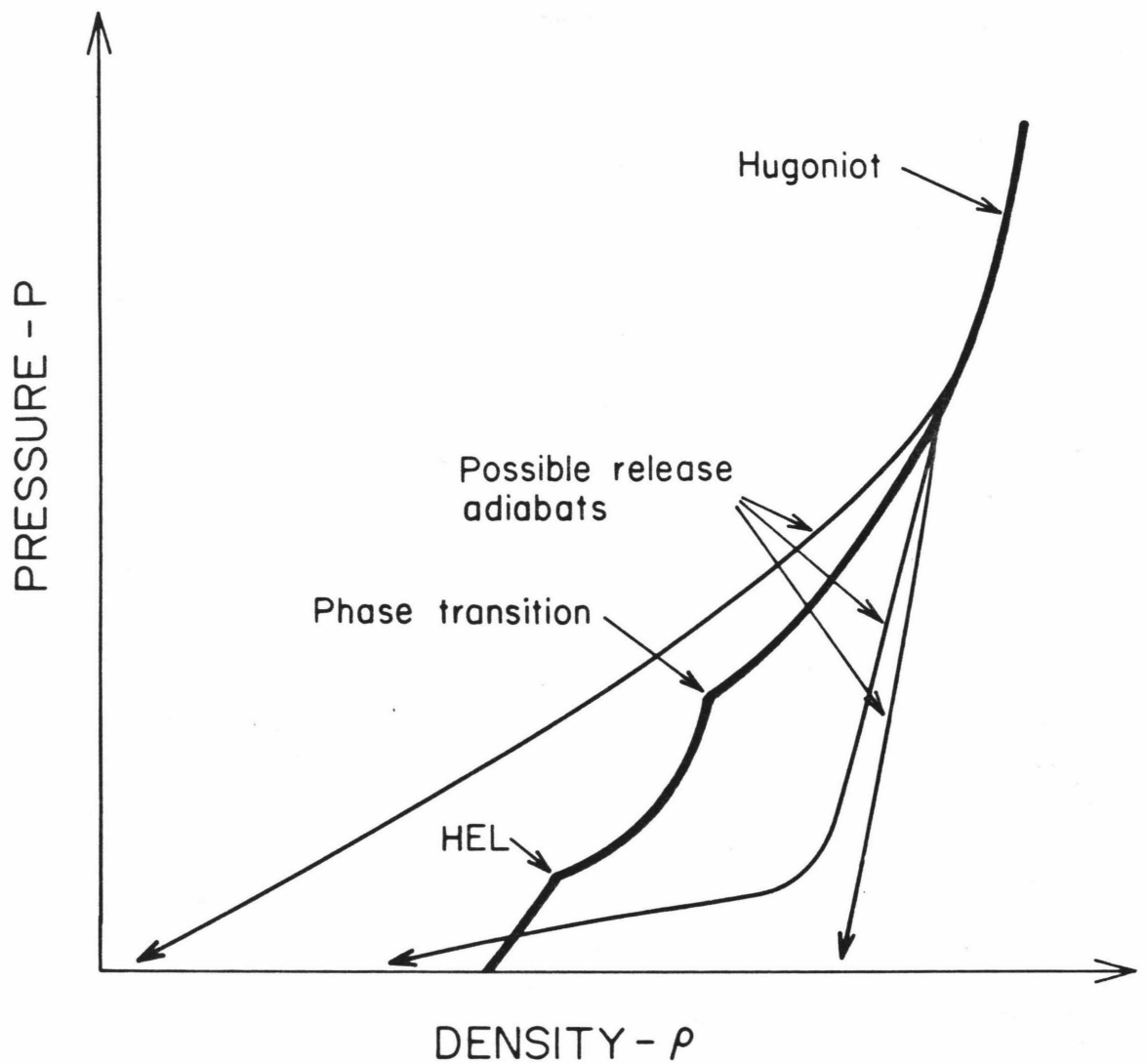

Figure 2-4. Characteristic Hugoniot of a material with both a Hugoniot elastic limit and a phase transition. Indicated possible release paths are discussed in the text.

References

Ahrens, T. J., C. F. Petersen and J. T. Rosenberg, Shock compression of feldspar, J. Geophys. Res., 74, 2727-2746, 1969.

Bradley, J. N., Shock Waves in Chemistry and Physics, Methuen and Co. Ltd., London, 1962.

Courant, R. and K. O. Friedrichs, Supersonic Flow and Shock Waves, Interscience, New York, 1948.

Zel'dovich, Y. B. and Y. P. Raizer, Physics of Shock Waves and High-Temperature Hydrodynamic Phenomena, Academic Press, New York, 1966.

Chapter 3

SHOCK DEFORMATION OF CALCITE FROM CACTUS CRATER: ESR STUDIES

Introduction

The unique difficulties associated with studies of shock metamorphism in carbonates, and specifically, in the very fine-grained Cactus Crater samples, prompt employment of equally unique investigative methods. The classical approach, involving optical microscopic observations of shock deformation effects, such as planar features and diaplectic glass, proved unproductive in the case of the Cactus samples for the following reasons: the extremely fine-grained coral material makes observation and identification of low shock pressure effects (such as planar features) a difficult and ambiguous venture, and higher shock pressure effects, such as diaplectic glass formation, may not be retained since $CaCO_3$ melts do not quench to a glass (Wyllie and Boettcher, 1969). Single crystal X-ray diffraction patterns of the shocked Cactus material, however, clearly showed residual deformation in both calcite and aragonite minerals (R. Couch, personal communication, 1978). What was needed, therefore, was a method not dependent on optically observable features, sufficiently sensitive to detect low (< 10 GPa) shock pressure metamorphism, and, preferably, applicable to bulk rather than single crystal samples. For these reasons, electron spin resonance, or ESR, was chosen as a potentially useful

technique.

Three previous investigations of shock effects in minerals using the ESR technique have been reported. Linde and De Carli (1969) report shock pressure induced changes in the radiation damage center ESR peak (i.e. the free electron signal) in shocked specimens of TiO_2. In dynamic compression experiments on single crystal MgO (Gager et al., 1964) and olivine (Ahrens, et al., 1976), variations in ESR spectral features of the shock-loaded samples are described and attributed to shock produced random orientation of Mn^{2+} centers, a trace constituent of both minerals. The Mn^{2+} ESR signal was detected in most Cactus samples (manganese being a common trace element of carbonate minerals) and a consistent spectral variation with core depth was observed. In an attempt to quantify this depth, and presumably shock pressure, related spectral variation, coral limestone samples were shock loaded in the laboratory to known stress levels. Electron spin resonance spectra of these experimentally shocked samples, as well as shocked single crystal calcite specimens, were then used to characterize the Cactus event as well as to gain a better understanding of shock induced effects in calcite in general.

Cactus Crater Geology and Sample Description

The geology beneath Runit Island, as determined from Project EXPOE, (see Chapter 1) drilling operations, consists, in general, of all-carbonate back-reef and lagoonal deposits, increasing in degree of cementation at deeper levels and recording 4 solution unconformities, correlative with discontinuities recognized throughout Eniwetok Atoll, above 60 m depth. Dating based on foraminiferal zones gives ages of

Recent to Upper Pleistocene (500,000 y.b.p.) to core samples from 0 to approximately 60 m depth.

The lithology of Runit core samples is dominated by uncemented to well-cemented grainstone; units of coral and coralgal boundstone are also present (classification scheme according to Dunham, 1962). The most common identifiable organic remains include corals, foraminifera, and algae, with trace pelecypod, gastropod and echinoderm fragments also in evidence. Detailed descriptions of Runit Island cores, as well as further information on the geology of Eniwetok Atoll can be found in Couch et al., 1975 and Ristvet et al., 1978.

The chemistry and composition of XC-1 (the core drilled at the center of Cactus Crater) samples were examined in further detail. X-ray diffractometer spectra show only the presence of calcite and aragonite. The aragonite concentration, as determined from measurements of relative peak heights and an empirically derived curve relating peak height to mole % aragonite, varies irregularly from 13% to 98% through the section. Manganese concentrations were determined via atomic absorption (AA) analysis and range from 0.0017 to less than 0.0002 weight %; as demonstrated by the values listed in Table 3-1 there is no correlation of manganese content with core depth. Iron concentrations, also determined via AA, ranged unsystematically from 0.084 to less than 0.005 weight % (see Table 3-1). Micrographs and SEM photos taken of upper XC-1 core levels (above approximately 15 m) display sub-angular void outlines and extreme fragmentation of mineral grains. (See Fig. 3-1, an SEM photo of an XC-1 sample from 11.1m depth.) However, calcite overgrowths and cavity infillings indicative of cementation processes

Table 3-1

ATOMIC ABSORPTION ANALYSES[a]

XC-1 Sample Depth (m)	Mn (weight %)	Fe (weight %)
11.1	0.0002	0.008
12.2	0.0014	0.038
∿13.6	0.0011	<0.005
19.2	<0.0002	<0.005
∿27.1	0.0011	0.021
29.7	0.0017	0.038
34.1	0.0003	0.022
35.4	0.0002	0.009
37.5	<0.0002	0.022
40.8	0.0007	0.084
41.8	0.0002	0.012
43.3	0.0003	0.025
45.4	<0.0002	<0.005

(a) Analyses by R. Haack, Jet Propulsion Laboratory

Figure 3-1. SEM photo of 11.1 m sample from central Cactus Crater core (XC-1) showing fine-grained fragmented nature of the material. Scale bar is 1µ.

are not observed in these samples. It is therefore concluded that significant $CaCO_3$ solution and re-deposition did not occur in these upper levels following the nuclear test and that the ESR data reflect features of calcite crystals deposited before and mechanically affected by the explosion.

Shock Experiments

Laboratory shock recovery experiments were performed on previously unshocked samples taken from the 3 m level of XRU-3, a drill core taken approximately 130 m from the edge of Cactus Crater. A well cemented, foraminiferal-red algal grainstone makes up this portion of the core. It is also the lithology comprising the uppermost level of XRU-1, located just outside Cactus Crater (Fig. 3-2); although it is not observed at the top of the XC-1 core, this rock type was probably present in the immediate subsurface of the ground zero point.

Density determinations were performed on a series of rectangular slabs (lateral dimensions 20-29 mm, thickness 3-13 mm) cut from the XRU-3 3 m core section. Details of the weighing procedure are given in Ahrens et al., (1977a). The measured bulk and "intrinsic" densities were 2.50 g/cc ± 0.05 and 2.71 g/cc ± 0.01, respectively. Since infilling of all pores and cracks with the solvent, toluene, is improbable, the latter measurements may be as much as 4% too low. An average, accessible porosity of 8% was determined from a comparison of bulk and "intrinsic" densities.

For the shock experiments, a series of coral samples, cored to a diameter of 16.4 mm and cut into pieces 5 to 7 mm long, were emplaced in either 2024 aluminum or high density polyethylene assemblies and machined

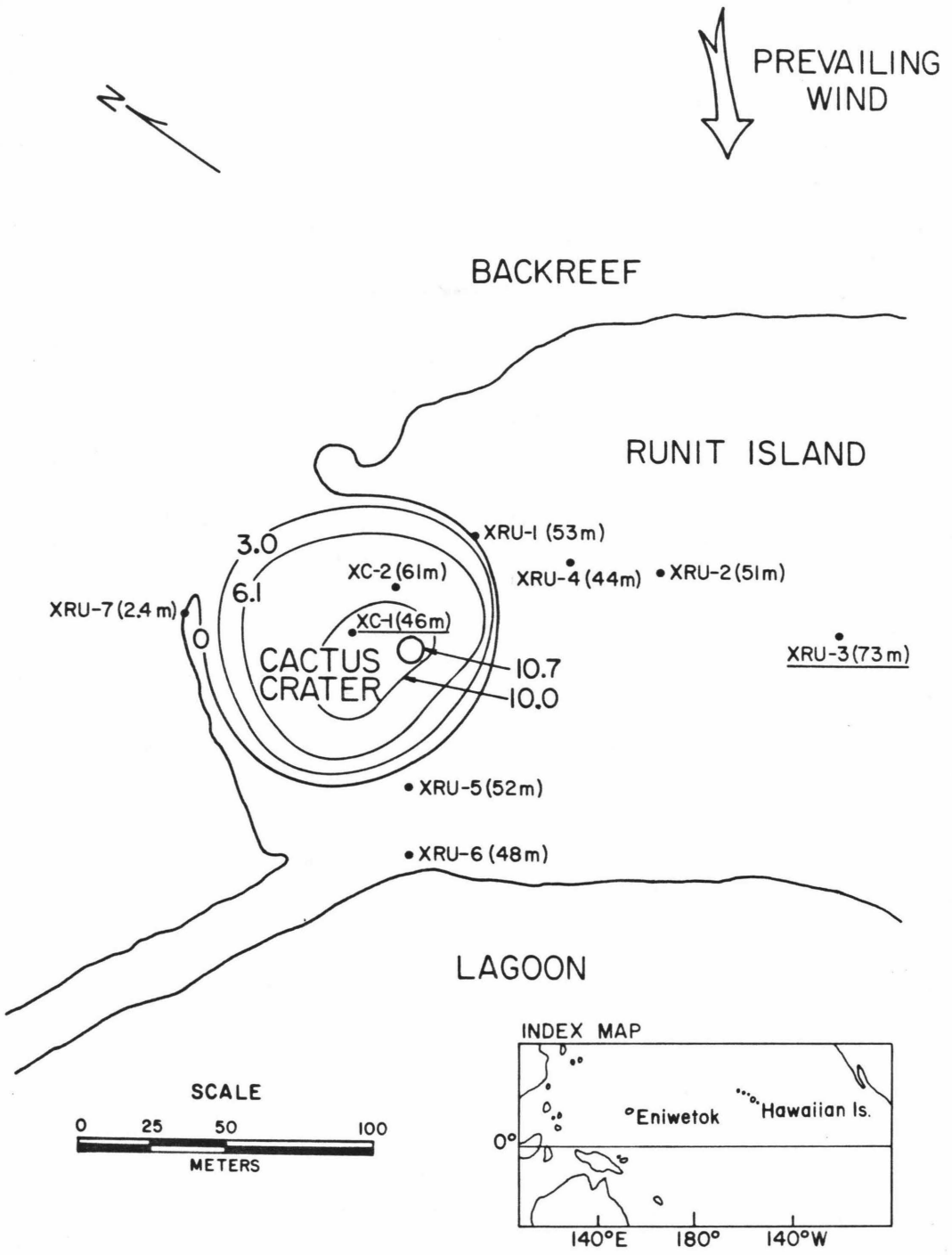

Figure 3-2. Map of northern Runit Island, Eniwetok Island (11.30°N, 162.15°E) showing the location of Cactus Crater and of Project EXPOE drillholes. Samples used in this study came from XC-1 and XRU-3. Post and pre-shot profiles were used to construct the Cactus Crater difference contour map; contour levels are indicated in meters.

flat with the container surface to a final thickness of 3 to 4 mm. Samples were then evacuated, saturated with water, and sealed to the 6 mm thick driver plate. The water saturation was done in order to simulate conditions present in the immediate subsurface of the test site. A diagram of the polyethylene assembly is seen in Fig. 3-3; the aluminum units, also sketched in Fig. 3-3, were slightly modified from the polyethylene design for easier machining.

A 40 mm propellant gun was used to accelerate lexan projectiles to velocities in the range of 0.08 to 1.53 km/sec. Lexan flyer plates, 6.3 mm thick, were used to impact samples in all high density polyethylene and in one aluminum assembly. 5 mm thick 2024 aluminum flyers were used with the remaining assemblies. Projectile velocities were measured using the time between interruption of three 0.5 mw He-Ne lasers positioned along the last 0.7 m of the projectile path. The impedance match technique (Stöffler, 1972), using projectile velocities and Hugoniot data (shock equation of state data relating pressure and density) for flyer, driver and sample materials allowed calculation of shock pressure in the sample.

For the experiments in which high density polyethylene (ρ_o = 0.96 g/cc) assemblies were used, sample Hugoniot states were determined using experimental data for lexan (Carter and Marsh, 1980) and high density polyethylene (ρ_o=0.954 g/cc; Carter and Marsh, 1980), and a calculated Hugoniot for water saturated coral. We assume that the individual components in a mixture are at the same pressure, and make use of the additivity rule to obtain the mixture density:

$$\rho^{-1}_{\text{mixture}} = m_1 \rho^{-1}_{H_2O} + m_2 \rho^{-1}_{CaCO_3} \qquad (3\text{-}1)$$

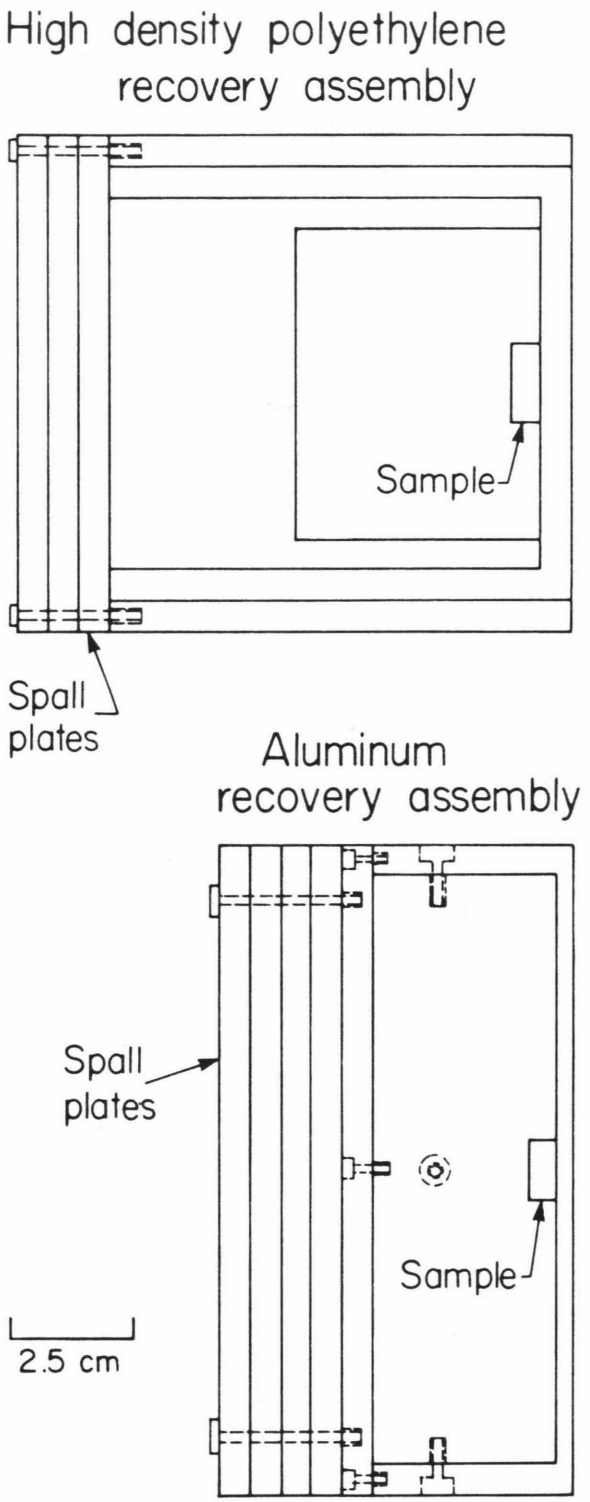

Figure 3-3. Cross section view of experimental assemblies used in shock recovery experiments on saturated coral samples. Both assembly types appear circular in plan view.

where m_1 and m_2 are the water and calcite weight fractions, respectively. The densities of water and calcite correspond to their Hugoniot densities. Mass fractions were determined from the measured average "accessible porosity" of 8%. The degree to which the above approximations are valid has been demonstrated by McQueen et al., (1970) and Al'tshuler and Sharipdzhanov (1971) in calculating silicate Hugoniots from their constituent oxides, and by Ahrens et al., (1977a) in constructing whole rock Hugoniots using data for constituent minerals. In their investigation of the calcite-water system, Kalashnikov et al., (1973) found good agreement between the dynamic adiabat calculated using Hugoniot data for calcite and water and Eq. 3-1, and experimental data in the pressure range of 5 to 65 GPa. An example of an impedance match solution using the calculated coral Hugoniot is illustrated in Fig. 3-4.

For experiments using a 2024 aluminum assembly, the final sample Hugoniot state was determined from an impedance match solution using the standard 2024 aluminum data given in McQueen et al., (1970) and flyer plate (either lexan or aluminum) Hugoniot data.

Experimental Results

Electron spin resonance powder spectra were obtained for coral and single crystal (originally) calcite samples. Details of the experimental method are given in Appendix I. A characteristic Mn^{2+} ESR signal centered at g = 2 (where g is the spectroscopic splitting factor) was detected in all single crystal calcite and most coral samples. Since aragonite does not show a Mn^{2+} ESR spectrum (Low and Zeira, 1972), the signal detected in the coral samples is due entirely to Mn^{2+} in calcite, which, in powder spectra, depicts Mn^{2+} occupying a single site. A

detailed explanation of the ESR spectrum of Mn^{2+} in calcite is also presented in Appendix I. Relevant features of the signal are illustrated in Fig. 3-5, a second derivative spectrum of a powder sample of unshocked calcite. The splitting of the six prominent hyperfine component peaks, labelled "central transitions" in the figure, is the feature observed to vary with shock pressure. These peaks correspond to the transitions, $M_s = +1/2 \leftrightarrow -1/2$ and $\Delta m_I = 0$, where M_s and m_I are the electron and nuclear spin quantum numbers, respectively, for Mn^{2+}, with M_s and m_I ranging from -5/2 to +5/2. The splitting amplitudes, $\Delta H(G)$, reported in Table 3-2 and used in calculating the zero-field splitting parameters, D, are measurements of the distance, in gauss, between the two sub-peaks of the highest field hyperfine component (the central transition peak on the far right in Fig. 3-5).

Of the 16 investigated Cactus Crater core (XC-1) samples, all but 3 gave a detectable ESR signal. The lack of signal in these 3 samples is probably due to insufficient Mn^{2+} concentrations, $<< 0.0002$ weight %, as determined by atomic absorption analyses (R. Haack, personal communication, 1978). For three of the samples, several aliquots were prepared and the spectra measured; in all cases, splitting values for the various aliquots of the same sample agreed to within less than 0.5 G. Consistent variations in spectral features from the top to the bottom of the core can be observed in Fig. 3-6. (These spectra were taken at a uniform 1 G modulation amplitude, therefore line shapes can be directly compared.) The lowest field Mn^{2+} hyperfine component (the left-hand arrow in the figure) is observed as a single peak in the 11.1 and 12.2 m samples; below this depth it is clearly split into two sub-peaks and

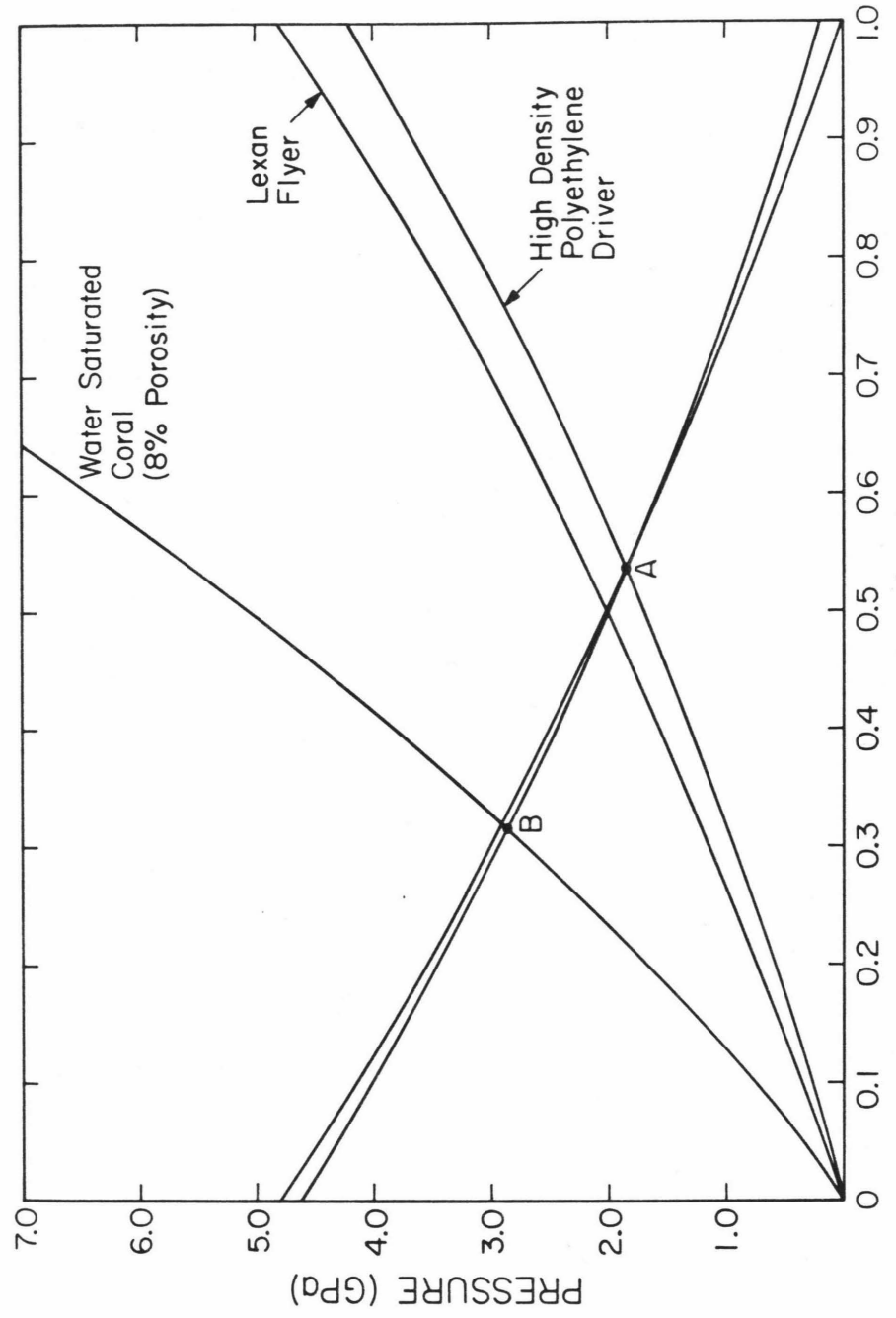

Figure 3-4. Graphical representation of shock pressure determination via the "impedance matching" method. In the example depicted, a lexan flyer plate at a free flight velocity of 1.0 km/sec impacts a high density polyethylene target containing a specimen of water saturated coral. A and B are the peak pressures attained in the polyethylene target and in the sample, respectively.

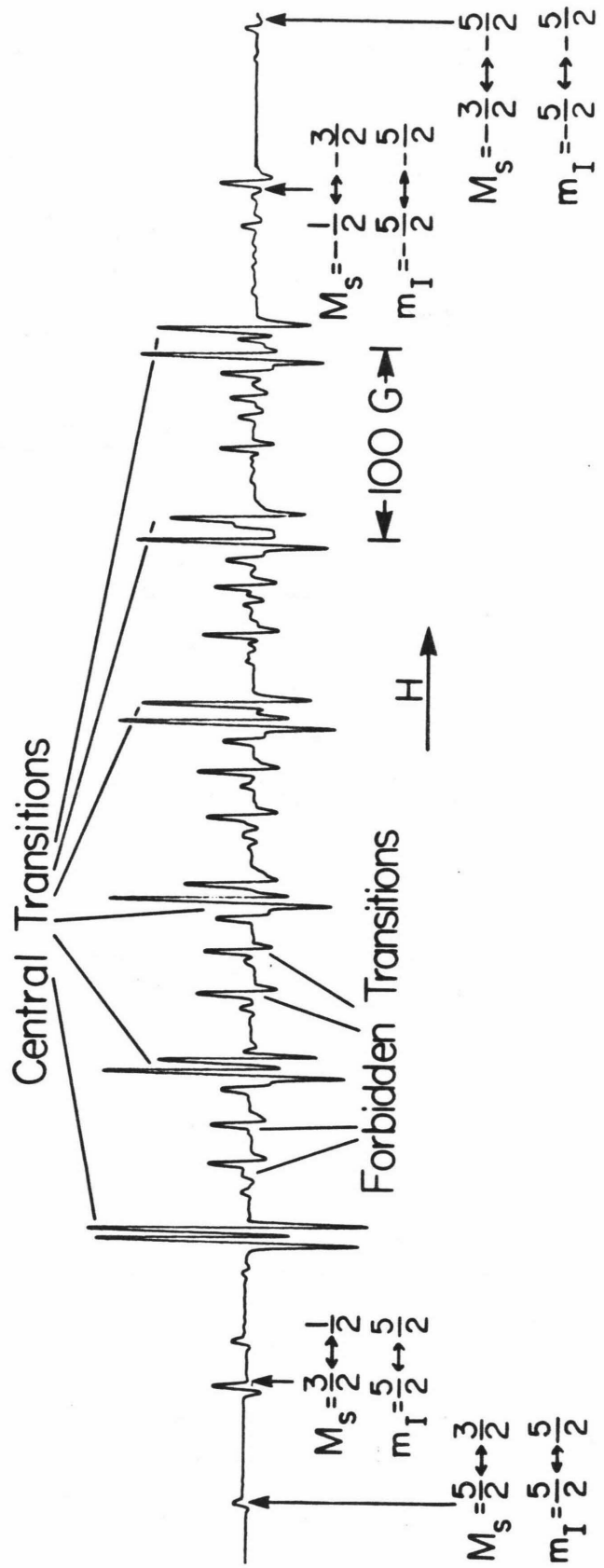

Figure 3-5. Second derivative spectrum of Mn^{2+} in a powder sample of unshocked calcite. The six prominent split peaks are the hyperfine components due to the central transitions, $M_S = +1/2 \leftrightarrow -1/2$, $\Delta m_I = 0$; the intervening lower intensity absorptions are due to forbidden transitions ($M_S = +1/2 \leftrightarrow -1/2$, $\Delta m_I = \pm 1$). Hyperfine components corresponding to non-central transitions are observed at the high and low field ends of the spectrum. Magnetic field strength, H, increases toward the right.

Table 3-2

CRYSTAL FIELD SPLITTING PARAMETERS

XC-1 Samples			Experimentally Shocked Samples		
Depth	ΔH (G)	D (G)[a]	Pressure (GPa)	ΔH (G)	D (G)[a]
11.1 m	11.0 ±0.5	69.0	0.15	13.5 ±1.0	74.5
11.8 m	11.5 ±0.5	71.0	0.15	14.0 ±0.5	75.9
12.2 m	12.0 ±0.5	72.0	0.25	13.5 ±1.0	74.5
~13.6 m	13.0 ±1.0	75.0	1.42	14.5 ±0.5	77.2
19.2 m	14.5 ±0.5	79.0	1.54	(11.5 ±0.5)[b]	68.8
~27.1 m	14.0 ±0.5	78.0	1.62	14.5 ±0.5	77.2
29.7 m	14.0 ±0.5	78.0	1.85	12.0 ±1.0	70.2
34.1 m	14.7 ±0.5	80.0	2.88	12.0 ±0.5	70.2
35.4 m	14.5 ±0.5	79.0	3.53	12.0 ±1.0	70.2
37.5 m	14.0 ±0.5	78.0	4.42	11.0 ±1.0	67.2
40.8 m	14.2 ±0.5	79.0	4.78	10.0 ±2.0	64.1
41.8 m	15.0 ±0.5	81.0	7.90	9.0 ±1.0	60.8
43.3 m	15.0 ±0.5	81.0	10.62	8.0 ±2.0	57.4
45.4 m	15.0 ±0.5	81.0			
Unshocked[c] single crystal calcite	15.78 ±0.1	81.0			

[a] Corrected for intrinsic line broadening

[b] Large uncertainty in datum point due to difficulty with recovery experiment

[c] The cubic crystal field splitting parameter, F, for unshocked single crystal calcite, determined from the non-central transitions, is $^{-}$7.7 ±0.3 G.

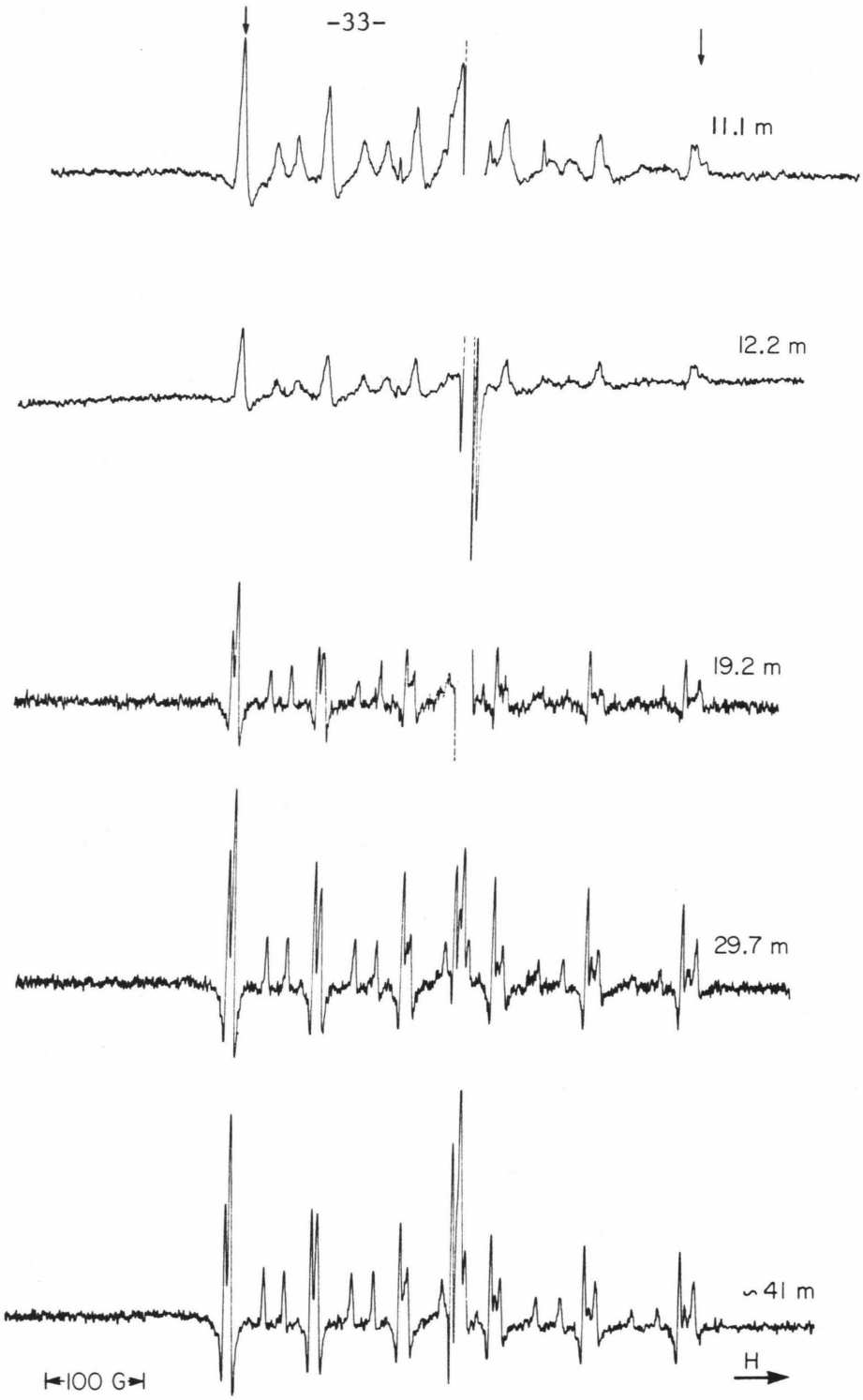

Figure 3-6. Second derivative ESR spectra of Mn^{2+} in Cactus Crater core (XC-1) samples from several depths. Note the consistant variation with depth in the splitting amplitude of the central transition hyperfine component peaks, particularly the highest and lowest field peaks (indicated by arrows). Magnetic field strength increases toward the right.

this splitting is increasingly well-defined in lower core samples. The highest field hyperfine component (right-hand arrow in figure) remains split throughout the extent of the core, but the amplitude of the splitting decreases approximately 30% from the bottom to the top, as seen in Fig. 3-7, a graph of splitting amplitude versus core depth. The equation for the power curve fit for the XC-1 data is:

$$HPS = 7.82d^{0.17} \qquad (3\text{-}2)$$

where HPS is the highest field Mn^{2+} hyperfine peak splitting, measured in gauss, and d is core depth in meters; the correlation coefficient r^2 is 0.81.

Spectra of samples taken from 3 to 60 m depths along the XRU-3, i.e. unshocked, core display no trends in their ESR signal; in particular, the upper core levels do not show any decrease in the amount of splitting. In addition, the splitting amplitude shows no correlation with the calcite to aragonite ratios of the Cactus samples.

Several spectra obtained for coral samples shock-loaded in the laboratory are presented in Figure 3-8. Note the consistent variation with shock pressure in splitting of the hyperfine components, particularly the high and low field peaks, as well as similarities between particular laboratory shocked and Cactus core samples, for example, the 2.9 GPa and XC-1 12.2 m samples. Results from the laboratory shocked coral samples are plotted in Figure 3-9. A least squares fit line to the data provides the relationship:

$$HPS = -0.60P + 13.85 \qquad (3\text{-}3)$$

where HPS is the highest field Mn^{2+} hyperfine peak splitting (gauss) and P is shock pressure (GPa); the correlation coefficient is 0.82.

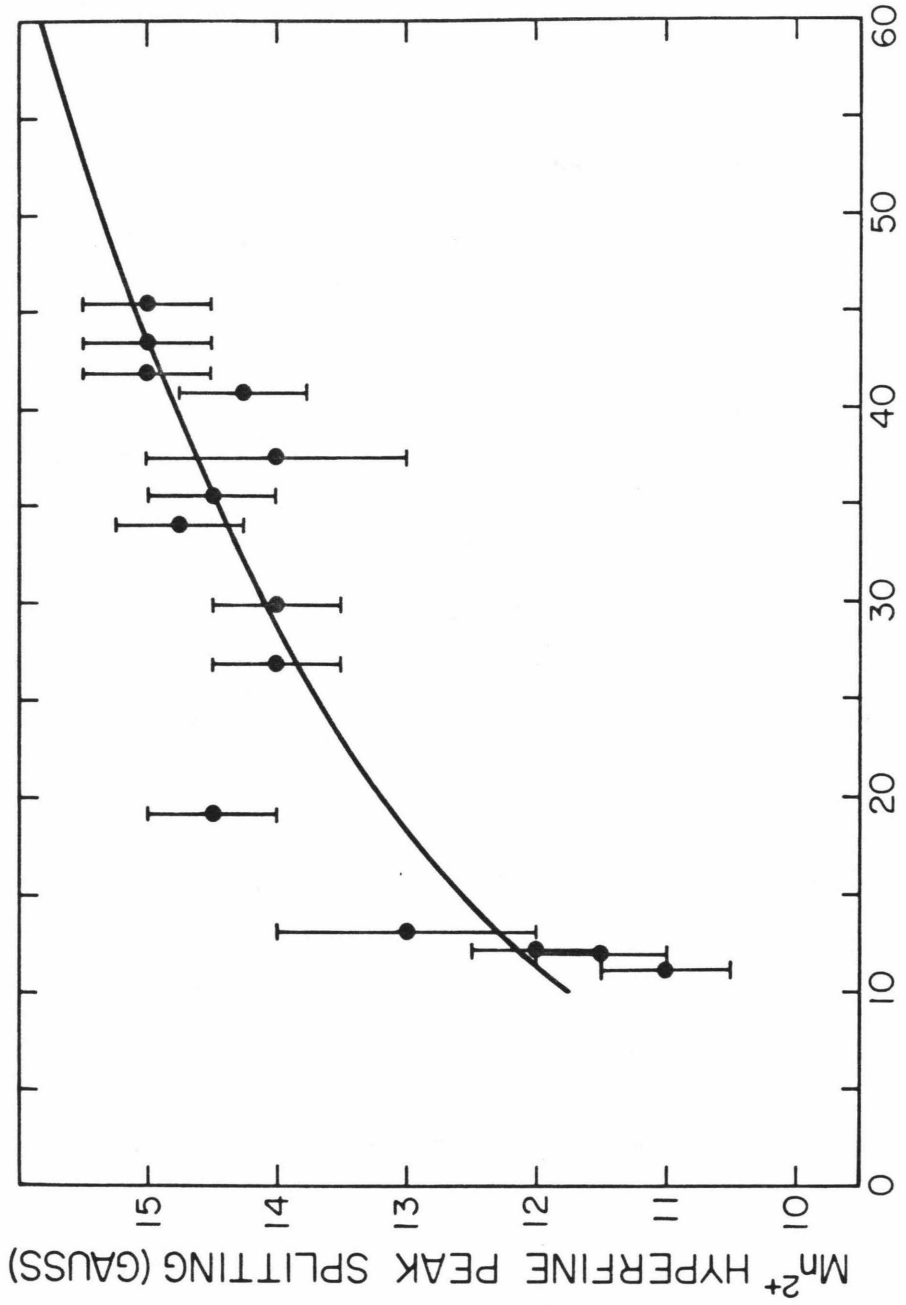

Figure 3-7. Variation of Mn^{2+} hyperfine peak splitting (HPS), as measured for the highest field component, with depth (d) in the Cactus Crater core. The equation for the power curve fit to the data is $HPS = 7.82d^{0.17}$.

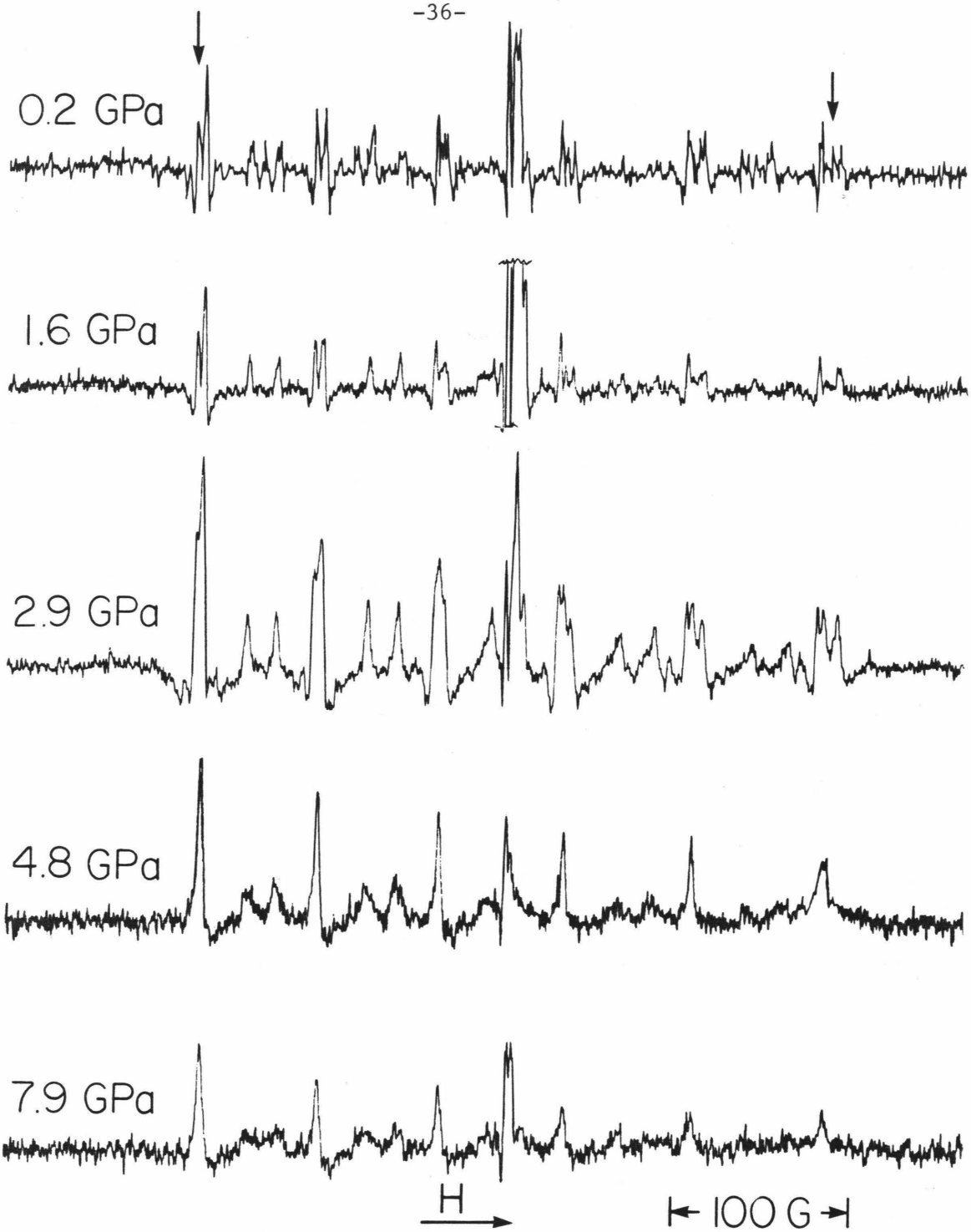

Figure 3-8. Coral core (XRU-3) samples experimentally shocked to indicated pressures (in GPa). Note the variation with pressure in the splitting of the central transition hyperfine component peaks. Magnetic field strength increases toward the right.

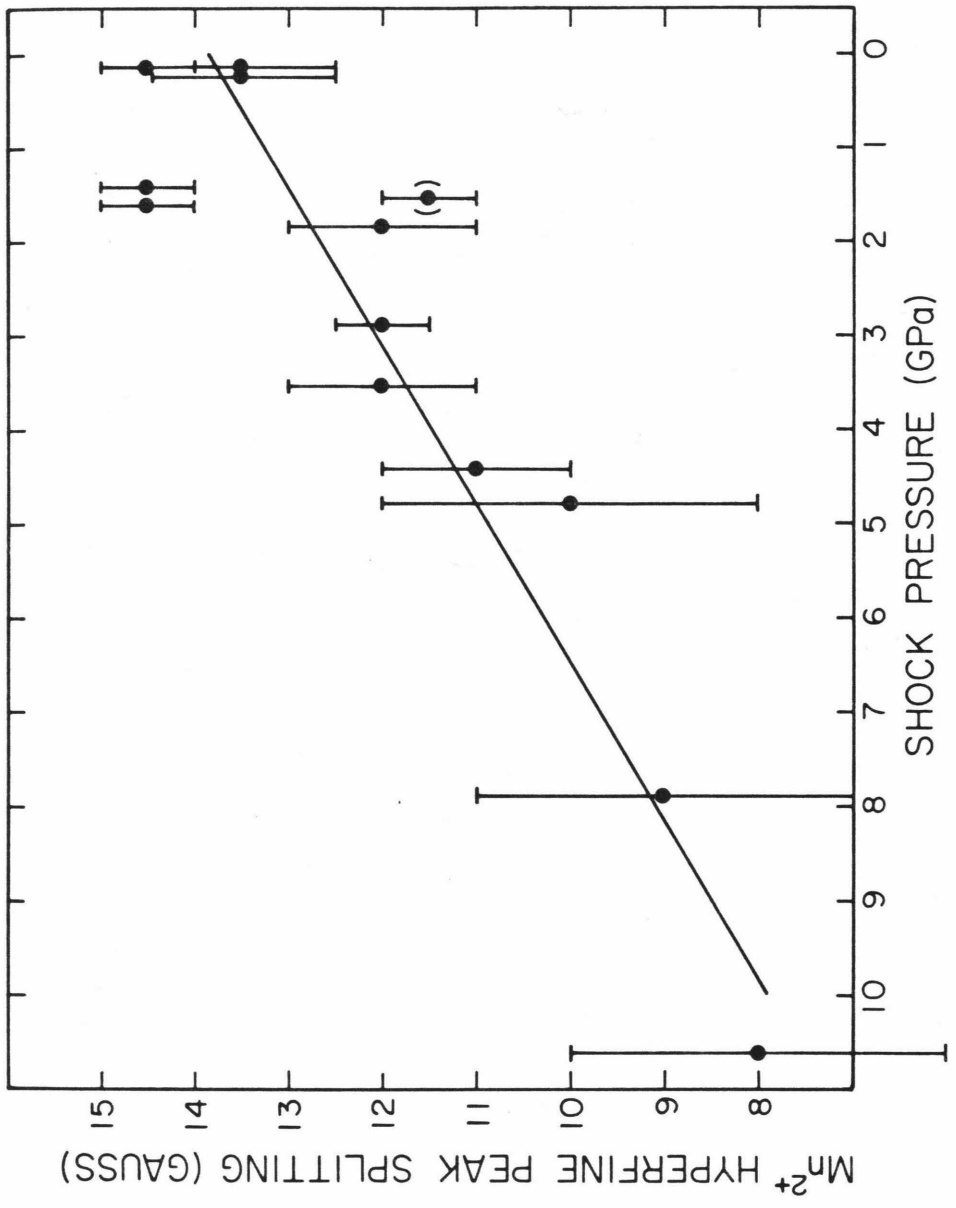

Figure 3-9. Variation of splitting in the highest field Mn^{2+} hyperfine component (HPS) with pressure (P) in experimentally shocked coral samples. Parentheses around the 1.54 GPa data point indicate uncertainty due to difficulty with the recovery experiment. The equation of the least squares fit is HPS = $^{-}$0.6P + 13.9.

Discussion of ESR Results

The splitting amplitude of the hyperfine component peaks, as calculated from the spin Hamiltonian of Mn^{2+} in calcite, is given by Eq. I-4 of Appendix I. Slight changes in the crystal field configuration at the Mn^{2+} site, a likely consequence of the shock and rarefaction process, could possibly be reflected in variations in 3 parameters of this equation: D, A and g (where g is included in the H_o term). Table 3-3 lists calculated g, A (and B) values (where A and B are the nuclear hyperfine coupling constants measured with the external magnetic field parallel and perpendicular to the c axis, respectively) for 8 of the 16 XC-1 samples and for unshocked single crystal calcite (an average of 4 samples). It is seen that the XC-1 values show no deviation from those of the unshocked calcite standard, within the error limits. D values for all of the XC-1 samples and for experimentally shocked coral were calculated using Eq. I-4 of the Appendix and splitting measurements of the highest field hyperfine component, and are presented in Table 3-2. They show a consistent decrease from the unshocked calcite value with decreasing XC-1 core depth and with increasing experimental shock pressure.

The values listed include a correction factor for intrinsic line broadening. It is qualitatively observed that the Mn^{2+} absorption peaks are broader in coral sample spectra than in single crystal calcite spectra. As noted in Table 3-2, the hyperfine splitting values for the 3 lowermost core samples are 15 G; also, samples taken along 60 m of the unshocked XRU-3 core show splitting values of 14.0 to 15.0 G. Unshocked single crystal calcite, however, shows an average splitting value of

Table 3-3

SPIN HAMILTONIAN PARAMETERS

Sample	$g_{\parallel}^{a}$	$g_{\perp}^{b}$	A (G)[c]	B (G)[d]
XC-1; 11.8 m	e	1.9996 ±0.0006	e	-94.1 ±0.5
12.2 m	e	1.9996 ±0.0006	e	-94.3 ±0.5
19.2 m	2.0039 ±0.0006	2.0004 ±0.0006	-93.7 ±0.5	-93.9 ±0.5
∿27.1 m	2.0030 ±0.0006	2.0006 ±0.0006	-93.9 ±0.5	-94.3 ±0.5
35.4 m	2.0035 ±0.0006	2.0004 ±0.0006	-94.00±0.5	-93.9 ±0.5
40.8 m	2.0035 ±0.0006	2.0008 ±0.0006	-93.7 ±0.5	-93.9 ±0.5
43.3 m	2.0033 ±0.0006	2.0006 ±0.0006	-94.0 ±0.5	-93-9 ±0.5
45.4 m	2.0035 ±0.0006	2.0004 ±0.0006	-93.7 ±0.5	-93.9 ±0.5
Unshocked single crystal calcite[f]	2.0026 ±0.0006	2.0010 ±0.0006	-93.7 ±0.1	-93.9 ±0.1

[a,b] Spectroscopic splitting factor parallel and perpendicular to c crystallographic axis, respectively

[c,d] Hyperfine coupling constant parallel and perpendicular to c crystallographic axis, respectively

[e] Calculations unavailable due to ambiguities in some peak positions

[f] Averaged values from 4 samples

15.78 G. Therefore, the amount of splitting observed may be a diminished value due to intrinsic line broadening effects. In an attempt to correct for this effect, the splitting values of coral spectra were multiplied by a factor bringing the unshocked coral ΔH into coincidence with that of the unshocked single crystal calcite value.

The effect of varying crystal field splitting parameters on the hyperfine peak splitting values has been investigated by De Wijn and Van Balderen (1967), who, using perturbation theory, calculated theoretical spectra of the central transition fine structure group at X band frequencies for various values of D and found a direct relationship between D and the splitting amplitude. Simulated spectra also demonstrate that the allowed to forbidden transition peak amplitude ratio increases with decreasing D (see Fig. 3-5). Whereas our experimental results indicate a clear and consistent relationship with shock pressure levels and hyperfine peak splitting values, the allowed to forbidden transition peak amplitude ratios conform to the trend only about 60% of the time. Since the forbidden transition peak amplitude is proportional to the cube of the width, this observed inconsistency is probably due to the variable intrinsic line broadening of the Cactus samples. On the other hand, measurements of spectra from a series of experimentally shocked single crystal calcite samples showed a slight but consistent increase in the allowed to forbidden peak ratio with increasing shock pressure. Thus, for samples where the Mn^{2+} signal suffers little interference from other paramagnetic ions or organic radicals, both hyperfine peak splitting amplitudes and allowed to forbidden transition peak ratios vary systematically, and indicate

reduction of the crystal field splitting parameter with increasing shock pressure levels.

The crystal field splitting parameter in octahedral sites, 10 Dq, is known to be inversely proportional to the fifth power of the metal-ligand distance (Burns, 1970). Since this term is directly related to the zero-field splitting parameter, D (Wait, 1963), our experimental results suggest that the shock process has the effect of, on the average, increasing the cation-anion distance in the calcite lattice. This increase would be an understandable consequence of the sizeable input of mechanical and thermal energy during the shock and rarefaction processes, and of the fact that, even at low shock pressures, calcite and calcite rocks undergo several phase transformations. Ahrens and Gregson (1964), in shock experiments on single crystal calcite, observed three changes in slope of the Hugoniot above the HEL at pressures ranging from 2.2 to 9.5 GPa. In dynamic compression experiments on limestone and marble, Grady et al. (1978) found that the calcite I → II transition, a displacive transformation, initiates between 0.6 to 1.2 GPa depending on rock type, and that the calcite II → III transition occurs above 2.4 GPa. Both groups found that the yield stress decreases with increasing porosity. Other possible phase transitions in the $CaCO_3$ - H_2O system include the calcite to aragonite transformation, occurring at 0.4 GPa at room temperature in static compression experiments (Jamieson, 1953), and the transformation of both calcite and aragonite to ikaite ($CaCO_3 \cdot 6H_2O$) at water pressures in excess of 0.6 GPa (Van Valkenburg et al., 1971). Therefore, it is likely that the carbonate materials investigated in this study, both naturally and experimentally shocked,

had reached stress levels above the Hugoniot elastic limit and perhaps above one or more phase transition boundaries; release to ambient pressures, therefore, involved more than an elastic readjustment and may have resulted in a crystal structure slightly altered from the original.

The Guinier method was used in an attempt to accurately measure the lattice parameters of calcite in the coral samples; however, due to variable amounts of Mg in the calcite lattice, the calcite reflections were too diffuse to allow any accurate cell dimension determinations. On the basis of preliminary X-ray results from single crystal calcite samples, of uniform Mg content, experimentally shocked to 6 GPa, the maximum change in lattice parameter is estimated to be on the order of 0.01 Å. Similar shock pressure induced lattice parameter increases, detected using X-ray techniques, have been reported by Chao (1968) in heavily shocked quartz from the Ries Crater in Germany, and by Schneider (1977) in experimentally shock-loaded oligoclase.

Applications to Crater Models and Conclusions

Results from experimentally shocked samples, together with those from the unshocked XRU-3 core and chemical data on Cactus core samples, substantiates the observed splitting variation along the extent of the Cactus core as a shock deformation feature and not a reflection of trends in lithology, cementation, compaction, etc. A comparison of Figures 3-7 and 3-9 suggests pressure assignments to the Cactus core of 4.5 ± 0.5 GPa at the uppermost 11.1 m level, decaying to 1.5 ± 0.5 GPa at 14 m. Beginning with the sample at approximately 20 m, hyperfine peak splittings shift to substantially higher values (see Fig. 3-7). There is a

suggestion of continuing stress level decay from 20 m to constant zero pressure levels at and below 43 m, but the power law for this portion of the curve would be of little value given the error limits of the experimental data.

Combining XC-1 data for upper core level (above $\sim$ 20 m) samples with splitting values for experimentally shocked samples gives an attenuation rate of:

$$P = (5 \times 10^6)\ d(m)^{-5.7 \pm 1.5} \qquad (3\text{-}4)$$

where P is shock pressure in GPa and d is XC-1 core depth in meters.

This decay rate is several orders of magnitude higher than typical shock pressure attenuation values of d^{-2} to d^{-3} calculated for simple, i.e. bowl-shaped, nuclear and explosion craters or predicted by impact modelling calculations (Cherry and Peterson, 1970; Ahrens and O'Keefe, 1977b). However, the decay rates obtained in the calculational processes are in terms of pre-flow coordinates, whereas Eq. 3-4 was inferred from post-flow shock metamorphic features. Therefore, before a meaningful comparison can be made, the decay rate for Cactus Crater should be corrected for any rock displacement that may have occurred during the cratering process. Unfortunately, due to the highly fractured nature of the rocks under Cactus Crater, core recovery was poor, frequent use was made of split spoon sampling, and therefore, locations of recovered samples are not always precisely known and depth to solution unconformities cannot be accurately determined. Fossil evidence (discussed in detail in the following paragraphs) suggests that the first solution unconformity, occurring at 16 m in the XC-1 core, has been depressed 2 m relative to its level outside the crater;

however, in light of the ± 1.5 m location uncertainty of Cactus samples, no firm conclusions regarding displacement can be made. A model calculation, assuming differential compaction and negligible displacement at the 20 m level, was made in order to determine the amount of shortening needed for attenuation rates of d^{-2} to d^{-3}. The results indicate maximum depression of 5 to 6 m, decreasing to 2 to 3 m at the 16 m level; the latter values are consistent with the displacement suggested by the first solution unconformity level.

Our discussion up until now has considered the ESR evidence in light of a continuous shock pressure decay model. However, an alternative interpretation, as suggested by the data in Figure 3-7, is that of a bimodal pressure distribution; samples from depths shallower than 15 m are clustered at Mn^{2+} hyperfine peak splitting values much lower (hence, at shock pressure levels much higher) than the remaining samples, which define a very gradually attenuating regime below approximately 20 m. The second interpretation is consistent with cratering models which depict an unstratified breccia lens, formed by explosive excavation and fallback, overlying bedrock that has been brecciated in situ and perhaps compressed, but otherwise has not undergone extensive disruption. Thus the discontinuity in the ESR data between approximately 15 and 20 m levels might represent the boundary between a fallback breccia unit and rock that has been disrupted in situ. A sketch of the breccia model, based primarily on well log data of gamma radiation (Ristvet et al., 1978) and consistent with this alternative interpretation of the ESR results, is presented in Fig. 3-10.

Stratigraphic evidence described in Ristvet et al., 1978, is

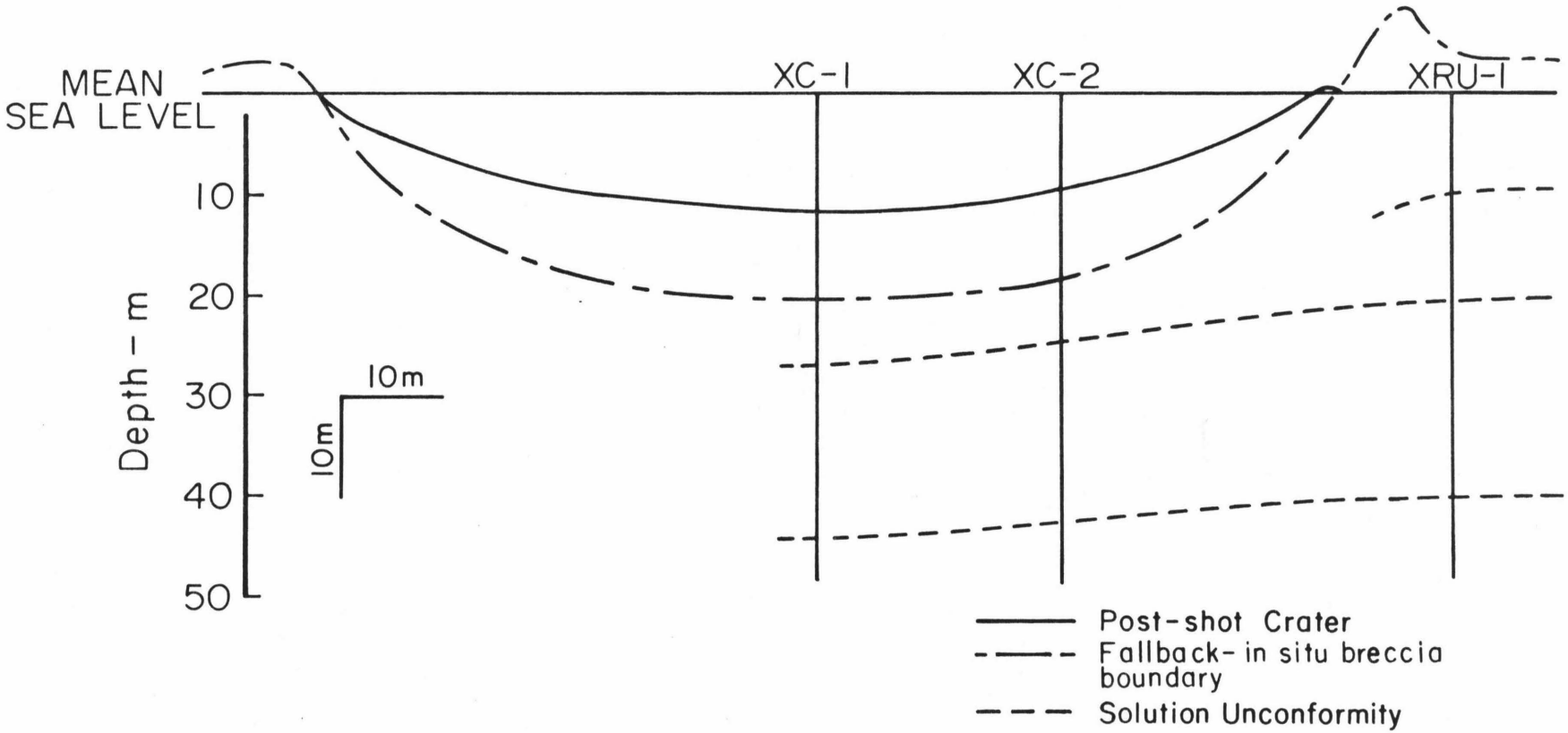

Figure 3-10. Cross section of Cactus Crater as viewed looking northeast. The position of the fallback-in situ breccia boundary is based on well log data of gamma radiation and has an uncertainty of 1.5 m. The uncertainty in the positions of the solution unconformities is ± 3 m. Adapted from Fig. 5-35 of Ristvet et al., 1978.

insufficient to delineate the true crater boundary or even to detect the presence of a breccia lens. The small amounts of rock sampled from the upper portions of the crater cannot be definitively identified as breccia fragments, due to both the lack of typical breccia characteristics, and to the fact that the split spoon sampling method by which they were retrieved alters the appearance of the bulk sample. Fossil evidence is also indeterminate. Unbleached Homotrema rubrum tests are found down to the first solution unconformity at 16 ± 1.5 m depth, depressed from the 14 m depth of this unconformity observed outside the crater. Homotrema rubrum, an encrusting foraminifera, has a bright red test while alive and gradually bleaches white at the onset of diagenesis. The occurrence of only unbleached tests above the first unconformity would indicate that, if excavation and fallback was indeed the mode of crater formation, the true crater boundary is found above 16 ± 1.5 m.

Logging of gamma activity during the drilling project at Eniwetok found a sharp decline in activity below the 20 m depth in cores XC-1 and XC-2 drilled inside Cactus Crater; the position of this drop is uncertain (± 1.5 m) due to the fact that tide height and bending of the casing were not recorded during the drilling (Ristvet et al., 1978). Therefore, given the uncertainties, the position of this break corresponds with the evidence of some discontinuity from unbleached Homotrema rubrum test occurrences, and from our ESR results. (For further discussion of gamma log evidence, see Chapter 5.)

A close look at the data presented in Figure 3-7 suggests a modification to the second interpretation. The 4 data points between 8 and 15 m show a consistent decrease toward lower shock pressure values

at lower depth. No such trend would be evident if the breccia unit were homogeneous. Therefore, stratification on the order of approximately 3 m or less is suggested for the Cactus breccia lens by the ESR data. Stratified breccia lenses have been observed in several meteorite craters, for example Brent (Dence, 1968) and Ries (Pohl et al., 1977).

In conclusion, two alternative crater models are suggested by the ESR data. In the first, the rocks beneath Cactus retain their pre-shock relative stratigraphic position; an attenuation rate of $d^{-5.7}$, calculated in terms of post-flow coordinates, may indicate a maximum downward displacement on the order of 5 to 6 m. The second model depicts a breccia lens, possibly stratified, with a breccia-bedrock interface at 20 m ± 5m. Given the limits on accuracy in the pressure correlation curve and the availability of only 1 XC-1 sample in the critical 15 to 25 m depth interval, the choice between the two models cannot be resolved on the basis of shock deformation evidence alone. New evidence is presented and the subject of Cactus Crater morphology readdressed and more thoroughly discussed in Chapter 5.

References

Ahrens, T. J. and V. G. Gregson Jr., Shock compression of crustal rocks: Data for quartz, calcite, and plagioclase rocks, J. Geophys. Res., 69, 4839-4874, 1964.

Ahrens, T. J., I. Jackson and R. Jeanloz, Shock compression and adiabatic release of a titaniferous mare basalt, Proc. Lunar Sci. Conf. 8th, 3437-3455, 1977a.

Ahrens, T. J. and J. D. O'Keefe, Equations of state and impact-induced shock-wave attenuation on the moon. In Impact and Explosion Cratering, Roddy, D. J., Pepin, R. O., and Merrill, R. B. (Editors). Pergamon Press, New York, 639-656, 1977b.

Ahrens, T. J., F. Tsay and D. H. Live, Shock-induced fine-grained recrystallization of olivine: Evidence against subsolidus reduction of Fe^{2+}, Proc. Lunar Sci. Conf. 7th, 1143-1156, 1976.

Al'tshuler, L. V. and I. I. Sharipdzhanov, Additive equations of state of silicates at high pressures, Izv. Earth Phys., 3, p. 11-28, 1971.

Burns, R. G., Mineralogical Applications of Crystal Field Theory, University Press, Cambridge, 1970.

Carter, W. J. and S. P. Marsh, Hugoniot equation of state of polymers, submitted to J. Chem. Phys., 1980.

Chao, E. C. T., Pressure and temperature histories of impact metamorphosed rocks - Based on petrographic observations. Neues Jahrb. Mineral. Abhandl., 209-246, 1968.

Cherry, J. T. and F. L. Petersen, Numerical simulation of stress wave propagation from underground nuclear explosions, Peaceful Nuclear

Explosions, Internat. Atomic Energy Agency, Vienna, 241-325, 1970.

Couch, R. F., J. Fetzer, E. Goter, B. Ristvet, E. Tremba, D. Walter, and V. Werdland, Drilling Operations in Eniwetok Atoll During Project EXPOE, Air Force Weapons Laboratory, Final Report, 1975.

Dence, M. R., Shock zoning at Canadian craters: Petrography and structural implications. In Shock Metamorphism of Natural Materials, French, B. M., and Short, N. M. (Editors), Mono Book Corp., Baltimore, 1968.

De Wijn, H. W. and R. F. Van Balderen, Electron spin resonance of manganese in borate glasses, J. Chem. Phys., 46, 1381-1387, 1967.

Dunham, R. J., Classification of carbonate rocks according to depositional texture. In Classification of Carbonate Rocks, Ham, W. E. (Editor), American Association of Petroleum Geologists Memoir I, 108-121, 1962.

Gager, W. B., M. J. Klein and W. H. Jones, The generation of vacancies in MgO single crystals by explosive shock. Applied Physics Letters, 5, 131-132, 1964.

Grady, D. E., R. E. Hollenbach and K. W. Schider, Compression wave studies on calcite rock, J. Geophys. Res., 83, 2839-2849, 1978.

Jamieson, J. C., Phase equilibrium in the system calcite-aragonite, J. Chem. Phys., 21, 1385-1390, 1953.

Kalashnikov, N. G., M. N. Pavlovskiy, G. V. Simakov and R. F. Trunin, Dynamic compressibility of calcite group minerals, Izv. Earth Phys., 2, 23-29, 1973.

Linde, R. K. and P. S. DeCarli, Polymorphic behavior of Titania under dynamic loading, J. of Chem. Phys., 50, p. 319-325, 1969.

Low, W. and S. Zeira, ESR spectra of Mn^{++} in heat-treated aragonite, Am. Mineralogist, 57, 1115-1124, 1972.

McQueen, R. G., S. P. Marsh, T. W. Taylor, J. N. Fritz and W. J. Carter, The equation of state of solids from shock wave studies. In High Velocity Impact Phenomena (R. Kinslow, ed.) Academic Press, New York, 294-419, 1970.

Pohl, J., D. Stöffler, H. Gall and K. Ernstson, The Ries impact crater. In Impact and Explosion Cratering, Roddy, D. J., Pepin, R. O., and Merrill, R. B. (Editors), Pergamon Press, New York, 343-404, 1977.

Ristvet, B. L., E. L. Tremba, R. F. Couch, J. A. Fetzer, E. R. Goter, D. R. Walter, and V. P. Wendland, Geologic and geophysical investigations of the Eniwetok nuclear craters. Air Force Weapons Laboratory, Final Report, 1978.

Schneider, H., Mechanical deformation and structural state of experimentally shock-loaded oligoclases, N. Jb. Miner. Mh., 1977, 255-269, 1977.

Stöffler, D., Deformation and transformation of rock-forming minerals by natural and experimental shock processes, Fortschr. Miner., 49, 50-113, 1972.

Van Valkenburg, A., H. K. Mao, and P. M. Bell, Ikaite ($CaCO_3 \cdot 6\ H_2O$), a phase more stable than calcite and aragonite ($CaCO_3$) at high water pressure. Carnegie Inst. Wash. Yr. Book, 70, 237-238, 1971.

Wait, D. F., Hydrostatic pressure dependence of the paramagnetic resonance of an S-state ion in a noncubic lattice: Mn^{2+} in calcite, Phys. Rev. 132, 601-607, 1963.

Wyllie, P. J. and A. L. Boettcher, Liquidus phase relationships in the system $CaO-CO_2-H_2O$ to 40 kilobars pressure with petrological applications, Am. J. of Science, 267, p. 489-508, 1969.

Chapter 4

SHOCK DEFORMATION OF ARAGONITE FROM CACTUS CRATER: X-RAY DIFFRACTION STUDIES

Introduction

X-ray diffraction techniques are useful tools in investigations of shock metamorphism in minerals and rocks. Use of both single crystal and powder methods allow identification of such shock-induced phenomena as high pressure phase formation (e.g., coesite from quartz; Chao et al., 1960), disproportionation (e.g. andalusite to Al_2O_3 and SiO_2; Schneider and Hornemann, 1977), diaplectic glass formation from various silicate minerals (Hörz and Quaide, 1973), twinning (e.g., lunar ilmenite; Minkin and Chao, 1971), cell dimension expansion (e.g. feldspar; Schneider, 1977) and structural symmetry changes (e.g., TiO_2; McQueen et al., 1967).

Single crystal X-ray techniques, such as Laue, Weissenberg and single crystal Debye-Scherrer, offer the advantage of potentially lending insight into the mechanisms of deformation. Minkin and Chao (1971), for example, determine shock-produced twinning planes and directionally dependent crystallographic strain (qualitatively) using single crystal techniques. In addition, these methods allow correlation of the direction of shock-wave propogation to that of the resulting crystal deformation (Levien and Ahrens, 1980). Prior to the present study, shock deformation work on carbonate minerals was limited to a few

reconnaissance optical microscopy and single crystal X-ray (Laue) investigations (Offield and Pohn, 1979; Dachille et al., 1968); pronounced asterism, indicative of crystal lattice distortion, was evident in shocked calcite and dolomite.

Powder X-ray diffraction techniques, such as the Guinier method, can also provide information on the nature of shock-produced crystal deformation, specifically the amount and direction of lattice expansion (Schneider, 1977). In addition, powder methods offer the distinct advantages of convenience and a statistically valid basis for estimating shock pressures in a bulk sample.

This study attempts to use powder X-ray diffraction data, specifically, peak broadening measurements, to investigate shock-induced deformation in aragonite, the high pressure polymorph of calcite. X-ray peak broadening is a familiar technique in the metallurgical field, commonly used in studies of cold-work distortion of metals (see e.g., Warren and Averbach, 1950). It has also been applied to explosively shocked Al_2O_3 and MgO powders (Heckel and Youngblood, 1968; Sawaoka et al., 1979) and statically naturally and experimentally deformed calcite (Newton et al., 1969; Gross, 1965). Recently, the technique has been used to investigate geological materials shocked by meteorite impact, explosive and laboratory shock experiments (Hanss et al., 1978). Samples used in this study include Cactus Crater core material (see introduction and Chapter 3) and laboratory shocked coral and single crystal aragonite. Only aragonite from the Cactus core and laboratory shocked coral material is investigated here, because the variable chemistry of the calcite component also causes peak broadening, super-

imposed on that which is deformation induced; as will be shown, the aragonite component is compositionally uniform. Thus, references to coral material specifically address the aragonite component.

X-Ray Peak Broadening - Background

Causes of X-ray diffraction peak broadening and different methods of data analysis are briefly introduced in this section. The variance technique, to be used in the aragonite shock deformation study, is presented in a more detailed fashion. For a thorough discussion of X-ray peak broadening, the reader is referred to Chapter 9 of Klug and Alexander (1974).

X-ray powder diffraction peaks of a strain-free sample with sufficiently large crystallites (the effective coherently diffracting domains) should, theoretically, be extremely sharp. In practice, however, diffraction peaks are broadened by a variety of instrumental and sample-related factors. Instrumental parameters affecting peak width include incident X-ray beam divergence, beam non-monochromaticity and detector geometry. The following physical factors, related to the nature of the sample, have been proposed as causes of X-ray peak broadening:

i) varying particle size, i.e. actual dimension of the sample powder particles,

ii) very small crystallite, or effective coherently diffracting domain, size; note that this can be smaller than the particle size,

iii) crystallites with varying lattice spacings, and

iv) straining of the crystal structure.

The effects of the first cause, i.e. that of particle size, can be eliminated by sifting the sample in order to obtain a uniform particle size. No support for the third mechanism as an active participant in peak broadening is found in experiments on deformed metals. The various X-ray peak broadening analyses described in the metallurgical literature, therefore, do not include treatment of the lattice spacing factor. However, as mentioned in the introduction, cell dimension expansion is a documented shock effect, and the exclusion of lattice spacing variations from treatment of shock deformation data requires further examination. Shock-induced expansion of aragonite cell dimensions would result in X-ray diffraction peaks shifted, or at least skewed, toward lower 2θ diffraction angles. As part of the peak broadening analysis, the centroids, or centers of gravity, of the most intense aragonite reflections were calculated and are listed in Table 4-1. Note the constancy of the centroid values. Thus, shock-induced lattice expansion, if it exists, is too small to allow detection by X-ray powder diffraction methods, and the contribution of cell dimension variations to X-ray peak broadening can be neglected. The constant aragonite peak centroid values also indicate compositional uniformity.

Thus, two factors contributing to X-ray peak broadening remain: small crystallite size, commonly referred to as mosaicism, and strain; these phenomena, indicative of material deformation, are schematically drawn in Fig. 4-1. Various methods of X-ray data treatment for the simultaneous determination of crystallite size and strain have been proposed. The simplest techniques assume simple additivity of peak breadths resulting from size and strain effects (Hall, 1949). Another

Table 4-1

CENTROID AND VARIANCE CALCULATIONS

Sample	hkl	Centroid (radians)	Variance = W (radians x 10^{-6})	$\psi W^{(a)}$ (radians/Å)	$\psi 4_{\circ} \tan^2\theta^{(a)}$ ($1/Å \times 10^{-4}$)
XC-1/11.1m	111	0.456	3.987	8.011	1.483
	021	0.474	3.720	8.736	1.380
	012	0.578	3.974	12.942	1.455
	221	0.798	4.183	25.147	1.471
11.8m	111	0.456	2.866	8.011	1.066
	021	0.474	3.163	8.736	1.174
	221	0.799	4.252	25.147	1.495
12.2m	111	0.456	2.580	8.011	0.960
	021	0.474	2.819	8.736	1.046
	221	0.798	3.699	25.147	1.301
15.4	111	0.456	3.001	8.011	1.116
±0.8m	021	0.474	2.891	8.736	1.073
	221	0.798	3.588	25.147	1.262
19.2m	111	0.456	3.242	8.011	1.206
	021	0.474	2.754	8.736	1.022
	221	0.798	3.795	25.147	1.335
XC-2/10.1	111	0.456	3.312	8.011	1.232
±0.2m	021	0.474	4.382	8.736	1.626
	221	0.799	4.134	25.147	1.454
10.6	111	0.456	3.150	8.011	1.172
±0.2m	021	0.474	3.802	8.736	1.411
	012	0.577	3.569	12.942	1.306
	221	0.799	3.493	25.147	1.229
12.1	111	0.455	2.812	8.011	1.046
±0.2m	021	0.474	2.674	8.736	0.992
	012	0.578	2.840	12.942	1.039
	221	0.798	3.691	25.147	1.298

Sample	hkl	Centroid (radians)	Variance = W (radians x 10^{-6})	$\psi W^{(a)}$ (radians/A°)	$\psi 4_o \tan^2\theta^{(a)}$ ($1/Ax10^{-4}$)
15.2	111	0.456	2.529	8.011	0.941
±0.9m	021	0.474	3.191	8.736	1.184
	221	0.798	3.445	25.147	1.212
29.7	111	0.456	2.783	8.011	1.035
±0.5m	021	0.475	1.857	8.736	0.689
	221	0.798	3.046	25.147	1.071
XRU-3/3m	111	0.454	3.643	8.011	1.355
	021	0.474	2.420	8.736	0.898
	012	0.578	2.211	12.942	0.809
	221	0.798	3.736	25.147	1.314
10.7m	111	0.456	2.922	8.011	1.087
	021	0.475	2.616	8.736	0.971
	012	0.578	2.621	12.942	0.959
	221	0.798	3.384	25.147	1.190
21m	111	0.455	3.187	8.011	1.185
	012	0.577	2.301	12.942	0.842
	221	0.799	3.651	25.147	1.284
Laboratory Shocked Coral/					
0.2GPa	111	0.456	3.033	8.011	1.128
	012	0.577	2.600	12.942	0.952
	221	0.798	3.747	25.147	1.318
4.4GPa	111	0.456	4.353	8.011	1.619
	012	0.577	4.908	12.942	1.796
	221	0.798	6.582	25.147	2.315
7.1GPa	111	0.456	5.671	8.011	2.109
	021	0.474	6.826	8.736	2.533
	012	0.577	7.942	12.942	2.907
	221	0.796	13.652	25.147	4.802
7.9GPa	111	0.456	5.078	8.011	1.889
	021	0.474	6.215	8.736	2.306
	221	0.795	11.985	25.147	4.215
10.6GPa	111	0.456	7.005	8.011	2.606
	021	0.474	8.778	8.736	3.257
	221	0.798	11.954	25.147	4.204

Sample	hkl	Centroid (radians)	Variance = W (radians x 10^{-6})	$\psi W^{(a)}$ (radians/Å)	$\psi 4_{\circ}\tan^2\theta^{(a)}$ ($1/Ax10^{-4}$)
Unshocked Single Crystal Aragonite	111	0.455	3.078	8.011	1.145
	021	0.474	2.251	8.736	0.836
	012	0.578	2.830	12.942	1.036
	112	0.660	3.147	17.058	1.136
	221	0.798	3.193	25.147	1.132
Shocked Single Crystal Aragonite/ 8.1 GPa	111	0.454	3.548	8.011	1.320
	021	0.474	3.216	8.736	1.194
	012	0.578	3.737	12.942	1.368
	221	0.798	4.573	25.147	1.608

(a) ψ is defined as $\frac{\cos\theta}{\Delta(2\theta)\lambda}$, where θ refers to the angle of reflection, $\Delta(2\theta)$ is the increment used in variance calculations (see text) and λ is the X-ray wave length (1.5405 Å for Cu Kα radiation).

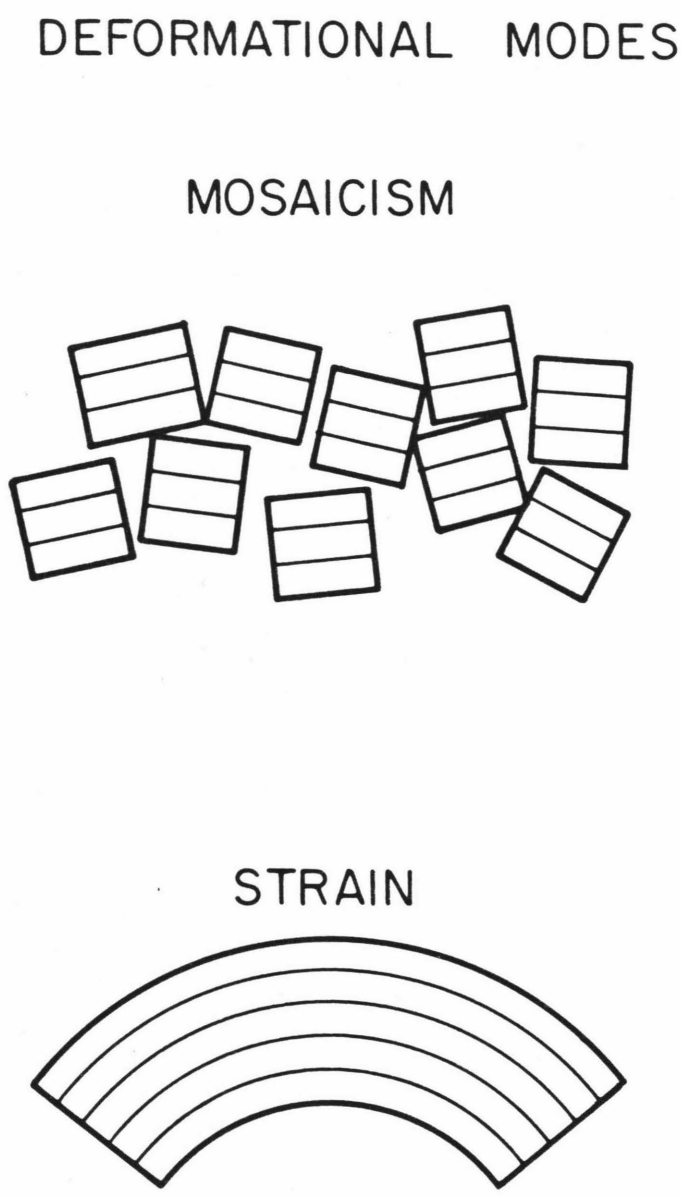

Figure 4-1. Schematic depiction of the two deformational modes contributing to X-ray peak broadening: mosaicism (or small crystallite size) and strain.

method, that of integral breadths (Klug and Alexander, 1974), requires assumptions as to the peak shape resulting from each effect; for example, broadening due to strain is often approximated by a Gaussian function, and that due to size by a Cauchy function. The Warren-Averbach (1950) method, using a Fourier series representation of the peak profile, allows resolution of size and strain effects from a single reflection; in addition, if several orders of reflection are available, the root mean square strain can be determined. This method is attractive in that it requires no assumptions regarding peak breadth additivity or profile function. However, it is a tedious analysis not readily applicable to the mineral aragonite, which shows no strong higher order reflections.

The variance method (Klug and Alexander, 1974), chosen for this study, requires no higher order reflections or assumptions regarding the peak profile, and, with the aid of a computer, provides accurate and efficient crystallite size and strain determinations from X-ray peak broadening data. Defined as the mean square breadth of a diffraction peak, the variance is determined as follows:

i) a diffraction peak profile is appropriately truncated and its angular extent divided into closely spaced increments,

ii) at the center of each increment, the angle, $2\theta_i$, the intensity, $I(2\theta)_i$, and the angular extent of the increment $\Delta(2\theta)_i$ are noted,

iii) the centroid, $\langle 2\theta \rangle$, or center of gravity of the diffraction peak, is calculated as follows:

$$\langle 2\theta \rangle = \frac{\Sigma 2\theta_i \cdot I(2\theta)_i \cdot \Delta(2\theta)_i}{\Sigma I(2\theta)_i \cdot \Delta(2\theta)_i} \qquad (4\text{-}1)$$

iv) the variance, W, is then calculated according to:

$$W = \frac{\Sigma(2\theta_i - \langle 2\theta \rangle)^2 \cdot I(2\theta)_i \cdot \Delta(2\theta)_i}{\Sigma I(2\theta)_i \cdot \Delta(2\theta)_i} \qquad (4\text{-}2)$$

Figure 4-2 schematically illustrates part of this calculational procedure. As detailed in Klug and Alexander (1974), the contribution of the crystallite size to peak variance follows the relationship:

$$W^S = \frac{K\lambda\Delta(2\theta)}{2\pi^2 p\cos\theta} \qquad (4\text{-}3)$$

where K is the Scherrer constant, related to crystallite shape and approximately equal to unity, λ is the X-ray wavelength ($\mathring{A}$), and p is the crystallite size ($\mathring{A}$). (A term including a crystallite shape related taper parameter should, strictly speaking, be included in Eq. 4-3; however, its relative insensitivity makes it useless in practical applications and it is commonly neglected.) The contribution to the variance from distortions, or local strains, $e = \Delta\ell/\ell$, is as follows:

$$W^D = 4 \tan^2\theta \langle e^2 \rangle \qquad (4\text{-}4)$$

where $\langle e^2 \rangle$ is the mean square strain. Since variance has the convenient property of additivity, the net variance of a diffraction profile is merely the sum of the size and distortion contributions:

$$W = W^S + W^D = \frac{K\lambda\Delta(2\theta)}{2\pi^2 p\cos\theta} + 4 \tan^2\theta \langle e^2 \rangle \qquad (4\text{-}5)$$

or, rearranging terms (and assuming K = 1):

$$\frac{W\cos\theta}{\Delta(2\theta)\lambda} = \frac{1}{2\pi^2 p} + \frac{4 \sin\theta \tan\theta}{\lambda\,\Delta(2\theta)} \langle e^2 \rangle \qquad (4\text{-}6)$$

Therefore, calculating peak variances for reflections at several 2θ values and plotting $\left[\frac{W\cos\theta}{\Delta(2\theta)\lambda}\right]$ versus $\left[\frac{4\sin\theta\tan\theta}{\lambda\,\Delta(2\theta)}\right]$, yields sample particle size from the y-intercept and mean square strain from the slope

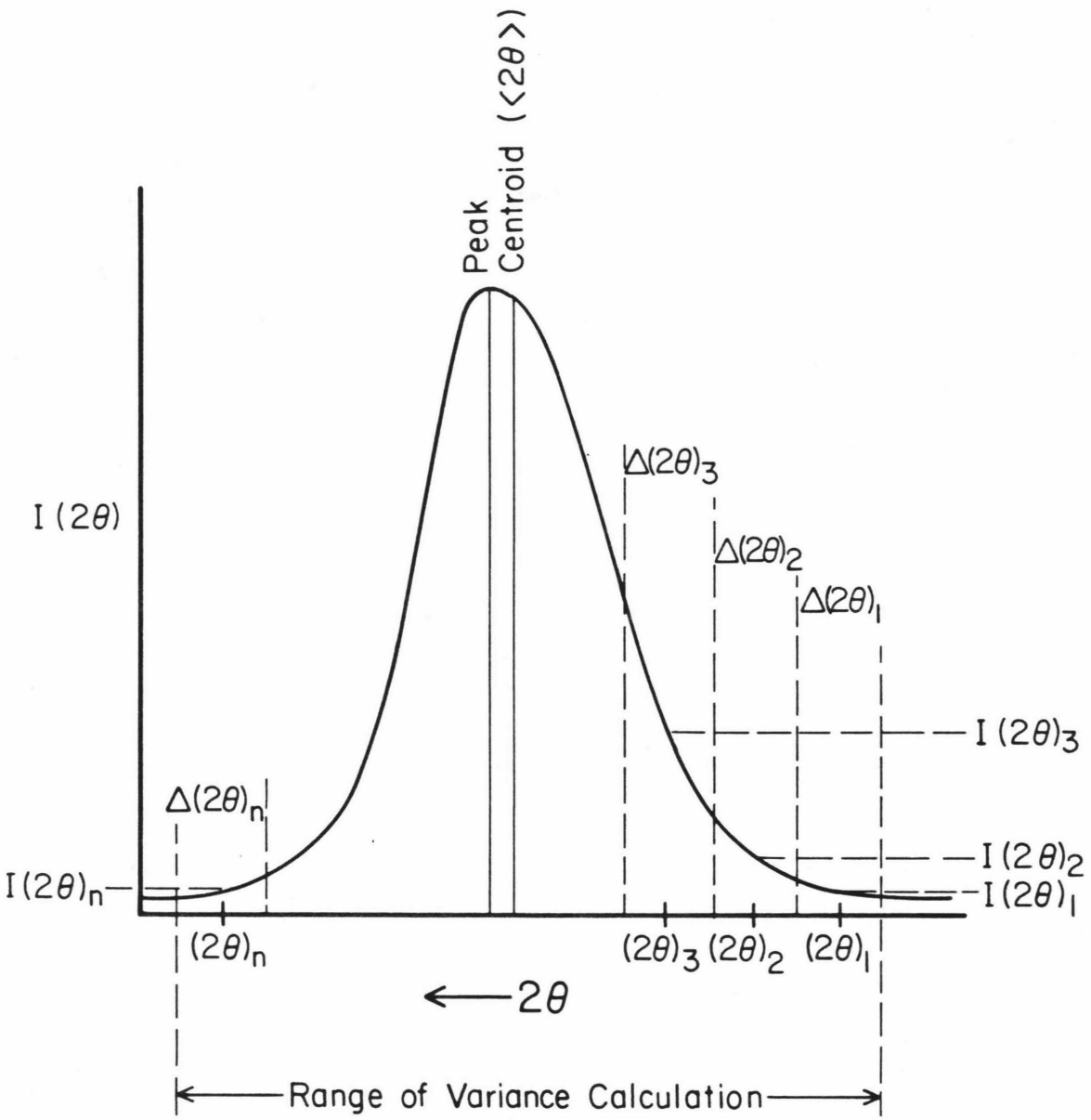

Figure 4-2. Schematic of a powder X-ray diffraction peak illustrating the procedure for calculating peak variance. I(2θ) refers to peak intensity at the angle, 2θ.

of the line.

Peak Broadening Analysis

Coralline and single crystal aragonite samples were prepared for powder X-ray diffraction analysis as described in Appendix II; details of the diffraction procedure are presented in the same appendix.

Depending on the amount of sample, or specifically, on the concentration of aragonite in the sample, 3 to 5 reflections were sufficiently intense to allow a peak variance calculation. In decreasing order of intensity, these reflections, and their corresponding d spacings are: (111) and 3.396Å, (221) and 1.977Å, (021) and 3.273Å, (012) and 2.700Å, and (112) and 2.373Å. The angular extent of the variance calculation was typically 1° 2θ, although the three most highly laboratory shocked samples had very broad reflections requiring a 1.5° 2θ calculation interval. The X-ray peaks were then digitally recorded, with 25 to 45 data points typically obtained for each peak. (One datum is an x, y point corresponding to angle, peak intensity.) A computer code then calculated the centroid and variance for each peak. The Cu Kα X-ray wave length, λ = 1.5405 Å was used, and K was assumed to be unity.

Results

Power X-ray diffraction spectra were obtained for samples from Cactus Crater cores XC-1 and XC-2, Runit core XRU-3, laboratory shocked coral, and unshocked and shocked single crystal aragonite; the recorded aragonite peaks were analyzed according to the procedure described in the previous two sections. Calculated centroids and variances are listed in Table 4-1. In addition, ordinate and abcissa parameters, as

defined in Eq. 4-6, are presented as ψW and $\psi 4 \tan^2\theta$, respectively, where $\psi = \frac{\cos\theta}{\Delta(2\theta)\lambda}$. ($\psi$ is defined merely for convenience and has no physical significance.)

Figures 4-3 through 4-7 plot ψW versus $\psi 4 \tan^2\theta$ for XC-1 and XC-2, XRU-3, laboratory shocked coral, and single crystal aragonite samples respectively. Repeated X-ray diffraction runs and data re-analysis essentially duplicated original results; intrinsic sample variability (see Fig. 4-5, the control sample plot), therefore, and not analytical reproducibility, limit the accuracy of the method. A linear least squares fit to the data from each sample yields y-intercept (indicated by large symbols on y-axes in Figs. 4-3 through 4-7) and slope values; those are listed in Table 4-2. Crystallite sizes are calculated from the y-intercepts according to Eq. 4-6, i.e.,

$$p \text{ (crystallite size, } \mathring{A}) = \left[\text{y intercept} \cdot 2\pi^2\right]^{-1} \qquad (4\text{-}7)$$

The slope of the linear least squares fit is equal to the mean square strain, $\langle e^2 \rangle$ (see Eq. 4-6). The crystallite sizes and root mean square (r.m.s.) strain, $\langle e^2 \rangle^{1/2}$, values are also presented in Table 4-2. $\langle e^2 \rangle^{1/2}$ is the measure of strain commonly used in the peak broadening literature and has been calculated here for comparison purposes. The crystallite size and r.m.s. strain values reported here are within an order of magnitude of those calculated for explosively shocked Al_2O_3 and MgO (Sawaoka et al., 1979) and plastically deformed calcite (Paterson, 1959), affirming the quantitative validity of the variance method as applied in this study. The linear least squares fit for each investigated sample is drawn through the corresponding points. In addition, the linear fit representing the average of the XRU-3 samples

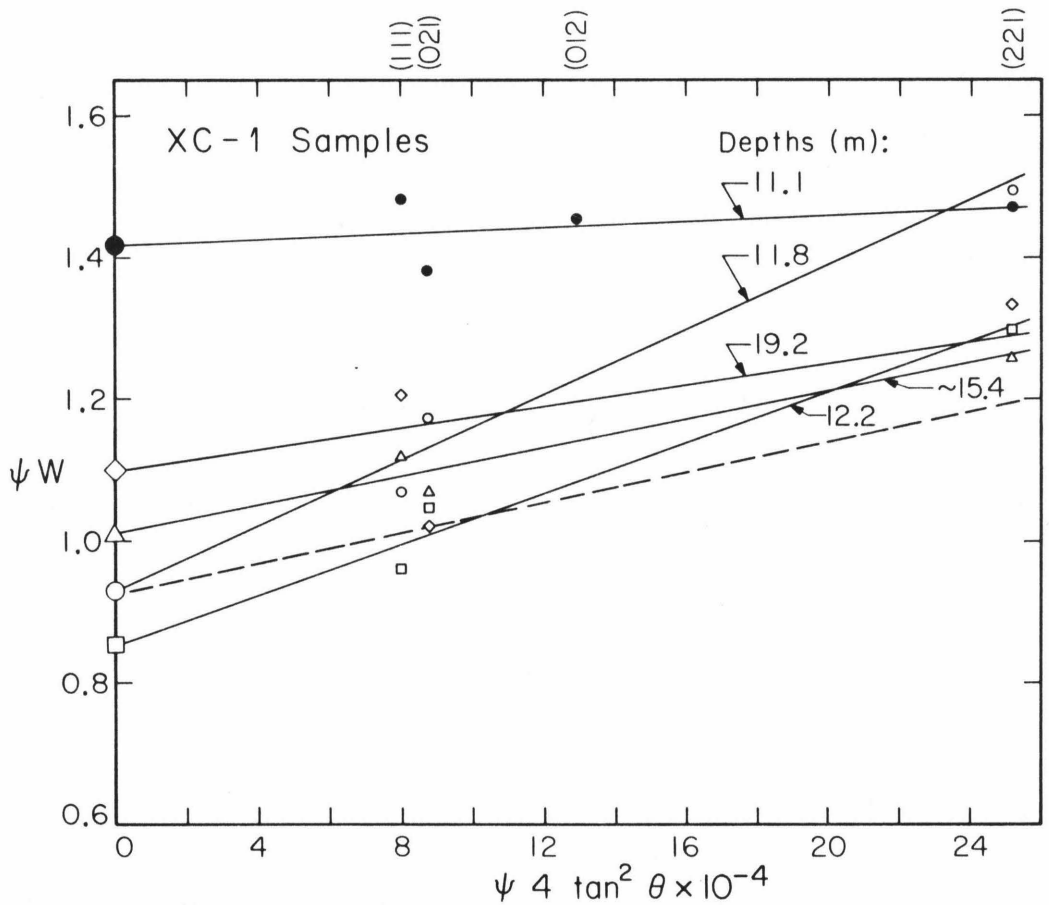

Figure 4-3. Plot of ψW for XC-1 core samples, where W is the variance, versus a function of diffracting angle, $\psi 4 \tan^2\theta$ (x 10^{-4}), for aragonite reflections; ψ is defined as: $\frac{\cos\theta}{\Delta(2\theta)\lambda}$, and diffracting planes are indicated at top of figure. Lines are linear least squares fits and are labelled with sample depths. Crystallite sizes are inversely proportional to y-axis intercepts, denoted by large symbols (see text). Similar symbols represent a single sample. Dashed line represents average of XRU-3 sample data (see Fig. 4-5).

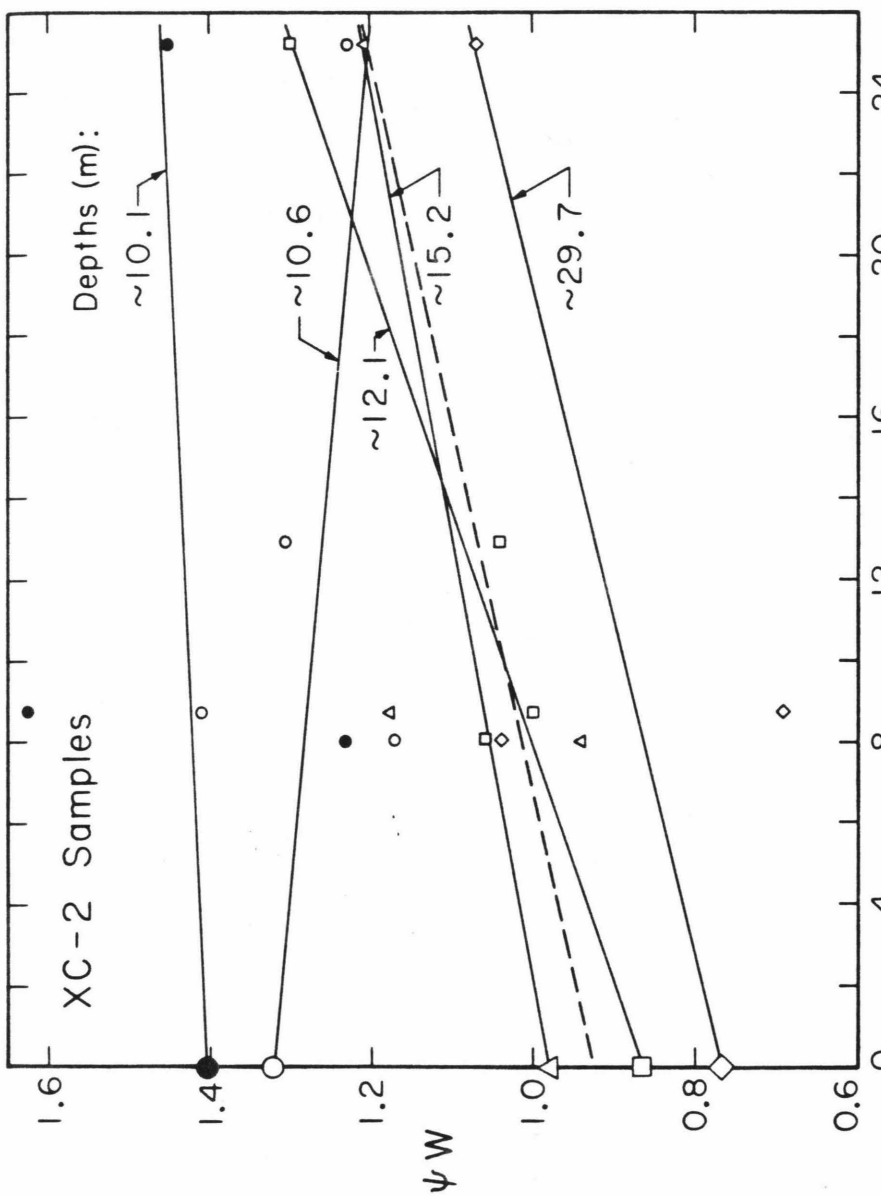

Figure 4-4. Plot of $\psi 4 \tan^2\theta$ (x 10^{-4}) for XC-2 samples. The same conventions described for Fig. 4-3 are used here.

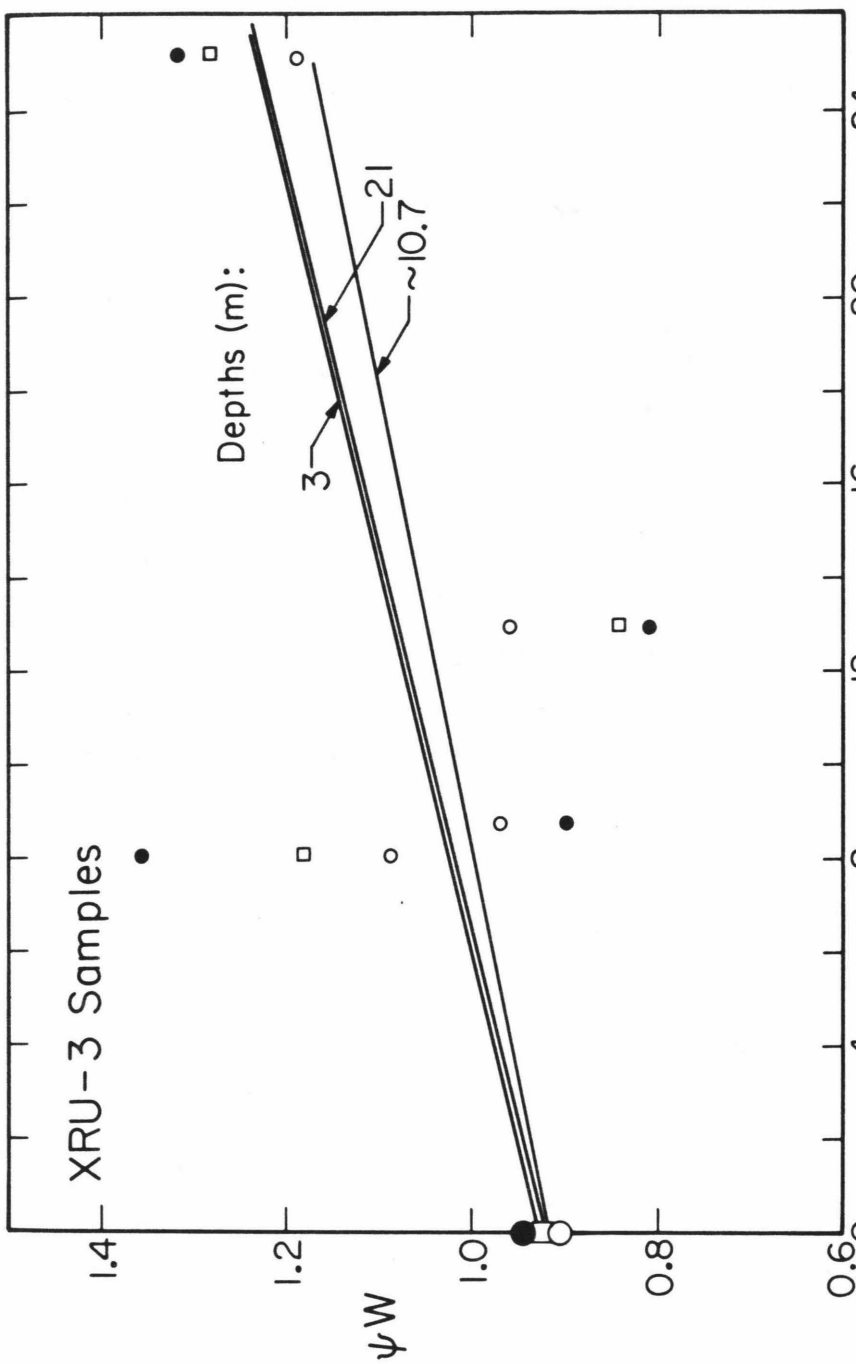

Figure 4-5. Plot of ψW versus $\psi 4 \tan^2\theta$ (x 10^{-4}) for XRU-3 (the control core) samples, using the same conventions as in Fig. 4-3.

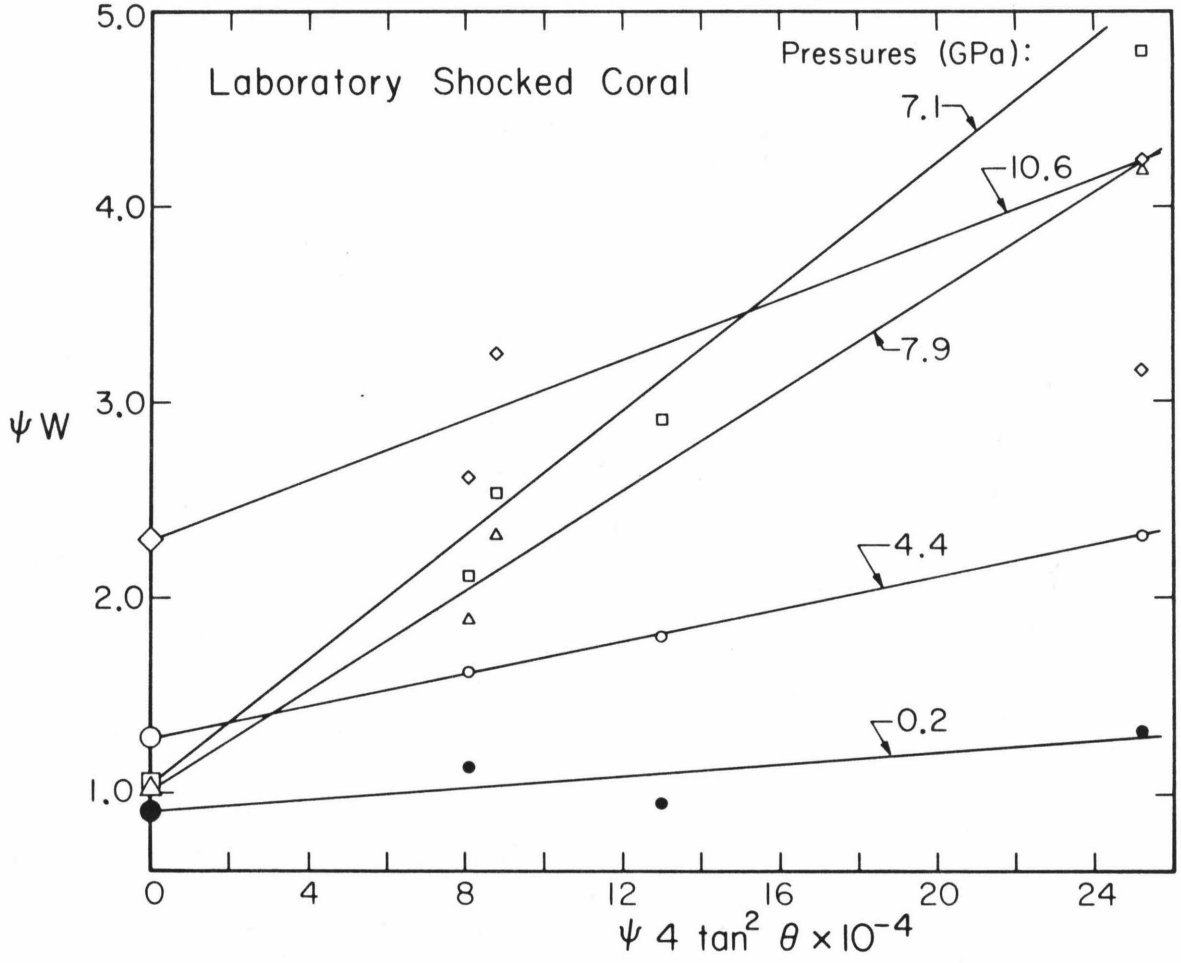

Figure 4-6. Plot of ψW versus $\psi 4 \tan^2\theta$ (x 10^{-4}) for coral samples shocked in the laboratory to pressures, in GPa, indicated in the right-hand side. Symbol conventions are those described for Fig. 4-3.

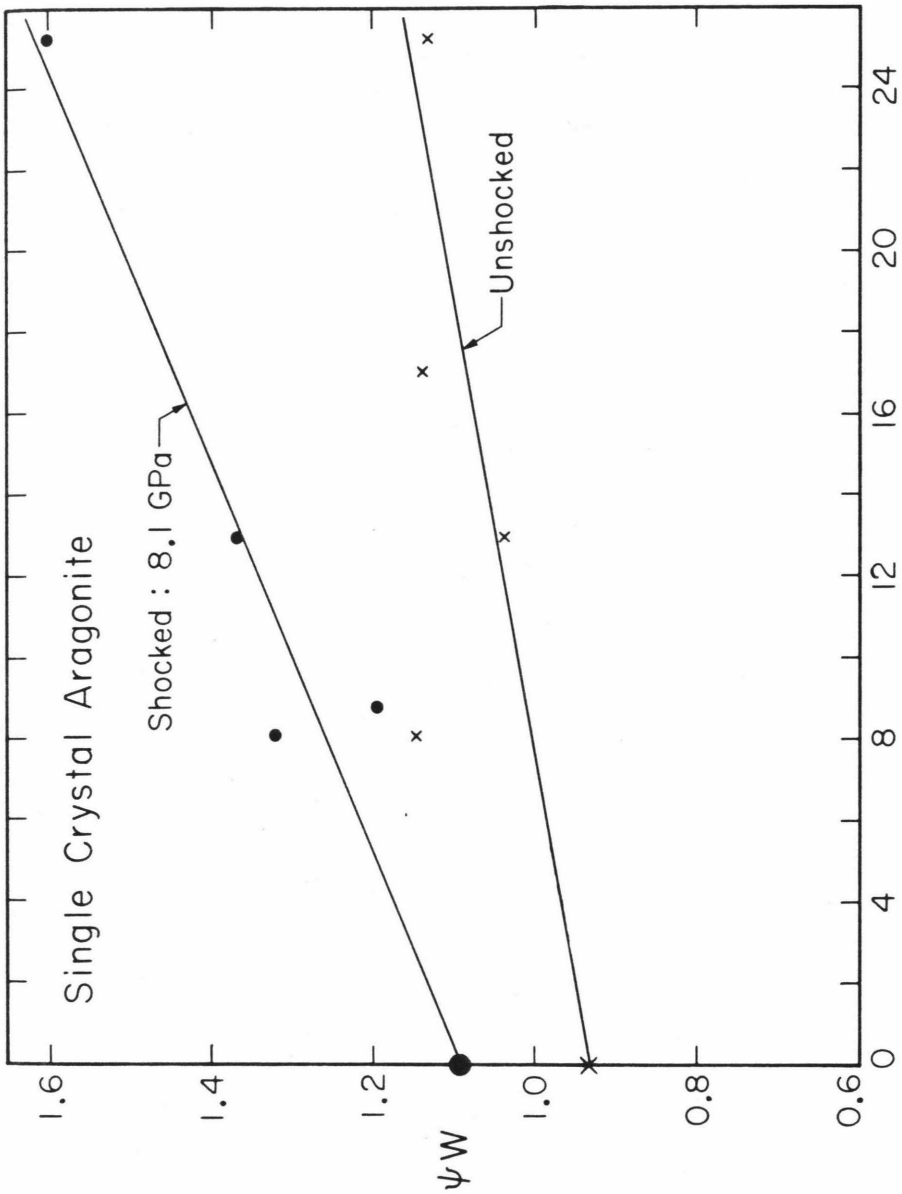

Figure 4-7. Plot of ψW versus $\psi 4 \tan^2\theta$ (x 10^{-4}) for unshocked and laboratory shocked (to 8.1 GPa) single crystal aragonite, using the same symbol conventions as in Fig. 4-3.

Table 4-2

CRYSTALLITE SIZES AND STRAINS

Sample	y-intercept ($1/Å \times 10^{-4}$)	slope ($\times 10^{-6}$)	r (correlation coefficient)	Crystallite Size (Å)	R.M.S. $\langle e^2 \rangle^{1/2} \times 10^{-3}$
XC-1/11.1m	1.418	0.210	0.36	357	0.458
11.8m	0.930	2.253	0.98	540	1.501
12.2m	0.852	1.791	0.98	595	1.338
15.4±0.8m	1.012	0.989	0.97	501	0.994
19.2m	1.009	1.280	0.79	502	1.131
XC-2/10.1±0.2m	1.406	0.225	0.11	360	0.474
10.6±0.2m	1.326	-0.339	0.26	382	--
12.1±0.2m	0.864	1.673	0.96	586	1.294
15.2±0.9m	0.981	0.937	0.61	516	0.968
29.7±0.5m	0.767	1.178	0.54	661	1.085
XRU-3/3m	0.932	1.178	0.33	544	1.086
10.7m	0.917	0.983	0.72	552	0.991
21m	0.925	1.157	0.44	548	1.075
Laboratory Shocked Coral/0.2GPa	0.907	1.468	0.71	559	1.212
4.4GPa	1.280	4.098	0.99	396	2.024
7.1GPa	1.047	14.889	0.99	484	3.859
7.9GPa	1.032	12.687	0.99	491	3.562
10.6GPa	2.280	7.701	0.93	222	2.775
Unshocked Single Crystal Aragonite	0.931	0.871	0.47	544	0.933
Shocked Single Crystal Aragonite/8.1GPa	1.090	2.059	0.94	465	1.435

(Fig. 4-5) is drawn as a dashed line in plots of the XC-1 and XC-2 data (Figs. 4-3 and 4-4, respectively), for comparison purposes. Figure 4-8 compares linear fits for laboratory shocked single and polycrystalline aragonite. Crystallite sizes and r.m.s. strain values for XC-1, XC-2 and laboratory shocked coral samples are plotted in Figs. 4-9, 4-10 and 4-11, respectively. Lines drawn through size and strain points are only visual estimates of data trends.

Before Figs. 4-9 to 4-11 are discussed in detail, a work of caution with regard to the tabulated crystallite size values is warranted. Variances calculated in this study have not been corrected for instrumental broadening effects. Attempts were made to experimentally determine the pure diffraction profile, however no consistent results were obtained. Therefore, instead of presenting variance data corrected on a rather arbitrary basis, uncompensated values are tabulated. To offer an order of magnitude estimate of the corrected parameters, the variance of the (111) diffraction peak of chemically pure, unstrained silicon powder was calculated, and subtracted from the net variance calculated for X-ray peaks of the 10.7 m XRU-3 sample. (Again, the additive property of the variance allows such straightforward manipulation.) The crystallite size determined from this corrected variance was 1470 Å, or a factor of 2.7 larger than the uncorrected size. Therefore, the tabulated crystallite sizes are within an order of magnitude of probable true sizes. The r.m.s. strain was essentially unaltered by this correction.

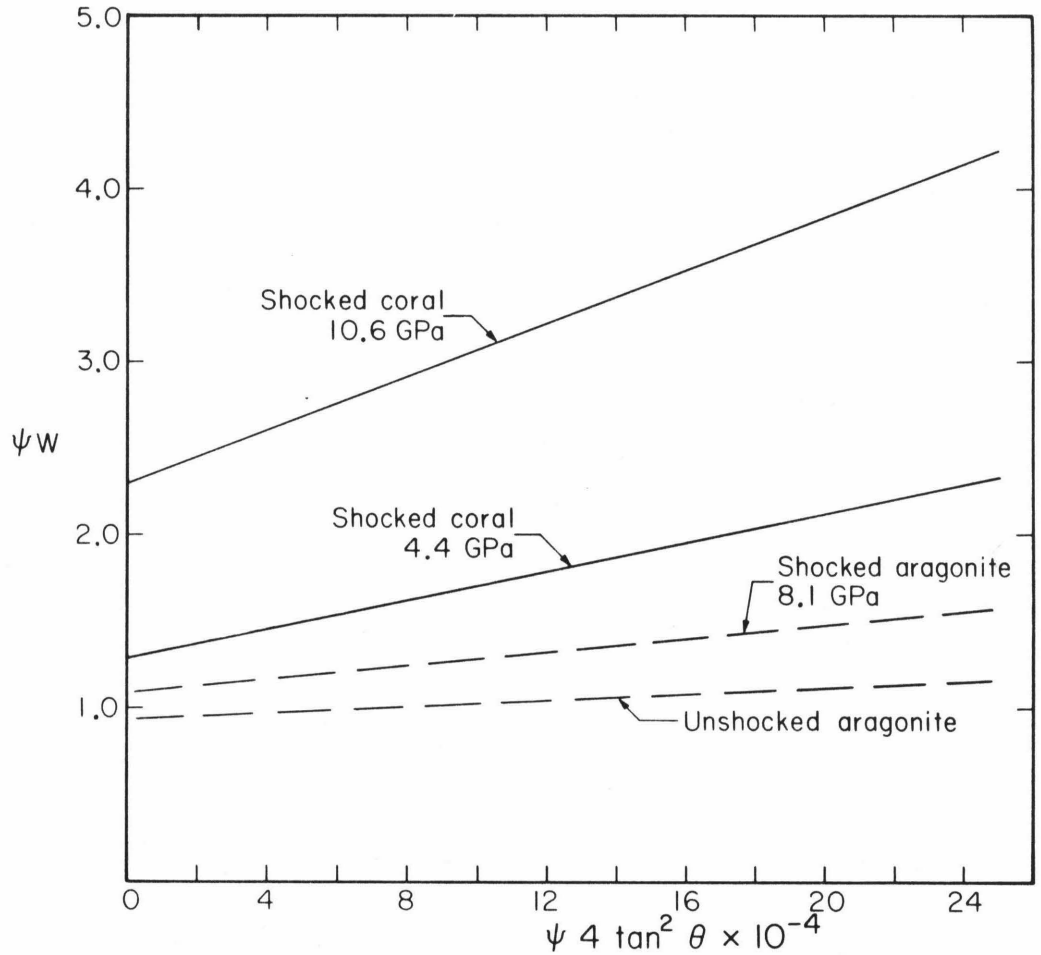

Figure 4-8. Comparison of linear least squares fits to unshocked and laboratory shocked single and polycrystalline (i.e., coral) aragonite data, in a ψW versus $\psi 4 \tan^2\theta$ (x 10^{-4}) plot.

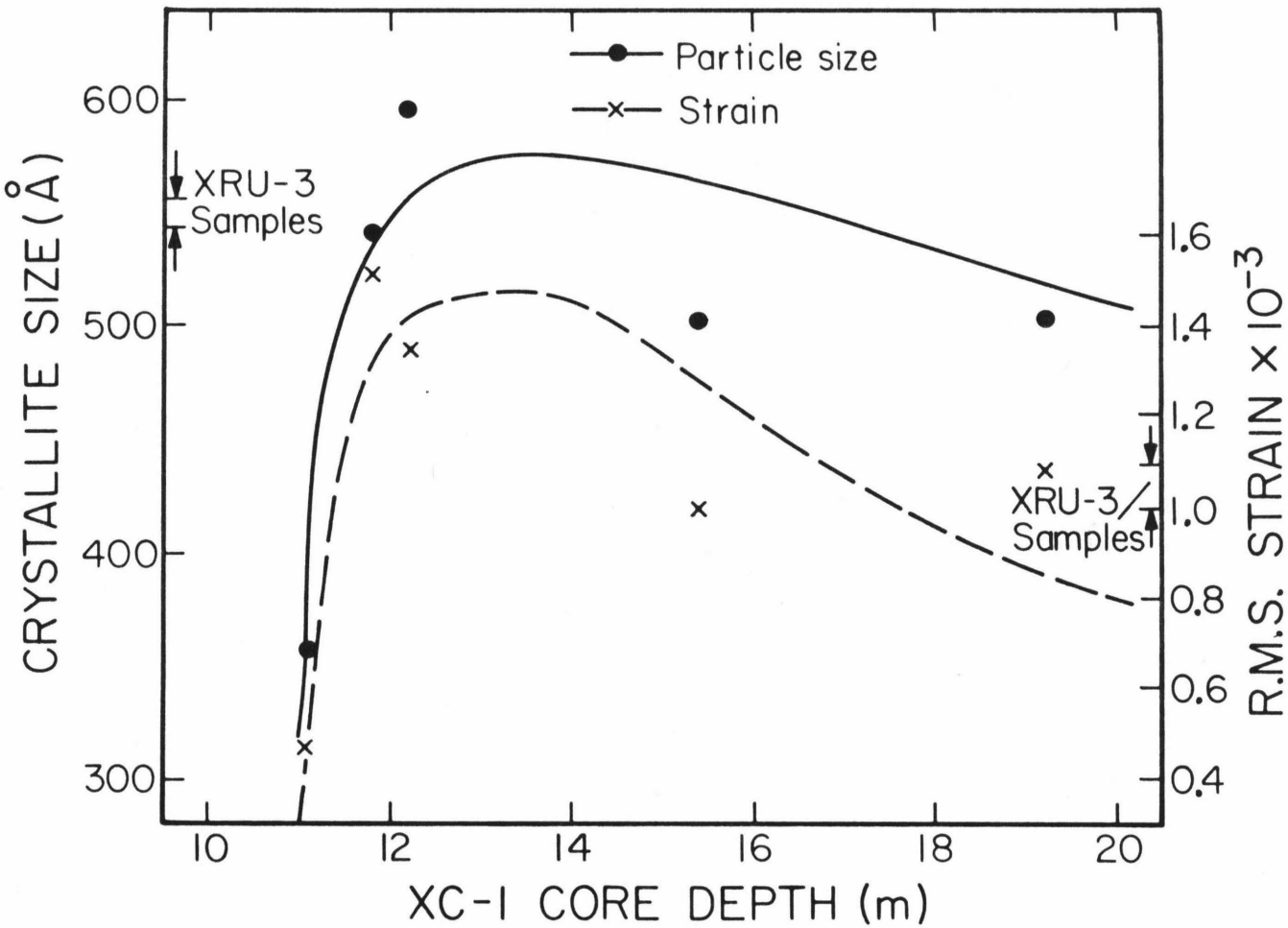

Figure 4-9. Aragonite crystallite size and root mean square (R.M.S.) strain values, calculated using data in Fig. 4-3 (see text), for XC-1 core samples from various depths. XRU-3, i.e., control core, sample values are indicated along the size and strain axes.

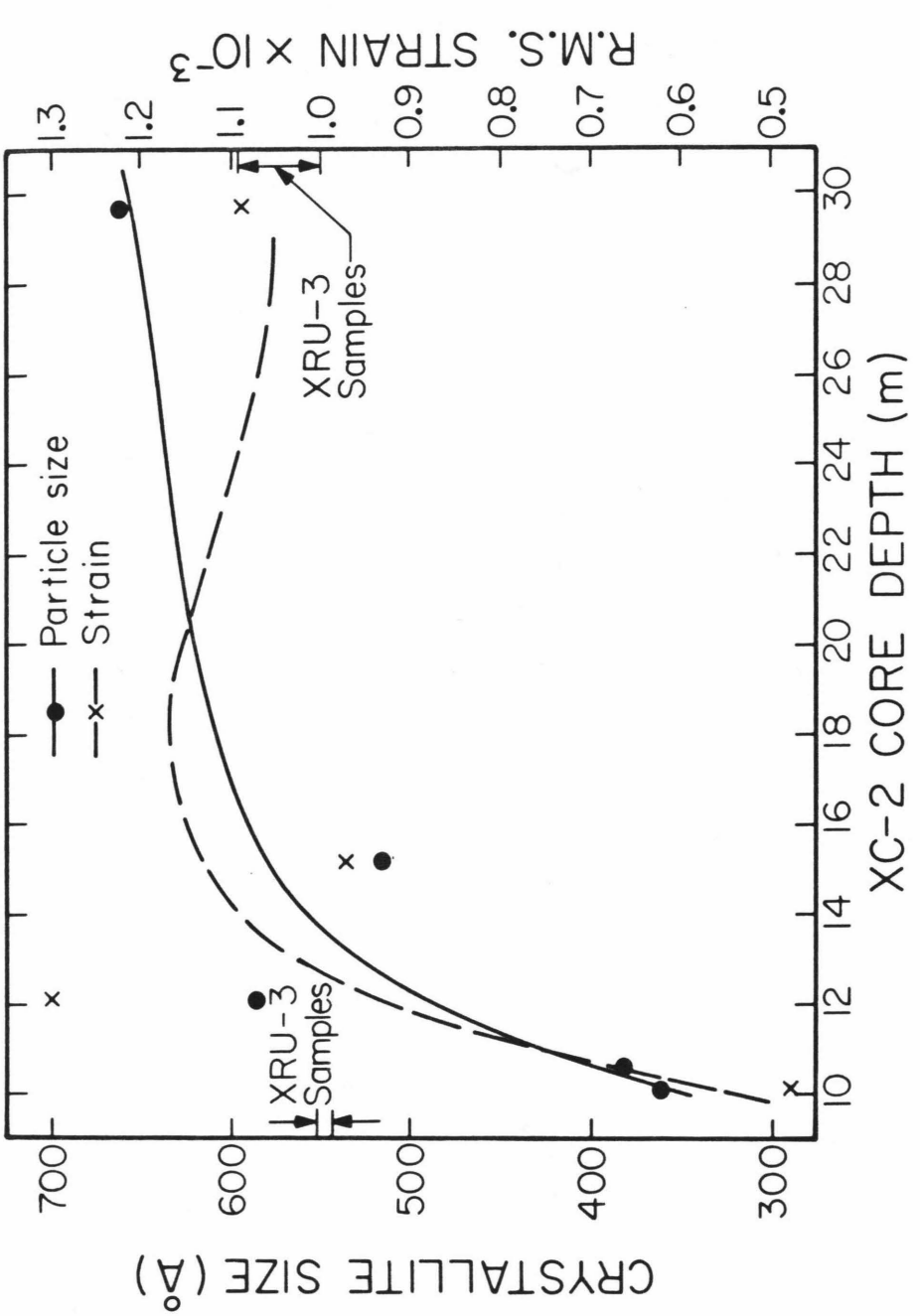

Figure 4-10. Plot of aragonite crystallite size and strain values for XC-2 core samples. The range of XRU-3 sample values are indicated along the size and strain axes.

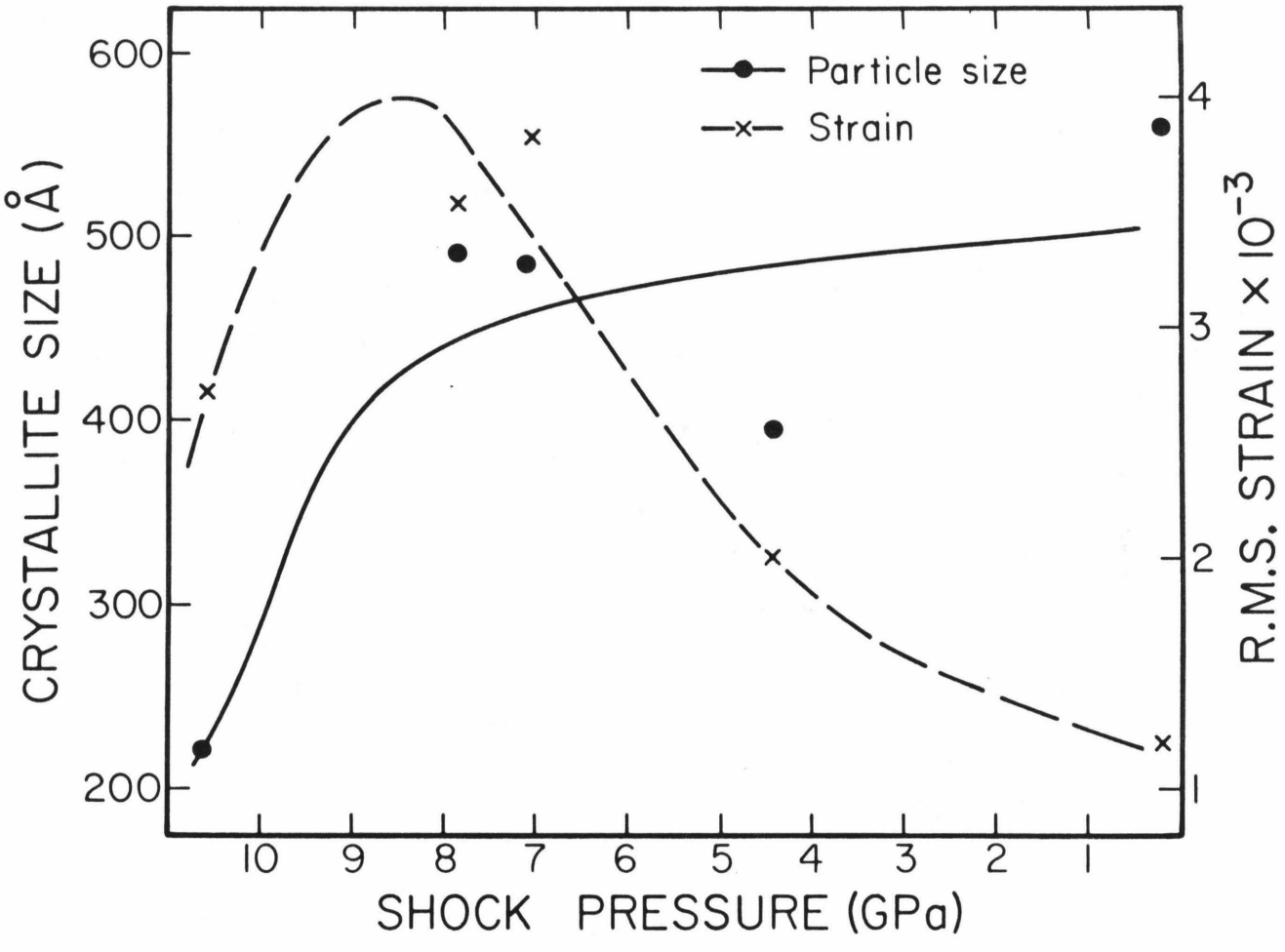

Figure 4-11. Plot of aragonite crystallite size and strain values for laboratory shocked coral core samples. Shock pressure axis reversed (i.e., values increase to the left) for easier comparison with Figs. 4-9 and 4-10.

Discussion

Plots of ψW against $\psi 4 \tan^2\theta$ (X 10^{-4}), presented in Figs. 4-3 through 4-8, provide a concise, graphic illustration of the crystallite sizes and strains of various samples; the y-intercepts, indicated by oversized symbols, are inversely proportional to crystallite sizes, and the slopes of the linear least square fits are directly proportional to sample strains.

Consider first the explosively and laboratory shocked coral samples; peak broadening data for the aragonite in these samples is illustrated in Figs. 4-3, 4-4 and 4-6. Figure 4-5 presents results for 3 samples from different depths in the control XRU-3 core, drilled approximately 100 m outside Cactus Crater (see Fig. 3-2). Note the similarity in size and strain values for all three samples. XC-1 sample results are shown in Fig. 4-3, together with the average linear fit of the XRU-3 data, sketched as a dashed line. Samples from 19.2 and 15.4 m levels show slopes, and consequently, strain values, very similar to that of the XRU-3 data. Results for the 12.2 m sample suggest a somewhat larger strain value, and those for the 11.8 m sample, a yet larger value. The variability of the y-intercepts for these 4 samples, corresponding to a 500 Å to 600 Å crystallite size range (see Table 4-2), is encompassed by the accuracy limits of the analytical method; thus, crystallite sizes for these samples do not show a significant variation. The XC-1, 11.1 m sample shows distinctly different results. Crystallite size is significantly reduced to 357 Å, and the strain value is even smaller than that of the control XRU-3 sample average. XC-2 sample data show a similar pattern (Fig. 4-4). Deeper sample (29.7 and 15.2 m) data resemble the

XRU-3 results, whereas the intermediate sample (12.2 m) indicates somewhat larger strain values. The two shallowest samples 10.1 and 10.6 m show significantly reduced crystallite sizes $\sim$ 370 Å and almost negligible residual strains. (The negative value of the slope for the 10.6 m sample does not, of course, have any physical significance, and is interpreted as indicating essentially no strain remaining in the sample.)

As discussed in Chapters 3 and 5, the shallowest samples from the XC-1 and XC-2 cores experienced the highest shock pressures generated in the core samples by the nuclear explosion. Since both the decrease in crystallite size (mosaicism) and increase in strain are expected to vary directly with increasing shock-induced deformation (see e.g., Heckel and Youngblood, 1968; Sawaoka et al., 1979), it is expected that the most highly shocked samples would show the largest amount of mosaicism and residual strain. Instead, what is observed in the shallowest XC-1 and XC-2 samples is a significant decrease in crystallite size and, surprisingly, an extreme reduction in strain.

Results from laboratory shocked coral samples, shown in Fig. 4-6, may lend insight into the unexpected results from the Cactus core samples. In this figure, numbers in the right hand portion of the graph indicate experimental shock pressures in GPa; the average fit to unshocked coral data (Fig. 4-5) essentially coincides with that to the 0.2 GPa shocked sample. As observed in this graph, samples shocked to pressures below 8 GPa show similar crystallite sizes and a relatively consistent increase in strain with increasing shock pressures. The sample shocked to 10.6 GPa shows a significant increase in mosaicism and decrease in strain.

Therefore, explosively and laboratory shocked coral samples indicate the same qualitative trend: residual strain increases with increasing shock pressures (for the laboratory shocked samples) and decreasing sample depths (for the XC-1 and XC-2 samples) until some threshold pressure value is reached, resulting in a discontinuous decrease in both crystallite size and strain. Calculated crystallite sizes and strains for XC-1, XC-2 and laboratory shocked coral samples are plotted in Figs. 4-9, 4-10 and 4-11, respectively. Curves through size and strain data points are a visual fit and approximately conform to the discontinuous mosaicism-strain deformation model just described. Note that, in all 3 graphs, particle size is approximately constant except for the most highly laboratory shocked or shallowest core samples, where it is distinctly smaller. Strain values undergo modest increases toward shallower depths of XC-1 and XC-2 samples, then discontinuously decrease at the shallowest available sample level. The gradual strain increase with pressure, and discontinuous decrease after some threshold value is best illustrated in the laboratory shocked sample plot in Fig. 4-11.

Before deliberating further on the observed discontinuous mosaicism-strain patterns, the single crystal aragonite results will be briefly discussed. Data from unshocked and laboratory shocked (to 8.1 GPa) samples are presented in Fig. 4-7. Linear least squares fits to these data, as well as to several laboratory shocked coral samples, are sketched in Fig. 4-8. In this figure, the line labelled "Unshocked aragonite" represents both single crystal and coral samples. Note that the 8.1 GPa shocked aragonite data show smaller strain and larger crystallite size values, i.e. indicates a lower intensity of deformation,

than the coral sample shocked to approximately half the pressure (the 4.4 GPa sample). The significant conclusion from the comparison is that the extent of detectable shock deformation critically depends on the nature of the sample; specific controlling parameters include polycrystallinity and porosity. Therefore, in determining shock pressure versus crystallite size and strain curves, the porosity and initial grain size of the shocked samples being compared must be taken into account.

Returning to the discontinuous mosaicism-strain patterns observed in shock deformed aragonite, consider first the data set that best illustrates that pattern, i.e. the laboratory shocked coral data, shown in Figs. 4-6 and 4-11. As discussed earlier, the pattern indicates strain increasing with shock pressure until some threshold value, after which strain and particle size are both substantially reduced. In static deformation studies, strain reduction is typically accomplished by heating a material; the annealing process not only reduces strain but often initiates recrystallization as well (see, e.g. Gross, 1965). However, this annealing process is accomplished on time scales considerably longer than those pertinent to shock experiments, and at much higher temperatures. For example, in annealing experiments on statically deformed calcite, Gross (1965) reports complete recovery after heating for several hours at about 600°C. A maximum estimate of the post-shock temperature for aragonite shocked to 8 GPa assumes no energy is taken up in the release process, and is calculated from:

$$\int_{T_0}^{T_R} Cp(T)dT = \Delta E \qquad (4\text{-}8)$$

where T_R and T_0 are the post-shock and initial (298 K) temperatures, respectively, and Cp(T) is the temperature dependent heat capacity function from Robie et al., 1978. Considering the steep release adiabats in this pressure region (see Fig. 6-4) such an estimate is not unreasonable. ΔE is calculated from the Rankine-Hugoniot equation:

$$\Delta E = E_H - E_0 = 1/2\ P_H \left(\frac{1}{\rho_0} - \frac{1}{\rho_H} \right) \qquad (4\text{-}9)$$

where subscripts H and 0 indicate Hugoniot and initial conditions, respectively. According to this estimate, the maximum temperature increase in aragonite shocked to 8 GPa is approximately 100°, which, by comparison to annealing studies under static conditions, is entirely inadequate to initiate strain recovery or recrystallization. In addition, it is intuitively expected that such temperature annealing would be a continuous rather than discontinuous phenomenon.

It is proposed here that the discontinuous mosaicism-strain patterns observed in shock deformed aragonite are a consequence of shock induced phase changes. Specifically, the process is envisaged as follows: Aragonite shocked to a pressure at or above that at which the mineral begins to undergo a phase transition, undergoes at least a partial transformation to the high pressure phase. During the release process, the high pressure phase is no longer stable, and recrystallization to the low pressure phase occurs. The crystallite size of this re-formed low pressure phase is substantially reduced reflecting either mosaicism introduced during the compression and transformation process or recrystallization kinetics acting during the rarefaction process. Due to recrystallization, any strains introduced during shock compression are annihilated. This process is schematically depicted in

Fig. 4-12. Therefore, assuming this model is correct, an aragonite phase change at shock pressures between 7.9 and 10.6 GPa is predicted (see Fig. 4-6 and 4-11). In Chapter 6, a low pressure phase change in single crystal aragonite is reported to occur at shock pressures of 6.6 ± 1 GPa. Considering the differences in the nature of the samples used and the experimental methods (thermodynamic paths in recovery and equation of state shock experiments differ slightly), these two pressure estimates can be considered as corresponding to the same phase transition.

In previous discussion, similarities in the qualitative mosaicism-strain patterns of laboratory shocked and XC-1 and XC-2 sample data were emphasized. However, considering the large differences in actual crystallite size and strain values between the laboratory shocked and Cactus Crater samples, results from the latter sample sets cannot readily be explained by the mechanism described above, i.e., a phase transition at pressures of $\sim$ 7 to $\sim$ 10 GPa. As listed in Table 4-2, crystallite sizes calculated for the shallowest XC-1 and XC-2 samples are comparable to those of the 4.4 GPa laboratory shocked sample (350 to 400 Å); however, strain values are significantly different, those of the Cactus samples being distinctly smaller.

A correlation of Cactus Crater and laboratory shocked data is complicated by several factors, the most significant of which is probably the water-saturated condition of Cactus Crater samples both during and after shock deformation. Two water-saturation dependent theories to explain the Cactus Crater sample data are offered:

1) The shallowest samples from cores XC-1 and XC-2 were shocked to pressures below the onset of the 7 to 10 GPa phase transition,

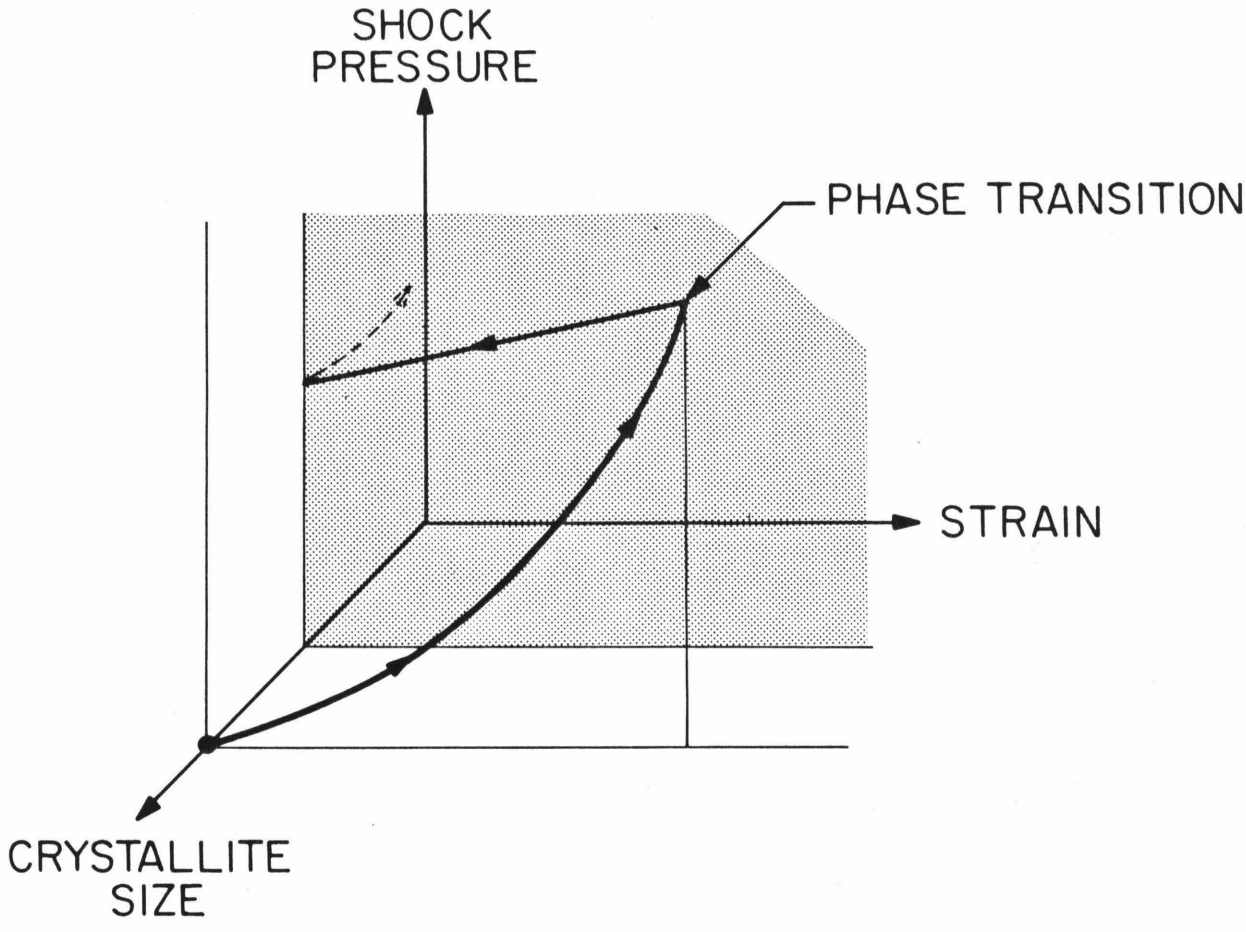

Figure 4-12. Schematic of model proposed to explain observed size and strain effects in explosively and laboratory shocked aragonite. With increasing shock pressure, strain progressively increases (crystallite size remaining approximately constant) up to a pressure at which a phase transition occurs. At this point, strain is reduced and crystallite size discontinuously decreases.

and were deformed mainly by the strain mechanism; recrystallization of the strained mineral was facilitated by the stored strain energy (see e.g., Newton et al., 1969) and by the aqueous environment.

2) These samples had been shocked to pressures above the phase transition; however, recrystallization in a water-saturated environment resulted in larger crystallite sizes than those observed for laboratory shocked samples.

Three water-saturation independent hypotheses are offered:

3) The shallow level Cactus Crater samples experienced a shock deformation history similar to that described for the laboratory shocked samples, and the quantitative crystallite size-strain differences reflect differences in durations of nuclear explosion and laboratory produced shock pulses.

4) The mosaicism-strain discontinuity observed in XC-1 and XC-2 sample results is due to a phase transition occurring at shock pressures below 4.4 GPa, and above the Hugoniot elastic limit, which, as reported in Chapter 6, occurs at 2.0 ± 0.5 GPa in single crystal aragonite. It is interesting to note that, in Chapter 6, a phase transition at 3.3 GPa is speculated.

5) The size-strain discontinuity in the Cactus core samples reflects the elastic-plastic transition; the shallowest samples therefore, have been shocked above pressures of approximately 2 GPa.

Explanation 4 and 5 are favored because of their consistency with the aragonite equation of state data reported in Chapter 6 and the ESR based peak pressure estimates for these samples of 4.5 ± 0.5 GPa. Although, as far as we are aware, the phase transition effects on

mosaicism-strain data reported here have not been previously observed, Paterson (1959) predicted anomalously large X-ray peak broadenings due to phase changes.

A strain energy, U, can be calculated from the mean square strains, $\langle e^2 \rangle$, determined from peak broadening analysis. Faulkner (1960) calculated the following strain to strain energy relationship for an isotropic material, assuming isotropic stress distributions:

$$U = \frac{15E}{2(3-4\nu + 8\nu^2)} \langle e^2 \rangle \qquad (4\text{-}10)$$

where E and ν are Young's modulus (GPa) and Poisson's ratio, respectively (Voigt-Reuss averages). Using E = 90.7 GPa, ν = 0.177 (from Simmons and Wang, 1971) and an aragonite density of 2.93 g/cc, a strain energy of 1.4×10^{-3} kjoule/g is calculated for the most strained 7.1 GPa laboratory shocked sample; this value is approximately 2% of the energy introduced in shocking the sample to this pressure, as calculated using Eq. 4-9 and the aragonite Hugoniot reported in Chapter 6. In plastic deformation studies on metals, it is observed that a similarly small fraction, typically 1% to 15%, of the energy expended in deforming the material is stored as strain energy (Christian, 1965). The X-ray peak broadening technique, therefore, can potentially provide useful information on energy partitioning during explosion or impact processes.

Conclusions

X-ray peak broadening analysis using the variance method provides evidence that the shock compression and release process introduces both mosaicism, or crystallite size decrease, and strain deformation into the mineral aragonite. Polycrystalline, aragonite containing coral core

samples experimentally shocked to pressures of up to 10 GPa show maximum aragonite crystallite size decreases of 60% and 300% increases in strain; deformation in single crystal aragonite experimentally shocked to comparable pressures is less extreme. The deformation pattern, as depicted by the laboratory data and strongly suggested by explosively shocked coral, consists of a progressive increase in residual strain with increasing shock stress (crystallite size remaining approximately constant) until some threshold stress is achieved, after which strain and crystallite size are both discontinuously and substantially reduced. It is proposed that shock-induced phase changes are responsible for the mosaicism-strain discontinuities. According to the laboratory shocked coral results, a phase change in aragonite occurs at shock pressures of approximately 7 to 10 GPa. Explosively shocked Cactus Crater samples tentatively suggest another phase transition between approximately 2 and 4.4 GPa. Both these speculated phase changes are consistent with the aragonite Hugoniot data presented in Chapter 6. Thus, X-ray peak broadening analysis of shock metamorphosed material offers the potential of both resolving the nature of residual shock deformation and lending insight into shock pressure induced phase transitions.

References

Chao, E.C.T., E. M. Shoemaker and B. M. Madsen, First natural occurrence of coesite, Science, 132, no. 3421, pp. 220-222, 1960.

Christian, J. W., The Theory of Transformations in Metals and Alloys, Pergamon Press, Oxford, p. 710, 1965.

Dachille, F., P. Gigl and P. Y. Simons, Experimental and analytical studies of crystalline damage useful for the recognition of impact structures. In Shock Metamorphism of Natural Materials (eds. B. M. French and N. M. Short) Mono Book Corp., Baltimore, pp. 555-569, 1968.

Faulkner, E. A., Calculation of stored energy from broadening of X-ray diffraction lines, Phil. Mag., 5, p. 519-521, 1960.

Gross, K. A., X-ray line broadening and stored energy in deformed and annealed calcite, Phil. Mag. 12, (8th series) p. 801-813, 1965.

Hall, W. H., X-ray line broadening in metals, Proc. Phys. Soc., A62, p. 741-743, 1949.

Hanss, R. E., B. R. Montague, M. K. Davis and C. Galindo, X-ray diffractometer studies of shocked materials, Proc. Lunar Planet. Sci. Conf. 9th, p. 2773-2787, 1978.

Heckel, R. W. and J. L. Youngblood, X-ray line broadening study of explosively shocked MgO and α Al_2O_3 powders, J. of the Am. Ceramic Society, 51, no. 7, p. 398-401, 1968.

Hörz, F. and W. L. Quaide, Debye-Scherrer investigations of experimentally shocked silicates, The Moon, 6, p. 45-82, 1973.

Klug, H. P. and L. E. Alexander, X-ray Diffraction Procedures, John Wiley and Sons, New York, 1974.

Levien, L. and T. J. Ahrens, Deformation mechanisms of shock compressed minerals (abstract) EOS, (Trans. AGU) 61, p. 378, 1980.

McQueen, R. G., J. C. Jamieson, and S. P. Marsh, Shock-wave compression and X-ray studies of titanium dioxide, Science, 155, p. 1401-1404, 1967.

Minkin, J. A. and E.C.T. Chao, Single crystal X-ray investigation of deformation in terrestrial and lunar ilmenite, Proceedings of Second Lunar Science Conf., Vol. 1, pp. 237-246, 1971.

Newton, R. C., J. R. Goldsmith and J. V. Smith, Aragonite crystallization from strained calcite at reduced pressures and its bearing on aragonite in low-grade metamorphism, Contr. Mineral and Petrol. 22, p. 335-348, 1969.

Offield, T. W. and H. A. Pohn, Geology of the Decaturville impact structure, Missouri, U.S.G.S. Professional Paper 1042, 1979.

Paterson, M. S., X-ray line broadening in plastically deformed calcite, Phil. Mag., 4, (8th series) p. 451-466, 1959.

Robie, R. R., B. S. Hemingway and J. R. Fisher, Thermodynamic properties of minerals and related substances at 298.15 K and 1 bar (10^5 pascals) pressure and at higher temperatures, Geol. Survey Bull. 1952 p. 300, 1978.

Sawaoka, A., K. Kondo and T. Akashi, Effects of shock compression on α - Al_2O_3 and MgO powders, Report of the Research Lab. of Engineering Materials, T.I.T., no. 4, p. 109-115, 1979.

Schneider, H., Mechanical deformation and structural state of experimentally shock-loaded oligoclases, N. Jb. Miner. Mh., 6, pp. 255-269, 1977.

Schneider, H. and V. Hornemann, The disproportionation of andalusite (Al_2SiO_5) to Al_2O_3 and SiO_2 under shock compression, Phys. Chem. Minerals, 1, p. 257-264, 1977.

Simmons, G. and H. Wang, Single Crystal Elastic Constants and Calculated Aggregate Properties: A Handbook, MIT Press, Cambridge, Mass. p. 304, 1971.

Warren, B. E. and B. L. Auerbach, The effect of cold-work distortion on X-ray patterns, J. of Applied Physics, 21, pp. 595-599, 1950.

Chapter 5

STRUCTURE OF CACTUS CRATER AND IMPLICATIONS FOR CRATERING IN CARBONATE ROCKS

Introduction

Because of their stratified nature, sedimentary rocks, acting as target media for impact or explosion craters, offer favorable circumstances for detailed crater structure investigations. Meteorite impact craters in sedimentary rocks readily display deformational features such as folded and faulted central peaks (e.g. Sierra Madera; Howard et al., 1972), rim deformation and ring faults (e.g. Decaturville; Offield and Pohn, 1979), and fallback and autochthonous breccia lenses (e.g. Gosses Bluff and Meteor Crater; Milton et al., 1972 and Shoemaker, 1963). Explosion craters in stratified targets, such as Snowball (Roddy, 1976), provide evidence of similar cratering produced features. Laboratory scale cratering experiments, using colored, layered targets, (see e.g. Gault, 1968) corroborate the observed large scale phenomena. Nevertheless, sedimentary crater (especially meteorite crater) structural observations are often sketchy and do not permit comprehensive analyses of impact induced deformation. In particular, data on the variety of possible sedimentary lithologies, with saturation and stratification as additional variables, are needed in order to allow a numerical assessment, or, at least, a qualitative synthesis, of the effect of target properties on crater morphologies.

The purpose of this study is two-fold. First of all, an attempt is made to present an accurate, detailed description of an explosion crater in a water-saturated carbonate rock. As an addition to the available data base, such a description would aid in formulating a rigorous theoretical treatment of crater structural dependence on target characteristics. Secondly, detailed observations of the crater are used to infer cratering excavation and modification mechanisms, and these interpretations are then compared with theoretically and observationally based cratering models.

Cactus Crater, described in the introductory and third chapters, is the object of this study. In the case of Cactus, insight into the details of crater structure is provided by a unique stratigraphic tracer, the diagenetic transition boundary between high and low magnesium calcite (described in the next section). This stratigraphic marker, together with other geochemical data, also serves as the basis for interpretation of cratering mechanisms responsible for the formation of Cactus Crater.

Carbonate Mineralogy - Background

Pertinent aspects of the mineralogy, formation and alteration history of organically precipitated carbonate minerals are presented in this section.

As described in Chapter 3, the lithology of Runit core samples consists of coral and coralgal limestones. X-ray diffractometer spectra of samples from cores XC-1, XC-2, and 5 of the XRU series cores (see Fig. 5-1) reveal a mineralogy consisting almost exclusively of aragonite and calcite. The sole exception is a sample from the XRU-3 core, in which a small amount (< 10%) of quartz, probably aeolian in origin, is

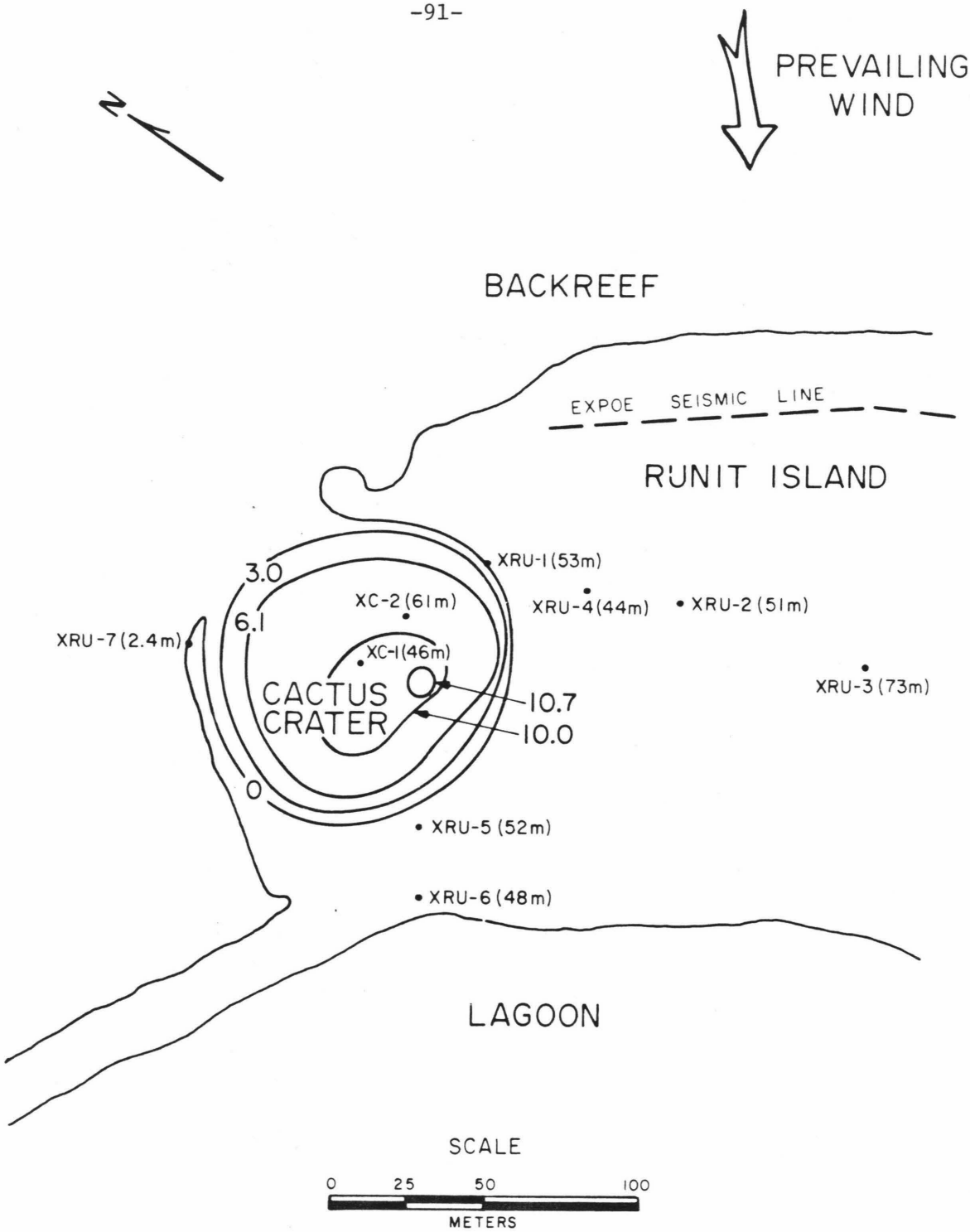

Figure 5-1. Map of Runit Island, Eniwetok Atoll (11.30°N, 162.15°E) showing positions of drillholes in cratered (XC) and uncratered (XRU) portions of the island. Cactus Crater contour levels are difference contours.
Dashed line indicates position of seismic refraction line.

present. As noted in Chapter 4, the aragonite composition in these samples is constant for the top 50 m of available core material. Calcite, on the other hand, undergoes a significant change in its major element, specifically magnesium, chemistry, discussed below, in this interval, and it is this diagenetic transition that serves as a stratigraphic control in the delineation of the structure of Cactus Crater. Ristvet et al. (1974) first reported the presence of this diagenetic boundary, i.e. the high to low magnesium calcite transition, at approximately 10 m depths on Eniwetok Atoll.

It has long been observed that organically precipitated carbonate skeletal materials contain relatively high concentrations of magnesium (see e.g. Silliman, 1846; Bøggild, 1930). Chave (1954a), in an extensive study on the magnesium distribution in the calcareous hard parts of a variety of marine organisms, reported the incorporation of up to 30 weight % magnesium carbonate. (The maximum figure represents $MgCO_3$ concentrations by certain calcareous algae.) In general, the phylogenetic level of the carbonate secreting organism and the temperature of the water in which it lived, were found to be the factors controlling the magnesium content of the precipitated mineral.

In 1952, Chave showed that the magnesium is present in the mineral calcite, and not dolomite, as earlier believed. In that study, $MgCO_3$ concentrations, determined by chemical analyses, were compared with X-ray diffraction spectra of the same samples. The results, shown as the solid line in Fig. 5-2, indicate a continuous decrease in the (104) d spacing of the calcite lattice with increasing $MgCO_3$, up to the observed limit of 30 weight % $MgCO_3$. (Dashed portions represent

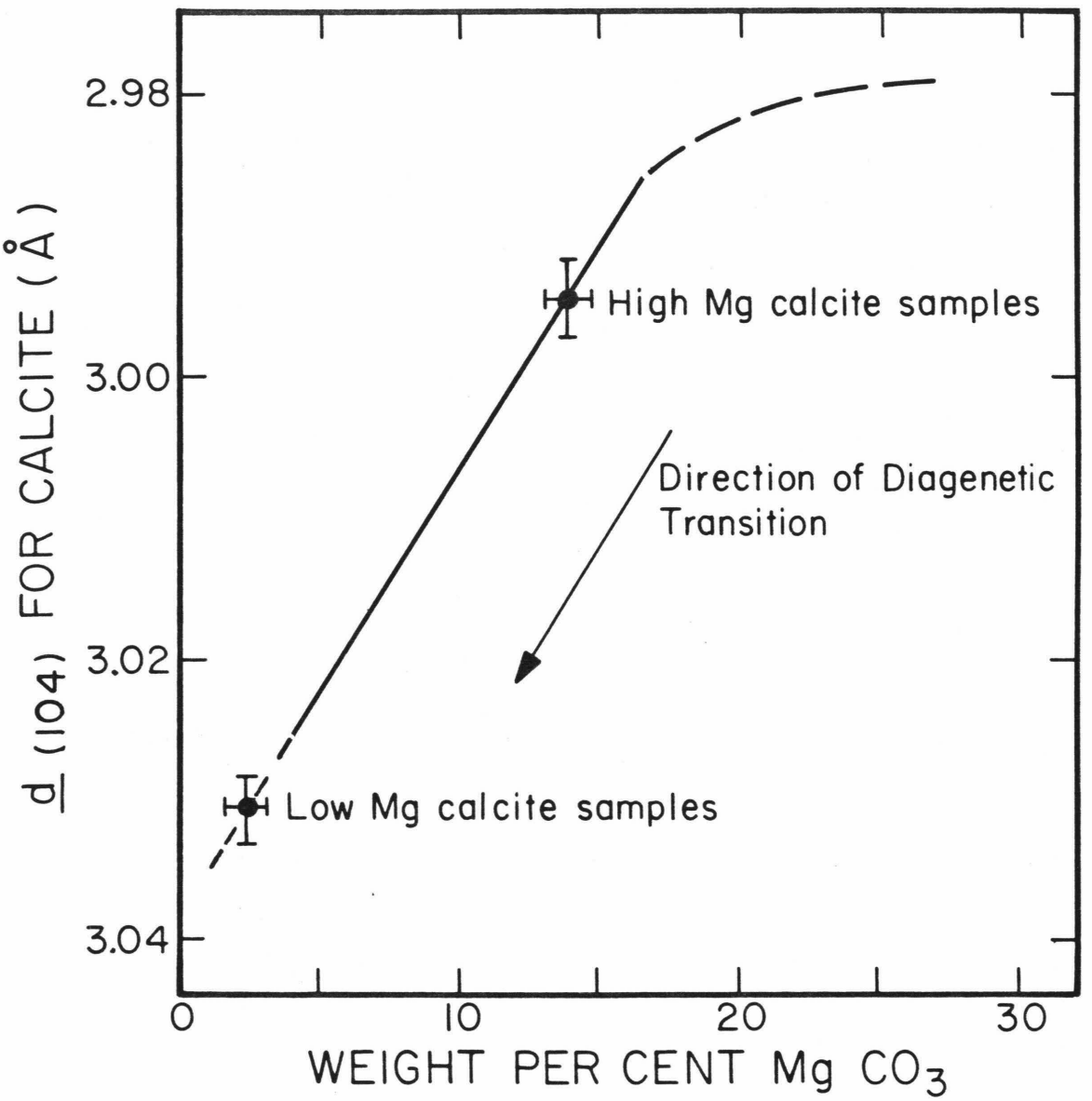

Figure 5-2. Curve relating chemically determined weight % $MgCO_3$ and the (104) d spacing calculated from powder X-ray diffractometer scans of magnesian calcites; dashed portions represent considerable data scatter. (From: Chave, K.E., "A solid solution between calcite and dolomite", J. Geology, 60, 190-192, 1952). Points representing the range of d spacings observed for the high and low Mg calcites in Runit core samples are indicated. These variations were translated to represent compositional variations.

considerable data scatter.) Reflections corresponding to the dolomite, $CaMg(CO_3)_2$, structure (d_{104} = 2.89 Å) and, hence, composition were not observed. Chave referred to this compositional variation as a solid solution between calcite, $CaCO_3$, and dolomite, $CaMg(CO_3)_2$. Goldsmith, Graf and Joensuu (1955) pointed out that such a designation, while compositionally acceptable, does not take into account structural considerations. Dolomite is an ordered structure composed of alternating calcium and magnesium planes, while the magnesium ions in magnesian calcite are randomly situated. Progression from magnesian calcite to a true dolomite phase would require, therefore, a reordering process.

Inorganically precipitated calcite, on the other hand, is typically observed to contain less than 2 weight % $MgCO_3$ (Chave, 1952). Subsolidus phase equilibrium studies in the system $CaCO_3$-$MgCO_3$ indicate limited solid solution between the two phases. Figure 5-3, from Harker and Tuttle (1955), shows that even at temperatures of 500°C, less than 6% $MgCO_3$ is stable in the calcite structure. Organically precipitated calcite with $MgCO_3$ concentrations of up to 30%, is, therefore, unstable at near surface conditions, excluding, of course, the biological environment in which it was produced. Thus, it is inevitable that, given sufficient time, magnesian calcite will alter to a more stable form. The stratigraphic record bears evidence to this statement (Chave, 1954b).

Three methods of stabilization of magnesian calcites have been proposed (Land, 1967): a solid state exsolution reaction:

$$\text{Mg calcite} \rightarrow \text{calcite} + \text{dolomite}, \qquad (5\text{-}1)$$

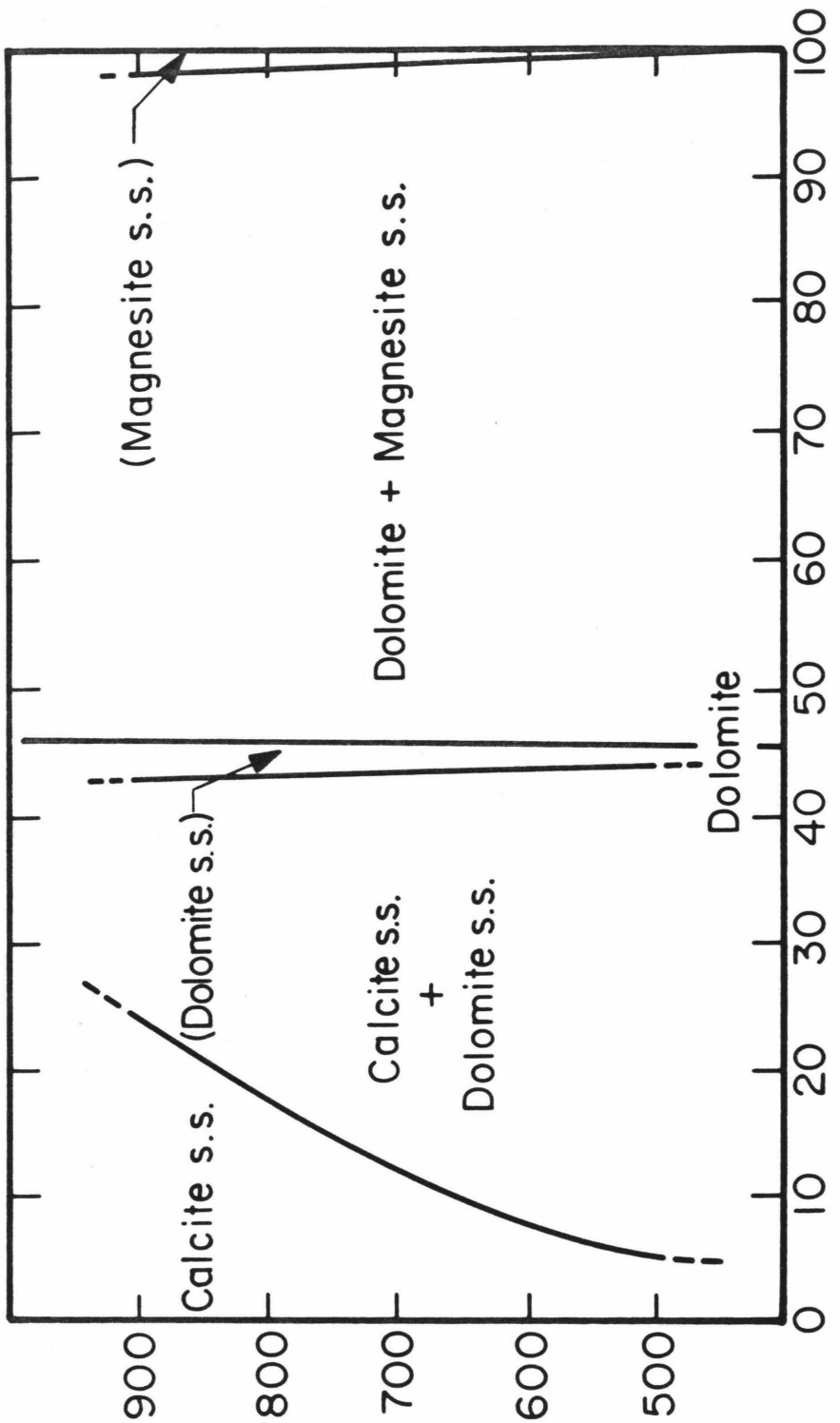

Figure 5-3: Phase diagram for the system $CaCO_3$-$MgCO_3$ depicting limited Mg solid solution in the calcite structure, especially at lower temperatures. (From: Harker, R. I. and Tuttle, O. F., "Studies in the system CaO-MgO-CO_2", Am. J. of Science, 253, 274-282, 1955).

replacement by dolomite or a non-carbonate phase, or dissolution, according to the following reaction:

$$(Ca_{1-x}Mg_x)CO_3 \text{ (calcite)} + xH^+(aq) \rightleftarrows (1 - x)CaCO_3 \text{ (calcite)} + xMg^{++}(aq) + xHCO_3^-(aq) \qquad (5\text{-}2)$$

resulting in calcite and a magnesium enriched solution. The total absence of dolomite in any of the Eniwetok samples investigated in this study supports the third mechanism as the relevant stabilization means in this instance. The dissolution of magnesian calcite to calcite is observed to be a texturally non-destructive reaction occurring in the meteoric vadose zone; absolute reaction rates are not known, but in relative terms, magnesian calcite stabilization precedes that of aragonite.

On coral atolls, conditions favorable to magnesian calcite diagenesis by dissolution occur during times of subaerial exposure correlative with episodes of major glaciations. It has been generally assumed that the magnesian calcite diagenetic transition boundary produced under such conditions is a sharp discontinuity. Results on the detailed nature of this transition, as observed on Runit Island, are discussed in the following section.

Observations

A detailed examination of the calcite mineralogy of samples from five of the cores drilled outside Cactus Crater, XRU-1, 3, 4, 5 and 6, (see Fig. 5-1) was conducted using powder X-ray diffractometry. Sample preparation and X-ray diffraction details are presented in Appendix II.

The X-ray spectra indicate the presence of two distinct calcite compositions. In samples from deeper (below 15 m) levels of these cores, the strongest calcite reflection (corresponding to the (104) plane) is

observed to occur between 2θ values of 29.43° and 29.48°, corresponding to d spacings of 3.032Å and 3.027Å, respectively. According to the relation between weight % $MgCO_3$ and $d_{(104)}$ spacings (hence 2θ values) determined by Chave (1952) and reproduced in Fig. 5-2, reflections in this range correspond to $MgCO_3$ concentrations of 2.3 ± 0.8 weight %. Judging from the considerable scatter in Chave's data at $MgCO_3$ contents less than 3%, the actual variability in $MgCO_3$ content may be somewhat larger than this; however, it almost certainly does not exceed 4 weight %. The (104) calcite reflection in samples from shallower core levels occurs between 29.81° and 29.83° 2θ, corresponding to $MgCO_3$ concentrations of 13.8 to 14.5 weight %. $MgCO_3$ calcite contents intermediate between 2.3 ± 0.8 weight % and 14.15 ± 0.35 weight % (hereafter referred to as low and high Mg calcite) were not observed. As discussed in the section on carbonate mineralogy, many organisms metastably precipitate calcite with relatively high $MgCO_3$ concentrations, which, upon subaerial exposure, transforms to calcite with low $MgCO_3$ contents; this phenomenon is clearly illustrated by the XRU core samples. The high Mg calcite in our Runit samples probably represents skeletal material of foraminifera and calcareous algae. These organisms have been identified in other Runit core samples (Cough et al., 1975), and the observed $MgCO_3$ concentrations in calcite are consistent with those reported by Chave (1954a) for skeletal material of tropical water foraminifera and calcareous algae.

The significant observation to be made in the Runit core studies is the nature of the high to low Mg calcite transition. There were no samples from any of the XRU cores that contained both high and low Mg

calcite. Therefore, within sampling interval limitations, magnesian calcite diagenesis on Runit Island (and, most likely, on all of Eniwetok Atoll) occurs as an abrupt transition. Depths to this transition reflecting the relative sea level stand during the last glaciation, in the XRU cores are listed in Table 5-1. Differences in these depth levels may be a result of transectionally varying hydrologic regimes, or of the blast that produced Cactus Crater; these possibilities will be discussed in the next section.

The nature of the high to low Mg calcite transition, as observed in samples from the cores drilled inside Cactus Crater, XC-1 and XC-2, markedly differs from that observed in the XRU cores taken outside the crater. Both high and low Mg calcite X-ray diffraction peaks were observed in several samples from shallow (above 20 m) levels in the XC-1 and XC-2 cores. X-ray powder diffraction spectra of the 5 shallowest available XC-1 samples are shown in Fig. 5-4. Peaks of both high Mg and low Mg calcite, at $\sim 29.8°$ and $\sim 29.5°$ 2θ, respectively, are present in the uppermost four of these samples. That of high Mg calcite, most prominent at the shallowest level, gradually decreases in intensity, while that of low Mg calcite increases in intensity with increasing depth in the core. At 15.4 m, and all levels below that, only low Mg calcite is observed. X-ray spectra of XC-2 core samples, reproduced in Fig. 5-5 show a similar pattern of consistently decreasing high Mg calcite and increasing low Mg calcite peak intensities. Below 20 m depth in XC-2, only the low Mg calcite peak is present.

Quantitative Analysis

Relative concentrations of high and low Mg calcite can be

Table 5-1

RUNIT DIAGENETIC TRANSITION DEPTHS

Core	Depth to High-to-Low Mg Calcite Transition (m)
XRU-1	13.7 ± 1.3
XRU-3	11.1 ± 0.5
XRU-4	13.6 ± 0.4
XRU-5	12.1 ± 1.0
XRU-6	13.4 ± 0.6

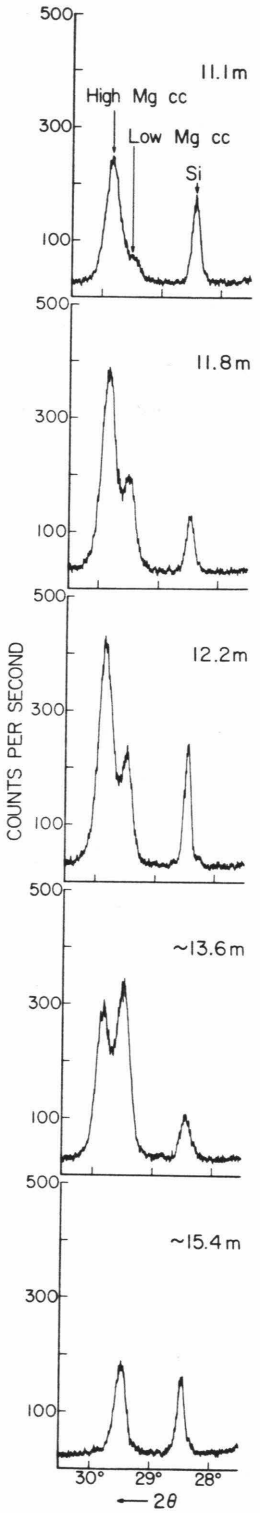

Figure 5-4. Portions of powder X-ray diffractometer scans of the five shallowest XC-1 core samples. Sample depth levels are indicated in the upper right hand corner. Note the progressive variation in high and low Mg calcite (cc) peak intensities with depth in the core. Si refers to the ( ) peak of metallic silicon used as an internal standard.

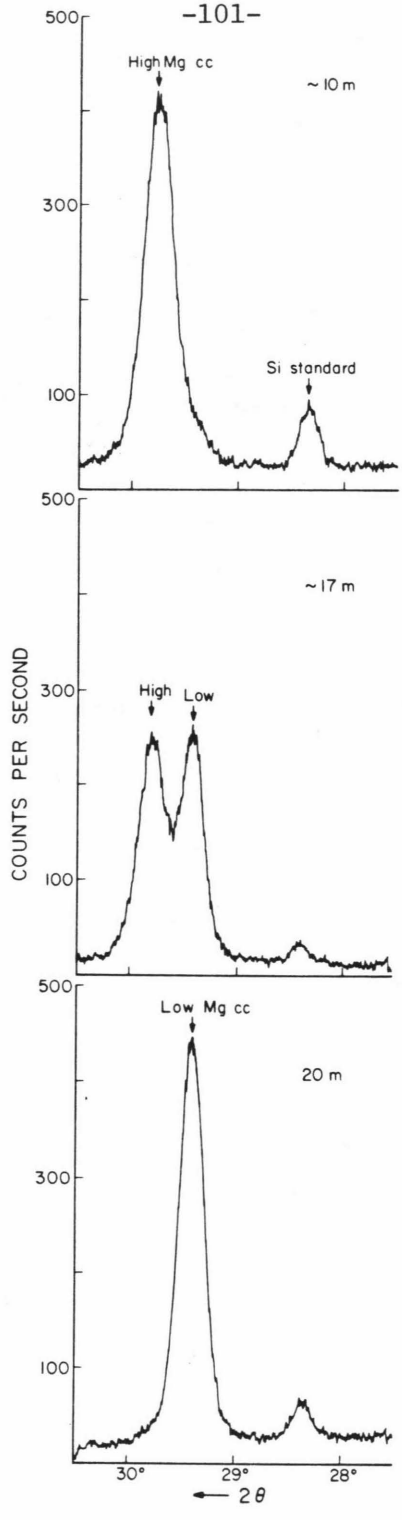

Figure 5-5. Powder X-ray diffractometer spectra of XC-2 core samples. Note the progression from high to low Mg calcite with increasing depth in the core, and the similarity of this variation to that of XC-1 core samples, shown in Fig. 5-3.

determined from X-ray powder diffraction spectra. The analysis involves resolution of high and low Mg calcite component peaks, calculation of integrated peak intensities, and comparison with an empirically derived composition versus peak intensity curve. Although the specific technique differs, the analysis presented below is analogous to that used by Neumann (1965).

Component peak resolutions and integral peak intensities were obtained in the following manner. Sections of X-ray diffractometer spectra between 28.5° and 30.5° 2θ, totally encompassing the high and low Mg calcite peaks, were digitized; additional 1° 2θ intervals on either side of these sections were used in determining a digitizing baseline. A least squares fit to the digitized data provided parameters A, B, C and D in the assumed Gaussian curve model:

$$I(2\theta) = A \exp\left[-B^2 (2\theta - \omega)^2\right] + C \exp\left[-D^2 (2\theta - \omega - \Delta)^2\right] \quad (5\text{-}3)$$

where $I(2\theta)$ is the peak intensity at some angle 2θ and Δ is the angular separation of the high and low Mg calcite peaks. ω is the centroid of the high Mg calcite peak:

$$\omega = \frac{\Sigma 2\theta \cdot I(2\theta) \cdot \Delta(2\theta)}{\Sigma I(2\theta) \cdot \Delta(2\theta)} \quad . \quad (5\text{-}4)$$

where $I(2\theta)$ is peak intensity at some angle 2θ and $\Delta 2\theta$ is the angular increment. The high Mg calcite peak was sufficiently symmetrical so that its centroid coincided with the angle of maximum amplitude, 28.82° ± 0.01° 2θ. The angular separation, Δ, was assumed constant at 0.37°. For the high Mg calcite peak, therefore, the integrated intensity is simply:

$$\int_{-\infty}^{\infty} A \exp\left[-B^2 (2\theta - \omega)^2\right] d(2\theta) = \sqrt{\pi}\,\frac{A}{B} \qquad (5\text{-}5)$$

Similarly, the intensity of the low Mg calcite peak is $\sqrt{\pi}\,\frac{C}{D}$.

A calibration curve, relating weight % high Mg calcite to its fractional X-ray diffraction peak intensity, was constructed using samples of known high and low Mg calcite concentrations. The standard samples were prepared using XRU-3 core samples from 3 m (all high Mg calcite) and 58 m (all low Mg calcite) depths mixed in weight proportions of 1:9, 3:7, 5:5, 7:3 and 9:1; using this proportion and the weight % aragonite in each sample, the weight % $MgCO_3$ was determined. X-ray diffractometer spectra of these standard samples were then treated as described in the preceding paragraph and intensities of the high and low Mg calcite components were obtained. Gaussian curve fit parameters are listed in Table 5-2. The intensity of the high Mg calcite peak relative to the sum of high and low Mg calcite peak intensities is plotted against the known weight % of high Mg calcite in Fig. 5-6. Due to the extremely low intensity of the high Mg calcite peak in the 1:9 standard sample, a satisfactory fit to the data could not be obtained. At values of 25 weight % high Mg calcite and greater, the data lie on a straight line with a slope of 1/86.

A theoretical intensity-concentration curve was also constructed, based on the procedure described in Chapter 7 of Klug and Alexander (1974). For the pure component 1,

$$(I_1)_o = \frac{K_1}{\rho_1 \mu_1^*} \qquad (5\text{-}6)$$

where $(I_1)_o$, ρ_1, and μ_1^* are the X-ray diffraction peak intensity, density, and mass absorption coefficient, respectively, of pure component 1. K_1 is a parameter dependent on the nature of the component

Table 5-2

X-RAY PEAK GAUSSIAN FIT PARAMETERS

	Sample	A	B	C	D (1)	$\frac{I_{High}}{I_{High}+I_{Low}}$ (2)	Weight % High Mg calcite (3)
Calibration Samples	(High/Low Mg Calcite; weight %)						
	25/75	1.47±0.12	3.37±0.18	7.55±0.06	2.92±0.09	0.14±0.03	
	44/56	3.67±0.10	2.57±0.15	7.65±0.09	3.16±0.11	0.37±0.03	
	65/35	4.81±0.10	2.46±0.11	3.91±0.09	3.30±0.14	0.62±0.03	
	88/12	6.20±0.10	2.55±0.15	1.58±0.20	4.25±0.21	0.87±0.03	
XC-1 Samples	(Depth; m)						
	11.1	3.95±0.35	2.51±0.55	0.48±0.22	1.67±0.61	0.85±0.11	87±10
	11.8	6.31±0.18	2.44±0.23	2.75±0.20	3.65±0.31	0.77±0.05	80±4
	12.2	4.44±0.05	2.97±0.13	1.78±0.06	2.99±0.12	0.72±0.02	75±2
	13.6±0.9	4.82±0.13	2.73±0.22	5.86±0.15	3.29±0.27	0.50±0.05	57±4
XC-2 Samples	(Depth; m)						
	15.2±0.9	6.73±0.38	2.26±0.49	1.65±0.44	5.34±1.73	0.91±0.07	93±7
	17.2±0.5	4.72±0.27	2.00±0.34	5.48±0.17	3.71±0.44	0.62±0.08	68±7

(1)
Parameters A, B, C and D are related (but not numerically equal) to high Mg calcite peak height, width, low Mg calcite peak height and width, respectively. Gaussian fit model discussed in text.

(2)
Integrated peak intensities of (high Mg calcite)/(high Mg calcite + low Mg calcite).

(3)
Obtained comparing calculated intensity ratios with calibration curve.

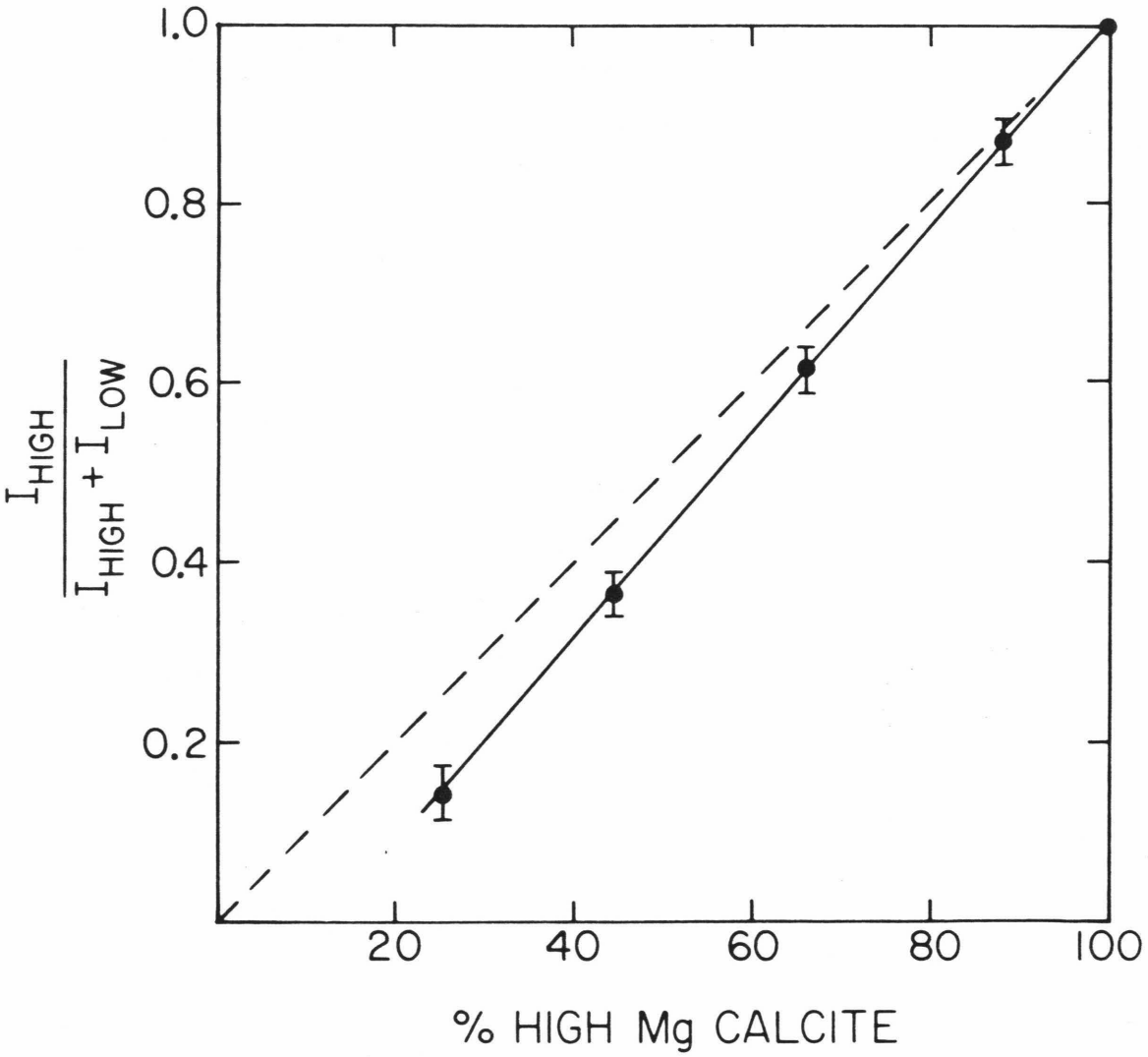

Figure 5-6. Empirical and theoretical calibration curves (solid dashed lines, respectively) relating measured intensity ratios and known $MgCO_3$ concentrations in calcite.

and instrumental arrangements. In a two component mixture containing a weight fraction x_1 of the first component, the X-ray peak intensity of this component is:

$$I_1 = (I_1)_o \frac{x_1 \mu_1^*}{x_1(\mu_1^* - \mu_2^*) + \mu_2^*} \qquad (5\text{-}7)$$

μ_2^* is the mass absorption coefficient of the second component. Combining (5-6) and(5-8) with an analagous set of equations for component 2 results in an expression for the peak intensity ratio of components 1 and 2:

$$\frac{I_1}{I_2} = \frac{x_1 \rho_2[x_2(\mu_2^*-\mu_1^*) + \mu_1^*]}{\rho_1 x_2[x_1(\mu_1^*-\mu_2^*) + \mu_2^*]} \qquad (5\text{-}8)$$

For the high and low Mg calcite analysis, it has been assumed that $K_1 = K_2$; this assumption appears justified by the close similarities in the chemical and structural nature of the two components, and by the identical sample preparation methods and instrumental arrangements used for both components. Using theoretical densities of 3.01 g/cc for $MgCO_3$ and 2.71 g/cc for $CaCO_3$, densities of the high (14.15 ± 0.35 weight % $MgCO_3$) and low (2.3 ± 0.8 weight % $MgCO_3$) Mg calcite components are calculated to be 2.75 g/cc and 2.72 g/cc, respectively. The mass absorption coefficients for CuKα radiation, calculated from the International Tables for X-ray Crystallography (1972), are 63.49 cm^2/g for high Mg calcite and 69.73 cm^2/g for low Mg calcite. From these values and Eq.(5-8), a theoretical curve between the fractional intensity of the high Mg calcite peak and its concentration can be determined; this is shown as the dashed line in Fig. 5-6. Note that the theoretical curve has a slope of 1/100 and passes through the origin.

The most plausible explanation for the discrepancy between the

theoretically and empirically determined calibration curves involves the nature of the components. As described earlier, the high to low Mg calcite transition is a microdissolution process in which textural features of the original high Mg calcite crystal are retained. However, changes in the crystals certainly must occur, and it cannot be strictly stated that the mechanism is totally non-destructive (Land, 1967). These variations in the microstructures of high and low Mg calcites may contribute to the deviation of the empirically derived from the theoretically calculated calibration curve. The direction of this deviation suggests a microcrystalline (i.e. less effective diffracting capacity) character for the high Mg calcite. Also, the low Mg calcite samples may consist of several populations of calcite crystals. In addition to stabilized products of high Mg calcite, samples from deeper levels probably contain calcite cement formed during marine or meteoric phreatic diagenesis (Land, 1970). The inorganically precipitated calcite will certainly be structurally distinct from that of organic origin, and may contribute to the deviation between the two curves in Fig. 5-6.

Whatever the characteristic of the high Mg calcite responsible for the discrepancy between the two curves, it is observed to be a feature of the high Mg calcite in samples from cores XRU-2 and 5, and hence inferred to be a feature of all the high Mg calcite on Runit. Calibration of XC-1 and XC-2 samples containing both high and low Mg calcite should, therefore, use the empirically determined curve.

X-ray powder diffraction spectra of XC-1 and XC-2 samples containing both high and low Mg calcite were analyzed according to the

method described in the first paragraph of this section. (See Table 5-2 for Gaussian fit curve parameters.) Computer drawn observed and calculated fit calcite peaks for four of the XC-1 samples are shown in Fig. 5-7. High Mg calcite concentrations were determined from integrated peak intensity ratios and the experimental curve in Fig. 5-6. In Fig. 5-8, these concentrations are plotted against depth of sample for both XC-1 and XC-2 core material. Two noteworthy features are evident in this graph: first, the progressive nature of the two curves, and consequently, of the high to low Mg calcite transition in the XC-1 and XC-2 cores, and, second, the 4 to 5 m downward displacement of the XC-2 transition curve from that of XC-1. The significance of these two features will be discussed in the next section.

Discussion of Cactus Crater Structure

The role of the Cactus cratering event in explaining the observations presented above, and how these observations, together with other geologic and geophysical data can provide a basis for understanding crater formation, are discussed below.

An initial word of caution concerning sample depth levels is warranted. Due to coring difficulties, sample recovery in the Cactus cores, XC-1 and XC-2, was poor, and there is a 1.5 meter uncertainty in the location of these samples; this uncertainty is superimposed upon the depth level error limits indicated in Fig. 5-8. The arguments, and resultant conclusions, presented below are not essentially altered by this additional uncertainty, however, quantitative values require critical assessment.

In order to evaluate possible cratering induced geologic changes,

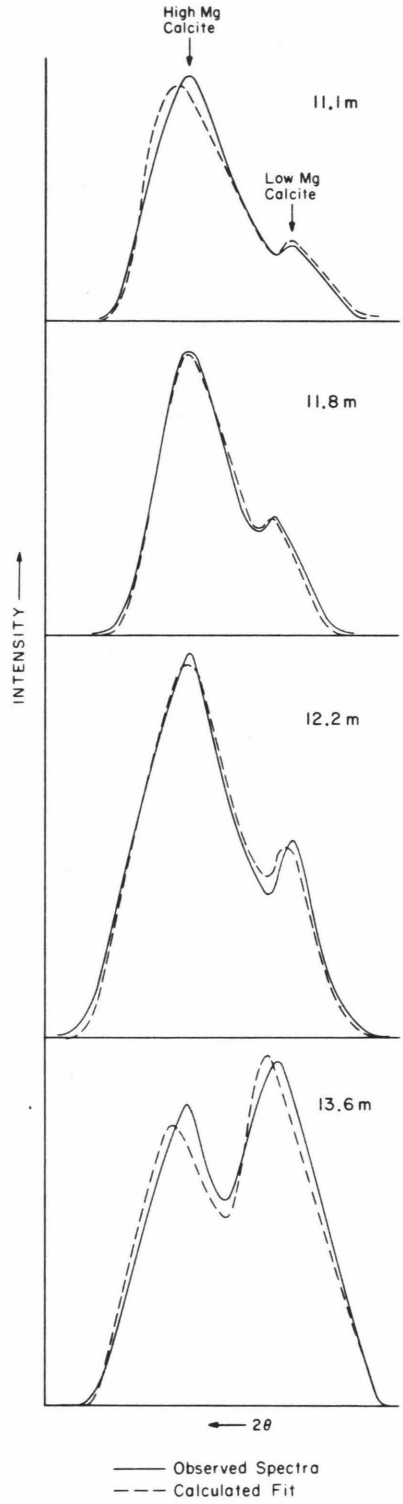

Figure 5-7. Observed and calculated X-ray diffraction peaks of high and low Mg calcite. Method used in calculating curve fits is described in the text.

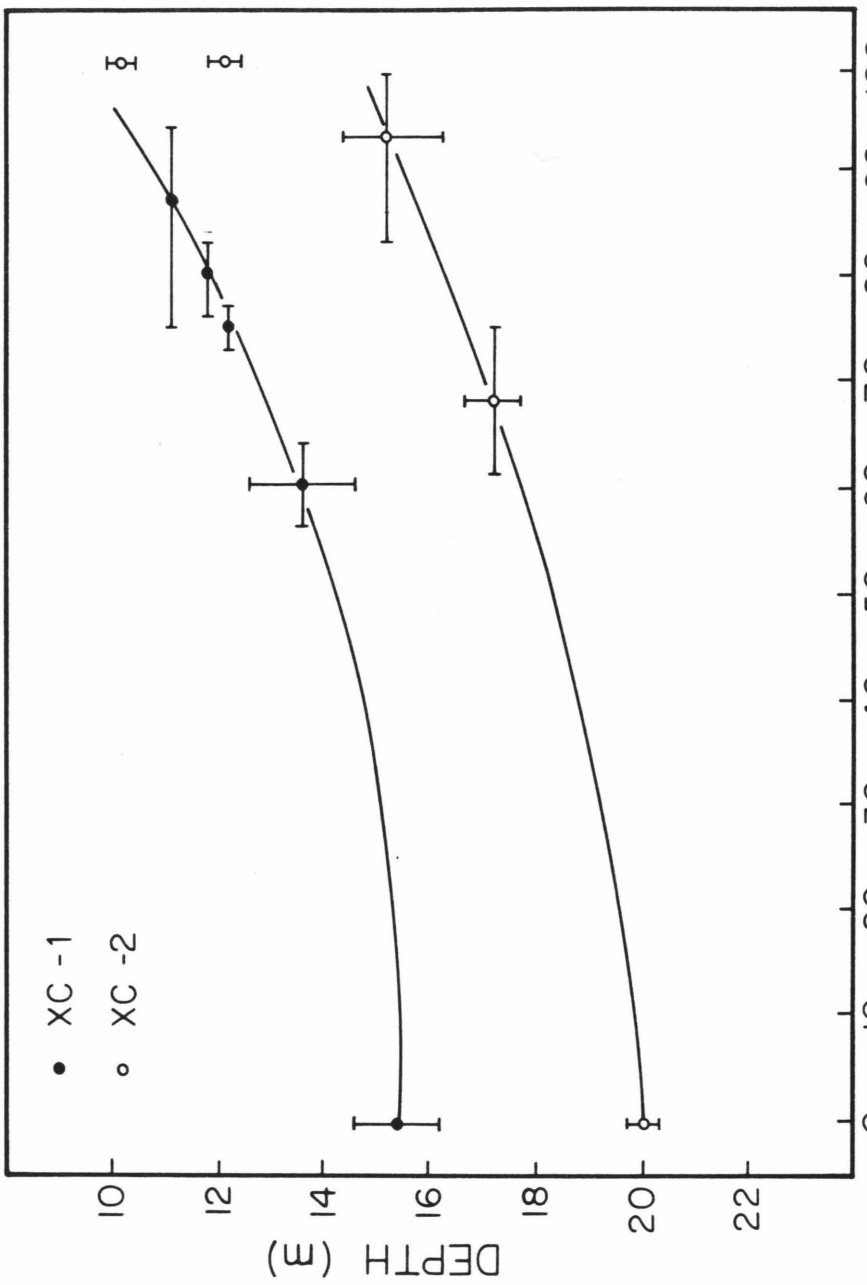

Figure 5-8. Weight % high Mg calcite, as determined from powder X-ray diffraction spectra, vs. depth in the core. XC-1 and XC-2 samples are indicated by solid and open circles, respectively. Note the smooth variation in both cores of composition with depth and the 4 to 5 m displacement of the XC-2 from the XC-1 curve.

it is first necessary to establish what the undisturbed situation was. Specifically, information on the nature and positional variation of the high to low Mg calcite transition boundary is needed. As discussed in previous sections, the high to low Mg calcite transition is observed as an abrupt boundary in the XRU cores and occurs at depths between 11 and 14 m (see Table 5-1). Considering the role of meteoric vadose diagenesis in this transition, it is reasonable to expect a correlation between the hydrologic regime present and transition depth. During periods in which the coral atoll is subaerially exposed, a meteoric fresh water lens develops within what is now a solid carbonate island. Rocks exposed to similar hydrologic, and therefore, diagenetic, conditions would lie circumferential to the island outline. It is thus anticipated that the depth to the high to low Mg calcite transition would vary along radial island transects, but remain fairly constant along any parameter, i.e. circumparallel to the reef crest. This situation may be illustrated on Engebi (Fig. 5-9), another windward island of Eniwetok Atoll (Couch, et al., 1975). Although the magnesian calcite transition on this island has not been investigated, depths to the first solution unconformity (with which the calcite transition correlates) are known. As depicted in Fig. 5-9, these depths are clearly observed to decrease moving approximately radially inward toward the center of the lagoon. It also appears that these depths or isochores approximately parallel to the reef crest.

The Runit Island cores XRU-1, 4 and 3 were drilled in a line approximately parallel to both the elongated island outline and the reef crest. According to the arguments just presented, depths to the

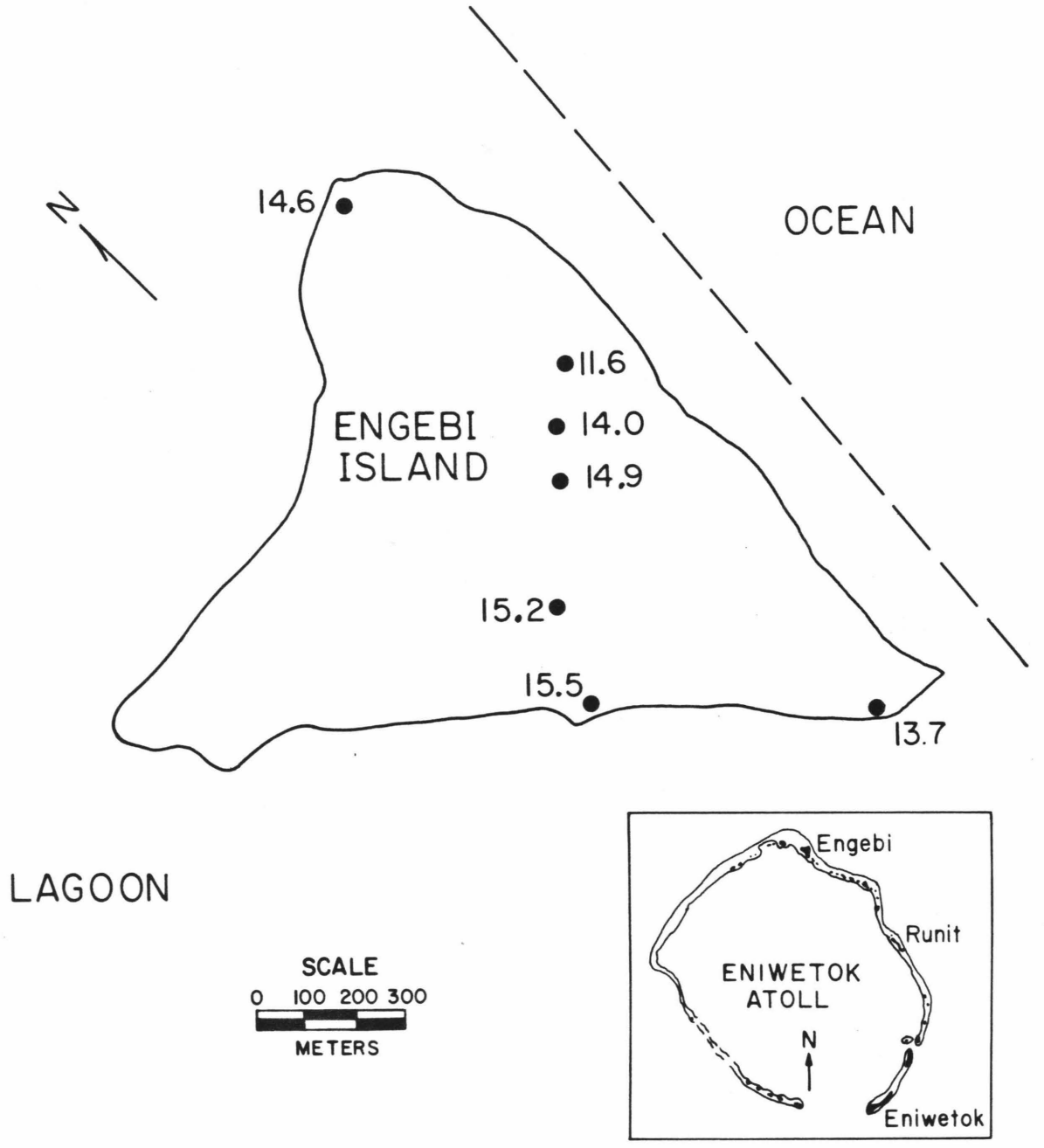

Figure 5-9. Map of Engebi Island, Eniwetok Atoll, showing depths, in meters, to first solution unconformity as observed in drillcore samples. Dashed line is approximately parallel to reef crest. (Adapted from Couch et al., 1975.)

high to low Mg calcite transition should be similar in these three cores. As noted in Table 5-1, however, the transition level in XRU-1 is depressed 1 to 3 m relative to that in XRU-3; a similar displacement is noted for XRU-4. These relations are illustrated in Fig. 5-10, a cross-section of Cactus Crater constructed from XRU and XC core data. The proximity of cores XRU-1 and 4 to Cactus Crater suggests cratering induced depression at these drill locations. Since the nature of the Mg calcite transition drastically changes directly beneath the crater, it is impossible to trace a sharp diagenetic transition into this area, and determining whether or not downward displacement is present here becomes difficult. Pressure attenuation considerations (Vizgirda and Ahrens, 1980), however, are consistent with stratigraphic depression occurring beneath the crater. According to results of this study, shock metamorphic levels in calcite from XC-1 require 4 to 5 m of downward displacement in order to accommodate theoretically reasonable pressure decay rates of d (depth)$^{-2}$ to d^{-3} (see e.g. Cherry and Peterson, 1970). In addition, deeper solution unconformities described in Couch et al., 1975 (i.e. older than the first solution unconformity correlative with the Mg calcite transition) are observed to be depressed beneath the crater (see Fig. 5-10). Since no core samples below 2.5 m were obtained from locations to the north-west of the crater (i.e., in line with XRU-1 and XRU-3 but on the opposite side of the crater), the behavior of the solution unconformities across the crater cannot be determined. Nevertheless, available evidence from stratigraphic and pressure decay considerations suggest cratering induced depression beneath Cactus.

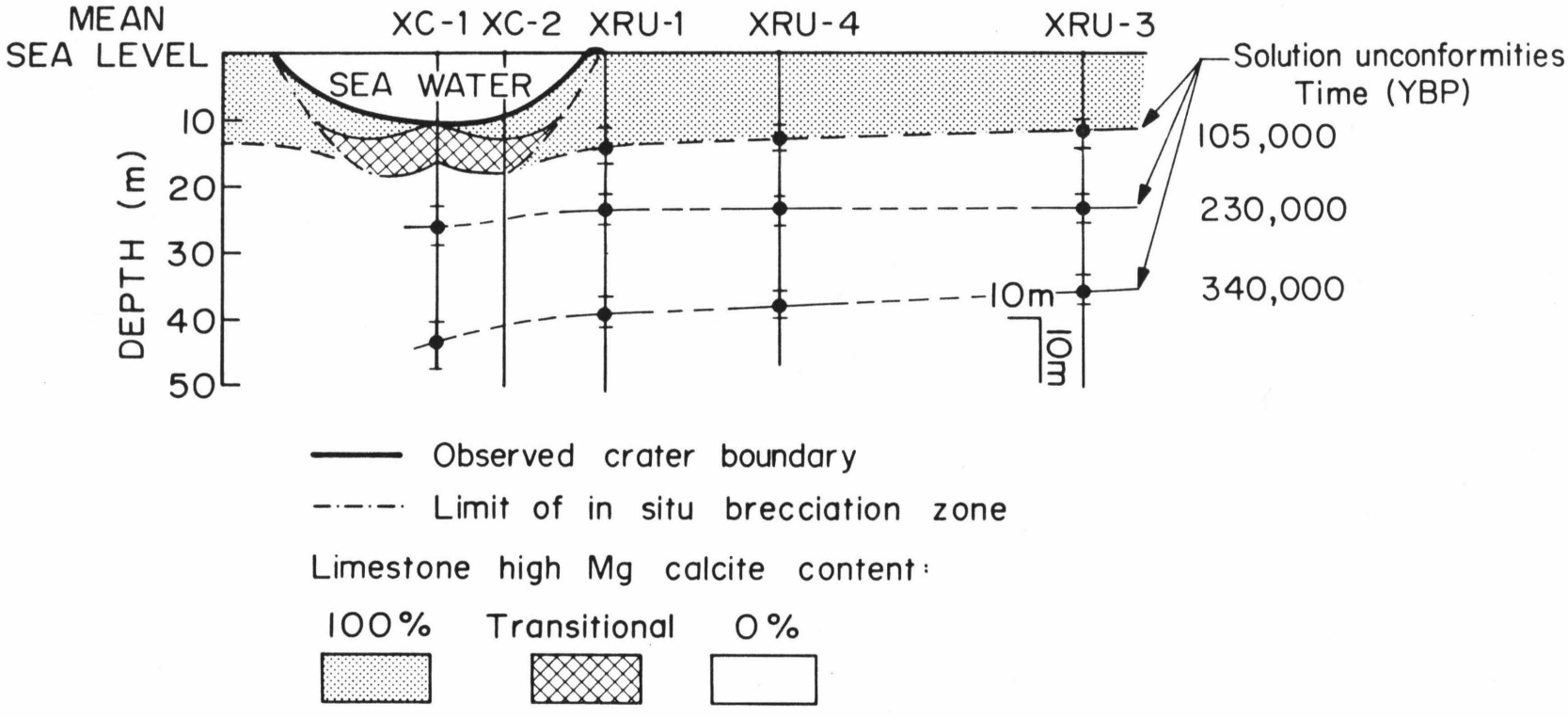

Figure 5-10. Cross-section through Cactus Crater constructed on the basis of the high and low Mg calcite data. Note the apparent depression of the high to low Mg calcite transition boundary toward the cratered area and the inferred central peak inside the crater. (Two-fold vertical exaggeration.)

As discussed in previous sections, the nature of the high to low Mg calcite transition observed in samples from cores drilled inside Cactus Crater contrasts drastically with that observed in cores drilled outside the crater. The gradual change from all high to all low Mg calcite, displayed by XC-1 and 2 core samples, is not found anywhere else on Runit Island, nor is it expected considering the conditions under which the diagenesis occurs. Characteristics of this feature, unambiguously resulting from the cratering event, lead to several conclusions regarding the mechanics of crater formation.

First of all, the fact that the transition occurs gradually and in a consistent manner (see Figs. 5-4, 5-5 and 5-8), indicates that the material in this transitional interval was never ejected from the cavity, since ejection is expected to result in a homogeneous fallback breccia. If a fallback breccia lens exists, it is limited, at the center of the crater, i.e. at the XC-1 drill site, to a thickness of 1 m or less. This is the difference between the depths at which the hole was collared in and the first sample was retrieved. Instead, most of the material excavated during the cratering event experienced in-situ brecciation and mixing. Mixing was probably initiated by material travelling radially downward and outward at particle velocities imparted after passage of the explosion-induced shock front. After brecciation of the originally saturated but competent coralline limestone, at least partial fluidization likely occurred, creating an inviscid, readily mixed substance. The turbulence of mixing was sufficient to completely homogenize hand specimen size samples.

The observed pattern of the transitional Mg calcite layer also

aids in the definition of the "excavation cavity". If the extrapolated "mixing lines" in Fig. 5-8 are valid, then material experienced some degree of excavation, though not ejection, down to depths of approximately 15 to 20 m in XC-1 and XC-2 drill-core locations, respectively. Brecciation and mixing may have occurred at deeper levels within a totally low Mg calcite lithology, however, our methods would not allow its detection. The depths noted in previous sentences are, therefore, used to define the minimum limit of in situ brecciation sketched in Fig. 5-10.

Finally, the form of the transitional Mg calcite layer, as shown in Fig. 5-10, suggests a fundamental reclassification of Cactus Crater, which, up to the present, has been considered as belonging to the class of simple craters. As depicted in this cross-section, the transitional Mg calcite layer is 4 m thick in both cores and is depressed 4 to 5 m in XC-2 relative to that in XC-1. Both these observations are inconsistent with the structure of simple crater. Rather, the observation that the transitional layer occurs at shallower depths in the center of the crater than at a distance of one-half crater radius outward from the center is compatible with the interpretation of Cactus as a complex crater with a central uplift (Dence, et al., 1977). Two other possibilities must first be investigated before any firm conclusions concerning crater structure can be drawn. As mentioned in the beginning of this section, sample depth levels in the Cactus Crater cores are not precisely known. Nevertheless, the margin of error is insufficient to alter the conclusion regarding the existence of a central uplift; its extent, however, may be under or overestimated by up to 3 m. A second situation

that may produce the observed pattern is the presence of some inhomogeneity in the cratered vicinity. In this case, the depiction of the Cactus floor as symmetrical would be inaccurate, and the structural classification ambiguous. Inhomogeneities do exist in Runit Island. For example, Ristvet et al., (1978) describe a cable berm structure located south of borehole XC-1. Lacking good geologic controls, in particular borehole evidence in the western portion of the island, this second possibility cannot be conclusively eliminated. However, as we shall see in the next section, the observation of a complex morphology in a small crater would not be an isolated case.

Seismic investigations conducted on Runit Island during Project EXPOE (Ristvet, et al., 1978) are limited to an approximately 550 m long seismic refraction profile obtained along the northeastern ocean margin (see Fig. 5-1 for location). Four seismic layers are distinguished in the upper 60 m of Runit. Apparent seismic velocities of these layers consistently vary from 0.4 km/sec to 3.1 km/sec with increasing depth, reflecting greater degrees of cementation. The shallowest layer represents unconsolidated supratidal sediments and is of uniform thickness along the extent of the seismic profile. The second layer, consisting of weakly to uncemented carbonate sediments appears to thicken toward Cactus, and the interface between this and the third layer of moderately cemented carbonate rock appears to be depressed 3 m in the proximity of the crater. As mentioned earlier, and as depicted in Fig. 5-10, 2 solution unconformities, occurring between 20 and 50 m depth, appear to be depressed beneath Cactus Crater, the extent of downward displacement is 6 m and 4 m for the first and second of these unconformities, respectively. On the

basis of this, and the seismic evidence, Ristvet et al. (1978) also suggest that depression did occur beneath Cactus Crater. A recently completed seismic survey of the crater (B. Ristvet, personal communication, 1980) may provide additional support for this conclusion.

Seismic velocities determined in the refraction profile may be used to further investigate the phenomenon of cratering induced brecciation. The velocities recorded for the second layer, i.e. the layer of unconsolidated to weakly cemented carbonate sediments, are observed to decrease consistently from 2.4 km/sec to 2.0 km/sec as one approaches the cratered area. Since this large a variation is not expected in a line parallel to the reef margin, we infer that this velocity decrease results from shock-induced brecciation beneath the crater. The depth of this lower velocity layer at the end of the refraction line closest to the crater is about 20 m below mean sea level. This depth is consistent with the observed maximum excavation limit of 20 m below Cactus Crater. On the basis of the high to low Mg calcite transition evidence from cores XRU-1 and XRU-4, where the transition was observed as a sharp diagenetic break, the disturbance causing decreased velocities involves fracturing, but no mixing.

Paleontological evidence (Ristvet et al., 1978) supports speculations involving brecciation and mixing beneath the crater and the extent of the excavation cavity. Pink, unbleached shells of the encrusting foraminifera, Homotrema rubrum, indicating an origin above the first unconformity, are observed down to depths of 16 ± 1.5 m beneath the floor of Cactus Crater. Outside Cactus, unbleached shells are found only above the first solution unconformity, correlative with the Mg calcite

transition depths, listed in Table 5-1. This fossil evidence is unclear in that it is not noted whether bleached and unbleached foraminifera shells are observed together at any level above 16 m beneath the crater. Such an observation would be analogous to the coexistence of both high and low Mg calcite in Cactus Crater cores. Nevertheless, the Homotrema rubrum evidence supports mixing occurring to depths of 16 ± 1.5 m beneath Cactus, and the delineation of a minimum excavation cavity based on the Mg calcite data.

Gamma logs were obtained for most of the EXPOE boreholes (Ristvet et al., 1978). Not unexpectedly, high radiation levels were recorded at several depths in boreholes XC-1 and XC-2; these patterns are reproduced in Fig. 5-11. Note the two high intensity peaks observed in both boreholes. As an accuracy check on the gamma log, radiation levels (primarily due to ^{60}Co, ^{102}Rh, ^{125}Sb and ^{155}Eu) of 24 split spoon samples were measured at the McClellan Central Laboratory, McClellan Air Force Base; these data are also presented in Fig. 5-11. These laboratory measurements corroborate both peaks observed in gamma logs of XC-1, and the shallower peak of XC-2. Lack of samples from 18 to 20 m depths of XC-2 may explain why the second high intensity radiation peak was not observed. Depths of the three laboratory observed high intensity peaks are consistently 2 m deeper than the well log data.

The observed distribution of gamma radiation serves to further elucidate the cratering process. Because peak penetration depths of nuclear fission products and neutrons are on the order of 10μ and 1 m, respectively (see e.g. Fleischer et al., 1975; Burnett and Woolum, 1974), peak radiation levels are produced only in substrate materials in close

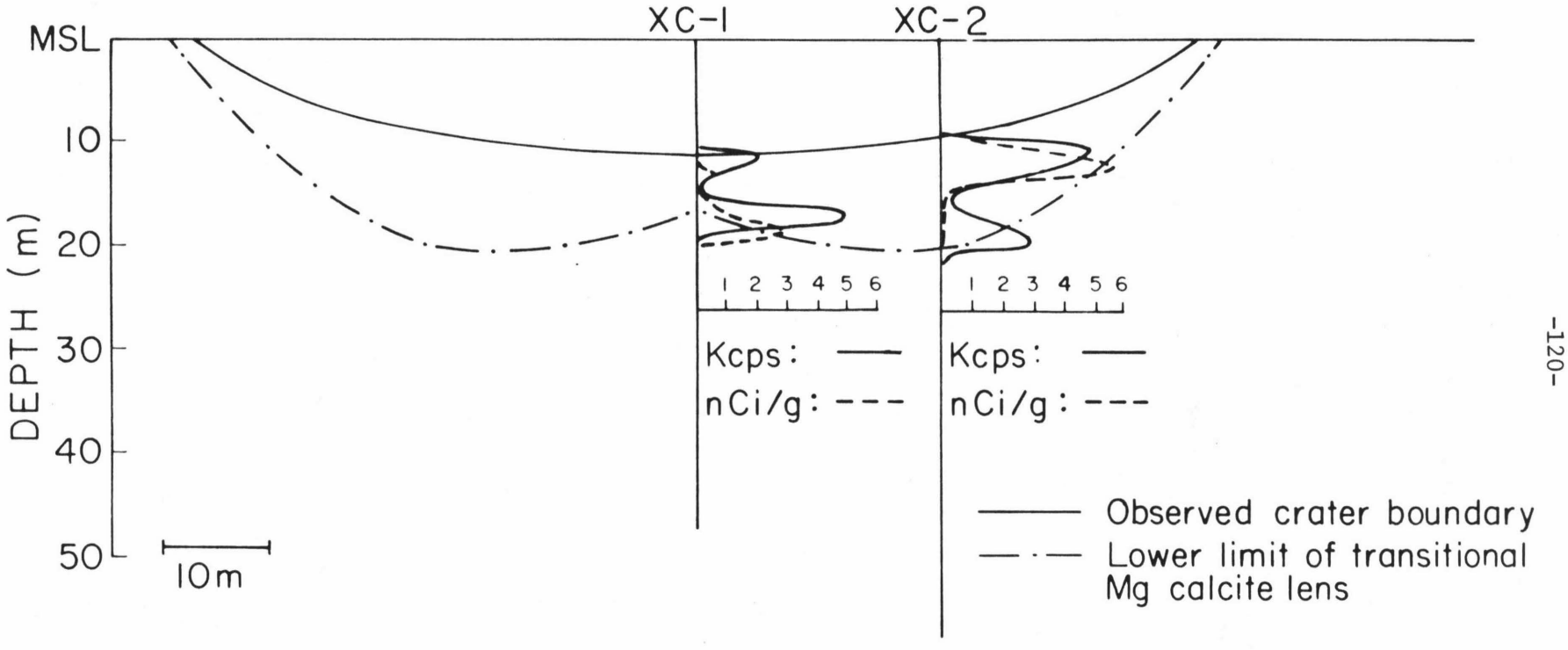

Figure 5-11. Cactus Crater cross-section (no vertical exaggeration) showing gamma (γ) well log data (solid line) and laboratory measured total gamma activity (dashed line) for XC-1 and XC-2 cores; units for these two data sets are in kilocounts per second and nanocuries per gram, respectively. Figure is compiled from data presented in Ristvet et al., 1978.

proximity (within 1 m) to the nuclear device. The observed post-event radiation intensity pattern, therefore, is a result of cratering produced particle motions. The observed radiation pattern in Cactus Crater may be the result of the following sequence of events. Material exhibiting the highest measured radiation levels originated closest to the nuclear device. As the shock wave from the explosion propagated into the target, high particle velocities were induced in the same material subject to severe radionuclide contamination. Some of this material travelled radially into the target and formed a lining to the excavation cavity. Other particles, engulfed by the rarefaction wave produced upon reflection of the shock wave from the free surface of the target, were ejected at high velocities from the forming crater cavity. Some of these particles fell back into the cavity and constitute a thin fallback breccia lens. It is proposed that the shallow and deep high radiation intensity peaks represent the fallback and high velocity injected material, respectively. This interpretation is consistent with the crater formation model derived on the basis of the Mg calcite transition data. In addition, the crater excavation limits based on the gamma well log evidence (16 m and 19 m for XC-1 and XC-2 cores, respectively) agree well with those determined from the same Mg calcite transition.

The various avenues of information discussed above offer regrettably little support for, or contention with, the Mg calcite transition based speculations concerning a central peak morphology for Cactus Crater. A logical source of corroborative evidence is crater profile data. Lead line profiling techniques were used in the post-shot crater survey conducted almost 4 months after the event. These results, together with

those of the pre-shot profile, were used in the construction of the difference contour map shown in Fig. 5-1. A complex crater morphology is not obvious from this map. However, it is improbable that the immediate post crater structure would be retained unaltered in a water-saturated environment, particularly after four months of exposure to open ocean circulation. Note, however, that the deepest point in the crater is located at an off-center location, equidistant with XC-2 from the crater center, directly opposite from the breached portion of the island. Since this is the portion of Cactus farthest from and, therefore, least susceptible to sediment inwashing from the open ocean, it has the greatest probability of retaining the original crater bottom topography. Perhaps the observation of maximum water depth here is a remnant of a topographic low encircling a central peak in the original crater bottom profile. No complex crater bottom profiles were recorded for any of the other shallow "flat-floored" Pacific Proving Ground nuclear craters (Ristvet et al., 1978). However, these profiles were all obtained months to years following the crater forming events, allowing sufficient time to completely alter the crater bottom topography. Support for a complex crater morphology for Cactus can best be obtained from comparisons with other explosion and laboratory scale craters, discussed in the following section.

Comparisons with Other Craters and Conclusions

In an attempt to gain a broader perspective of Cactus Crater in relation to other impact and explosion craters, the best comparison (in terms of size and substrate similarities) to be made is between Cactus and Snowball craters. The latter is an experimental explosion crater,

formed at the Defense Research Establishment, Suffield (Alberta) site by the detonation of 500 tons of TNT in saturated, unconsolidated clays, silts and silty sands (Roddy, 1976). Snowball has a diameter of 107 m and a maximum depth of 9 m compared to respective dimensions of 105 m and 10.7 m for Cactus Crater. As in Cactus, water infilling occurred after the crater formed. A thin breccia lens (1 to 2 m) is observed at Snowball, corresponding to that speculated for Cactus. Major differences between the Cactus and Snowball sites are in the strength properties of the media, one being a basically competent but saturated coral rock, the other, saturated and completely unconsolidated sediments. There is a small difference in the heights of burst (HOB) of the two explosions; the 500 ton TNT hemisphere producing Snowball was detonated at ground level, i.e. zero HOB, whereas the 18 kTon TNT
equivalent Cactus device had an approximately 1 m HOB. A distinct central peak structure, with an uplift of 8.5 m, is evident at Snowball. Although intensely folded, the clay and silt beds in this central mound retain sufficient integrity and can be mapped. Cactus, as speculated, also has a central peak, with 4 to 5 m of uplift. The rock making up this central structure, however, appears to be intensely shattered and mixed, and, had visually distinguishable units been present, they could probably not be mapped. Thus, significant differences exist in the size and nature of the two central peaks. Furthermore, differences in the mode of disruption are observed away from the central peak. Numbered markers used in the Snowball experiment, allowing resolution of mass movements during cratering, indicate two discrete sets of motions occurred beneath the crater floor: the top layer moved radially outward, while

material below it moved toward the center and up to form the central peak. Samples from the XC-2 Cactus core suggest turbulent brecciation and mixing compared to the (relatively) ordered movements beneath Snowball. It appears, therefore, that following shock-induced brecciation, the coral rock becomes less coherent than the silt and clay sediments. Differences in shock compression properties, or in the amount or distribution of water in the two types of substrates, may be responsible for the varying behavior. Despite these differences, the two craters are similar in many respects, the most important being target saturation, and the analogy of Snowball to Cactus serves as an important feasibility argument for the description of Cactus as a complex crater.

Applying the Bingham plastic model of Melosh (1981) gives some indication of the material strength of the shocked coral material. According to this model, a minimum value of 5 for the dimensionless strength parameter, $\rho gH/c$, is required before crater collapse can occur; central peak formation requires a larger value, but the limiting case is considered here. Using a water-saturated coral density, ρ, of 2.4 g/cc (from measured bulk ρ) and a transient crater depth, H, of 20 m, a maximum Bingham yield stress of 1 bar is calculated (g is the acceleration of gravity). Interestingly, yield stresses of the same order of magnitude have been measured for a variety of water-saturated clays, comparable to those at the Snowball Crater site (Wilson, 1927). There is potential then, according to this model, for quantitative treatment of crater structure target dependence.

Although information on terrestrial meteorite craters is often incomplete (or nonexistent), some comparisons between these craters and

Cactus can be drawn. Where depth to the bottom of the breccia lens can be ascertained, the depth-to-diameter ratio of simple terrestrial craters is 1:3 (Dence et al., 1977). Determining both the extent of the breccia lens and the rim position of the excavated cavity is particularly difficult for complex structures, and the depth-to-diameter ratio of these craters is speculative. A palinspastic reconstruction of the Sierra Madera and Gosses Bluff structures suggests a ratio of 1:4 or 1:5 (Dence, 1977). Using geologic observations and geophysical subsurface data, Pohl et al. (1977) speculate that the transient cavity of the Ries Crater had a similar depth to diameter ratio. The apparent 1:5 ratio for the true cavity of Cactus, therefore, is more compatible with that of complex structures.

Downward displacement has not actually been observed beneath any simple craters (Dence, 1977), even those which offer sufficient stratigraphic control, such as Meteor Crater (Shoemaker, 1963). On the basis of attenuation rate arguments, however, Robertson and Grieve (1977) speculate that depression and approximately 50% shortening of the rock section beneath the crater occurred at Brent, a simple crater in crystalline rock. In complex craters, rocks in the ring surrounding the central peak typically appear to have undergone downward and inward motions. At the Red Wing Creek buried structure, there is some evidence for depression, which eventually dies out at greater depth, of rocks beneath the central peak (Brenan et al., 1975). Stratigraphic depression beneath simple experimental impact craters has been clearly demonstrated by Gault et al. (1968), among others. In a laboratory scale study of explosive craters, Piekutowski (1977) observed downward displacement

beneath a crater, formed in loose saturated sand, with a distinct central uplift. These laboratory studies, particularly those of Piekutowski which utilized saturated target materials, lend significant support to the speculated depression (of the ringed area surrounding the central peak) beneath Cactus.

In Vizgirda and Ahrens (1980), an attenuation rate of $(\text{depth})^{-5.7}$ is calculated for Cactus on the basis of ESR detected shock metamorphism (see Chapter 3); this rate is calculated in terms of post-flow stratigraphic coordinates. According to model calculations, downward displacement of 4 to 5 m is consistent with attenuation rates of d^{-2} to d^{-3}. These rates are compatible with those inferred for simple craters. Displacements of approximately 3 m are compatible with $d^{-4.5}$ decay rates speculated for complex structures (Robertson and Grieve, 1977). Although, considering the uncertainty in the estimate of displacement beneath Cactus, and the speculative nature of model attenuation rates, firm conclusions about either cannot be drawn, the interesting fact remains, that estimated amounts of displacement are consistent with reasonable attenuation rates.

The observation of a thin (1 m or less) fallback breccia lens at Cactus is in agreement with general observations. Thin fallback breccia lenses, relative to the extent of autochthonous breccia, have been observed in both simple and complex structures, such as Meteor Crater (Shoemaker, 1963) and Gosses Bluff (Milton et al., 1972).

The γ ray intensity logs, discussed in the previous section, revealed two high intensity peaks, one located near the crater surface and the other at the hypothesized excavation cavity boundary. This pattern

is similar to the distribution of melts or of intensely shocked and pulverized rock in simple craters in crystalline and sedimentary rock. At Brent and Lonar Lake Craters, formed in granitic gneiss and basalt, respectively, melt rocks are concentrated in the top and basal portions of the excavated cavity (Dence, 1968; Fredriksson et al., 1973). At Meteor Crater, formed entirely in sedimentary rocks, meteorite fragments and highly shocked target rock are concentrated in similar positions (Shoemaker, 1963). These two layers of highly shocked material have not been clearly identified in complex craters. The extensive melt sheets described at complex craters, for example Manicouagan, are interpreted as the material lining the excavation cavity (Grieve and Floran, 1978). Melt layers are detected at two distinct intervals beneath the ring depression of Boltysh, a 20-25 km diameter structure in pre-Cambrian crystalline rock (Yurk et al., 1975); however, the lower "unit" of melt was detected at only 1 borehole location and extended for a mere 20 m. Its lateral extent, thus, remains ambiguous, and a melt distribution analogy between Boltysh and simple craters cannot be justified. Based on the γ log evidence, this same analogy between Cactus and simple craters is warranted.

Grieve et al. (1977), on the basis of impact melt distributions in simple and complex craters, proposed a common cratering model for both types of structures. Some of the interpretations stemming from Cactus Crater observations are consistent with that model. The inferred sequence of events and material motions during the Cactus excavation stage, for example, agree closely with that described by Grieve et al. (1977). There is no indication, however, that severe disruption of the breccia

lens occurred during the modification stage. Centripetal sliding (depicted in Fig. 5-12), a commonly invoked modification means for complex craters, produces an intensely disordered central peak. As evidenced in the orderly high to low Mg calcite transition in the XC-1 core, and its close similarity to the transition trend in XC-2, such disordering did not take place in the central uplift of Cactus Crater. This observation suggests that a rebound mechanism (Fig. 5-12), and not centripetal sliding, may have produced the Cactus central peak. The Melosh (1981) Bingham plastic model assumes a hydrodynamic rebound theory to explain various morphologic features of complex craters, such as central uplifts. A particularly persuasive argument for invoking rebound as the relevant modification mechanism is presented in a study of Martian complex craters by Pike (1980). Here, the sequence of morphologic features appearing with increased crater diameter is consistent with dynamic rebound acting to form central peaks, and in turn, initiating collapse phenomena such as rim failure. If rebound, and not sliding was, indeed, the active mechanism in the Cactus cratering event, then the observed crater diameter closely approximates that of the transient crater; the depth to diameter ratio of 1:5 would, thus, be inferred for the transient crater. The difference between this ratio and the 1:3 value commonly observed in simple craters suggests an essential difference in the transient crater geometry of simple and complex craters. This same suggestion has been proffered on the basis of terrestrial impact crater observations (see e.g. Pike, 1980) and experimental explosive crater investigations (Schmidt and Holsapple, 1981).

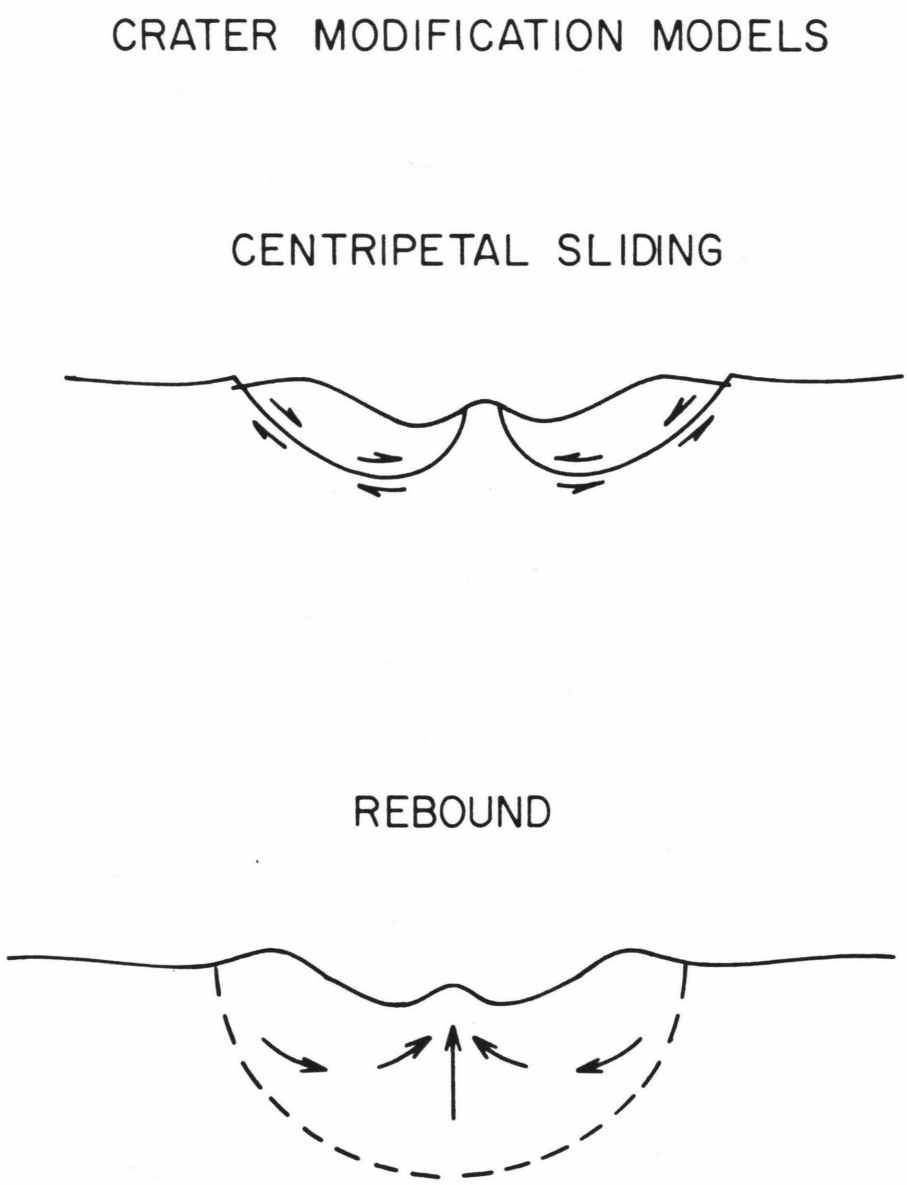

Figure 5-12. Sketches depicting two possible crater modification mechanisms. Dashed line in the rebound model represents limit of region "fluidized" during excavation process (after Melosh, 1981). Reasons for preference of this latter model in the case of Cactus Crater are discussed in the text.

Summary

Summarizing the key observations and interpretations, Cactus can be described as a 105 m diameter complex crater with 4 to 5 m of central uplift and possible downward displacement beneath the structure. Maximum depth of the excavation cavity is 20 m, and the resultant true crater depth to diameter ratio is 1:5. The majority of the breccia infilling the excavation cavity is of autochthonous origin and a fallback breccia lens, if it exists, is limited to a maximum thickness of 1 m. The excavation process, as deduced from Mg calcite and γ log data, involves both ejection of some of the highly shocked material and high velocity injection of the remainder to form a lining to the transient crater floor. This in situ brecciation and mixing is envisioned as a very turbulent mechanism, facilitated by the high velocities and low viscosities of the intensely shocked and, probably, fluidized carbonate rock. Such a sequence of events is consistent with the crater excavation model of Grieve et al. (1977), deduced on the basis of impact melt distribution in terrestrial, particularly simple, craters. Thus, observations at Cactus Crater (specifically, the two peaks in the γ log data, inferred to be analogous to the basal and upper melt layers in simple craters) serve to support a basic contention of the Grieve et al. model, that is, that a single excavation model can be applicable to both simple and complex craters. Cactus Crater modification, on the basis of the Mg calcite study, is inferred to involve a dynamic rebound mechanism rather than centripetal sliding. Using the Bingham plastic rebound model of Melosh (1981), a maximum yield stress of 1 bar is calculated for the shock-affected carbonate medium. Clays, such as those in which Snowball

(an explosion crater with many features similar to Cactus) was formed, have comparable yield stresses.

Some of the features observed at Cactus have counterparts in terrestrial impact craters and may have been produced by the same processes. Application of a cratering model based on Cactus to other impact and explosion structures, however, should proceed with caution, since the unique properties of a water-saturated carbonate target may influence cratering mechanisms as well as modulate transitions between basic morphologic categories. The detailed observations presented here will, hopefully, contribute to the quantitative evaluation of target properties on crater morphologies, and serve as useful guidelines in the formulation of theoretical cratering models.

References

Bøggild, O. B., The shell structure of the mollusks, Danske Vidensk. Selsk. Skr., 9, pt. II, p. 235-326, 1930.

Brenan, R. L., B. L. Peterson and H. J. Smith, The origin of Red Wing Creek structure: McKenzie County, North Dakota, Wyoming Geol. Assoc. Earth Sci. Bull., 8, 1-41, 1975.

Burnett, D. S. and D. S. Woolum, Lunar neutron capture as a tracer for regolith dynamics, Proc. 5th Lunar Conf., p. 2061-2074, 1974.

Chave, K. E., A solid solution between calcite and dolomite, J. Geology, 60, p. 190-192, 1952.

Chave, K. E., Aspects of the biogeochemistry of magnesium [pt] 1, Calcareous marine organisms, J. of Geology, 62, no. 3, p. 266-283, 1954.

Chave, K. E., Aspects of the biogeochemistry of magnesium [pt] 2, Calcareous sediments and rocks , J. of Geology, 62, no. 6, p. 587-599, 1954

Cherry, J. T. and F. L. Petersen, Numerical simulation of stress wave propagation from underground nuclear explosions, Peaceful Nuclear Explosions, Internat. Atomic Energy Agency, Vienna, p. 241-325, 1970.

Couch, R. F., J. Fetzer, E. Goter, B. Ristvet, E. Trember, D. Walter and V. Werdland, Drilling Operations in Eniwetok Atoll During Project EXPOE, Air Force Weapons Laboratory, Final Report, 1975.

Dence, M. R., Shock zoning at Canadian craters: petrography and structural implications, In Shock Metamorphism of Natural Materials, B. M. French and N. M. Short, eds., Mono Book Corp. (Baltimore), p. 169-184, 1968.

Dence, M. R., R.A.F. Grieve and P. B. Robertson, Terrestrial impact structures: principal characteristics and energy considerations, In Impact and Explosion Cratering, Roddy, D. J., Pepin, R. O. and Merrill, R. B. eds., Pergamon Press (N.Y.) p. 247-275, 1977.

Fleischer, R. L., P. B. Price and R. M. Walker, Nuclear Tracks in Solids: Principles and Applications, U. of California Press, Berkeley, 1975.

Fredriksson, K., A. Dube, D. J. Milton and M. S. Balasundaram, Lunar Lake, India: An impact crater in basalt, Science, 180, p. 862-864, 1973.

Gault, D. E., W. L. Quaide and V. R. Oberbeck, Impact cratering mechanics and structures, In Shock Metamorphism of Natural Materials, B. M. French and N. M. Short, eds., Mono Book Corp. (Baltimore) p. 87-99, 1968.

Goldsmith, J. R. D. L. Graf and O. I. Joensuu, The occurrence of magnesian calcites in nature, GCA 7, p. 212-230, 1955.

Grieve, R.A.F., M. R. Dence and P. B. Robertson, Cratering processes: as interpreted from the occurrence of impact melts, In Impact and Explosion Cratering, Roddy, D.J., Pepin R. O. and Merrill, R. B. eds., Pergamon Press (N.Y.) p. 791-814, 1977.

Grieve, R.A.F. and R. J. Floran, Manicouagan impact melt, Quebec Part 2, Chemical interrelations with basement and formational processes, J. Geophys. Res., 83, p. 2761-2771, 1978.

Harker, R. I. and O. F. Tuttle, Studies in the system CaO-MgO-CO_2, Part 1, The thermal dissociation of calcite, dolomite and magnesite, Am. J. of Science, 253, p. 209-224, 1955.

Howard, K. A., T. W. Offield, and H. G. Wilshire, Structure of Sierra Madera, Texas, as a guide to central peaks of lunar craters. GSA Bull. 83, p. 2795-2808, 1972.

Klug, H. P. and L. E. Alexander, X-Ray Diffraction Procedures for Polycrystalline and Amorphous Materials, John Wiley and Sons, Inc. (N.Y.) p. 531-544, 1974.

Land, L. S., Diagenesis of skeletal carbonates, J. of Sedimentary Petrology, 37, no. 3, p. 914-930, 1967.

Land, L. S., Phreatic versus vadose meteoric diagenesis of limestones: evidence from a fossil water table, Sedimentology, 14, p. 175-185, 1970.

MacGillavry, C. H. and G. D. Rieck, eds., International Tables for X-ray Crystallography, Vol. III, Kyroch Press, Birmingham, England p. 162-165, 1972.

Melosh, H. J., A schematic model of crater modification by gravity, preprint submitted to J. Geophys. Res., 1981.

Milton, D. J., B. C. Barlow, Robin Brett, A. R. Brown, A. Y. Glikson, E. A. Manwaring, F. J. Moss, E.C.E. Sedmik, J. Van Son, and G. A. Young, Gosses Bluff impact structure, Australia, Science 175, #4027, p. 1199-1207, 1972.

Neumann, A. C., Processes of Recent carbonate sedimentation in Harrington Sound, Bermuda, Bull. of Marine Science, 15, p. 987-1035, 1965.

Offield, T. W. and H. A. Pohn, Geology of the Decaturville impact structure, Missouri, U.S.G.S. Professional Paper 1042, 1979.

Piekutowski, A. J., Cratering mechanisms observed in laboratory in laboratory-scale high-explosive experiments, In Impact and Explosion Cratering, D. J. Roddy, R. O. Pepin and R. B. Merrill eds., Pergamon Press (N.Y.) p. 67-102, 1977.

Pike, Richard J., Formation of complex impact craters: evidence from Mars and other planets, Icarus 43, p. 1-19, 1980.

Pohl, J., D. Stöffler, H. Gall and K. Ernstson, The Ries impact crater, In Impact and Explosion Cratering, D. J. Roddy, R. O. Pepin and R. B. Merrill eds. Pergamon Press (N.Y.) p. 343-404, 1977.

Ristvet, B. L., R. F. Couch, J. D. Fetzer, E. R. Goter, E. L. Tremba, D. R. Walter and V. P. Wendland, A Quaternary diagenetic history of Eniwetok Atoll (abstract), Geol. Soc. of America Abstracts with Programs, 6, p. 928-929, 1974.

Ristvet, B. L., E. L. Tremba, R. F. Couch, J. A. Fetzer, E. R. Goter, D. R. Walter, and V. P. Wendland, Geologic and Geophysical Investigations of the Eniwetok Nuclear Craters. Air Force Weapons Laboratory, Final Report, 1978.

Robertson, P. B. and R.A.F. Grieve, Shock attenuation at terrestrial impact structures, In Impact and Explosion Cratering, D. J. Roddy R. O. Pepin and R. B. Merrill eds., Pergamon Press (N.Y.) p. 687-702, 1977.

Roddy, David J., High-explosive cratering analogs for bowl-shaped, central uplift, and multiring impact craters, Proc. Lunar Planet. Sci. Conf. 7th, p. 3027-3056, 1976.

Schmidt, R. M. and K. A. Holsapple, An experimental investigation of transient crater size (abstract). In Lunar and Planetary Science XII, p. 934-936, Lunar and Planetary Institute, Houston, 1981.

Shoemaker, E. M., Impact mechanics at Meteor Crater, Arizona, In The Moon, Meteorites and Comets, D. M. Middlehurst and G. P. Kuiper eds. Univ. of Chicago Press, p. 301-336, 1963.

Silliman, B., On the chemical composition of the calcareous corals, Am. Jour. Sci., v. 1 2nd ser., p. 189-199, 1846.

Vizgirda, J. and T. J. Ahrens, Shock-induced effects in calcite from Cactus Crater, Geochim. Cosmochim. Acta, 44, p. 1059-1069, 1980.

Wilson, H., Ceramics-Clay Technology, McGraw-Hill Book Company Inc. (New York), p. 58-59.

Yurk, Y. Y., G. K. Yeremenko and Y. A. Polkanov, The Boltysh depression - a fossil meteorite crater, Internat. Geol. Rev. 18, p. 196-202, 1975.

Chapter 6

SHOCK COMPRESSION OF ARAGONITE AND IMPLICATIONS FOR THE EQUATION OF STATE OF CARBONATES

Introduction

Compressive behavior in the $CaCO_3$ system has generated interest since the discovery by Bridgman in 1939 of two low pressure phase transitions in calcite. While subsequent static and dynamic compression studies have extended the calcite pressure-density field to 94 GPa (Huang and Wyllie, 1976; Ahrens et al., 1966; Adadurov et al., 1961; Kalashnikov et al., 1973) only limited compressibility data exist on its high pressure polymorph, aragonite. The static experimental results on aragonite by Bayuk, Volorovich and Yefimova (1974) and Jamieson (1957) are limited to pressures of 1.5 and 2.4 GPa, respectively; until the present investigation, no shock compression aragonite data have been available.

The purpose of this investigation is two-fold: first, to determine the shock compression curve of aragonite, identify any possible phase transitions and speculate as to their nature, and to compare it to the calcite Hugoniot; and second, to measure release isentropes for aragonite and thus gain insight into the behavior upon release from shock pressure of carbonates in general.

Results from the first of these efforts are of interest from the crystallographic and mineralogical point of view. The investigation of shock compression and release behavior of carbonates is particularly

relevant to studies of cratering mechanics and impact metamorphism, areas which have suffered from the limited availability of dynamic compression and release data on volatile containing rocks and minerals. Approximately 30% of the known or probable terrestrial meteorite impact craters occur at least partially in carbonate rocks (Dence et al., 1977). Also, carbonate rocks may comprise a significant portion of the cratered Martian surface (Booth and Kieffer, 1978), and have been suggested as being the primary phases which determine the partial pressure of CO_2 on the surface of Venus (Lewis, 1970). In addition, a large class of craters for which energies are approximately known, the Pacific Test Site nuclear craters, were formed in calcite and aragonite containing coralline limestone. The shock compression and release data presented in this paper should aid in understanding impact and explosion processes in these various carbonate terranes. Along these same lines, the release results should provide a firmer basis for estimating the contribution of shock-produced volatiles to an evolving atmosphere.

Experimental Details and Data Reduction

The aragonite samples used in this study were pseudo-hexagonal twinned crystals collected by A. Jones near Minglanilla, Spain. The doubly-terminated prisms, formed by an intergrowth of three individuals twinned on the (110) plane, display an approximately hexagonal cross-section with small re-entrant angles often appearing as prism faces at the twin boundaries. Guinier camera X-ray analysis verified the identity of the crystals and microprobe analysis indicated a relatively pure $CaCO_3$ composition (see Table 6-1).

Table 6-1

MICROPROBE ANALYSIS OF ARAGONITE CRYSTALS

Oxide	Weight %*
CaO	54.69
SrO	0.85
P_2O_5	0.04
CO_2	43.24
MnO	Trace
Na_2O	Trace
FeO	Trace
Total	98.82

* Average of 5 analyses by A. Chodos,

California Institute of Technology

Crystals with a minimum of cracking and discoloration (presumably due to iron and/or manganese), and measuring 15 to 20 mm in width were cut into 3 to 4 mm thick sections and lapped to within uniform thickness tolerances of 0.1 - 0.3% (i.e., ±3-10 μm). Archimedean densities were determined using reagent grade toluene as a solvent and the temperature corrections of Berman (1939). Individual density measurements varied by ±0.001 g/cc, while the average density for all 12 samples was 2.928 g/cc with a standard deviation of 0.003 g/cc. The close agreement between this measured average density and the X-ray density of 2.930 g/cc is probably due to a fortuitous cancellation of the effects of impurities and cracks. Due to the irregular shape of the crystal sections used in the experiment, bulk density determinations were not performed each time. To obtain an approximate measure of sample porosity, a rectangle was cut from an aragonite crystal and lapped to within dimensional tolerances of 0.1%; the porosity determined from this measurement was 1.7%.

The samples were then mounted on either 2024 Al or Ta driver plates with the c axes, as determined by crystal morphology, oriented perpendicular to the plate (i.e., parallel to the shock propagation direction). Arrays of 5 lexan mirrors were, in turn, mounted on the sample and the driver plate; care was taken to position the mirrors, particularly the inclined wedge, away from cracks in the sample. The entire sample assembly is pictured in Fig. 6-1a. A 40 mm propellant gun, described by Ahrens et al. (1971) was used to accelerate lexan projectiles fitted with either 2024 Al or Ta flyer plates to velocities in the range of 0.7 to 2.4 km/sec. Projectile velocities were measured using laser beam obscuration times. Sample and buffer mirror shock velocities were

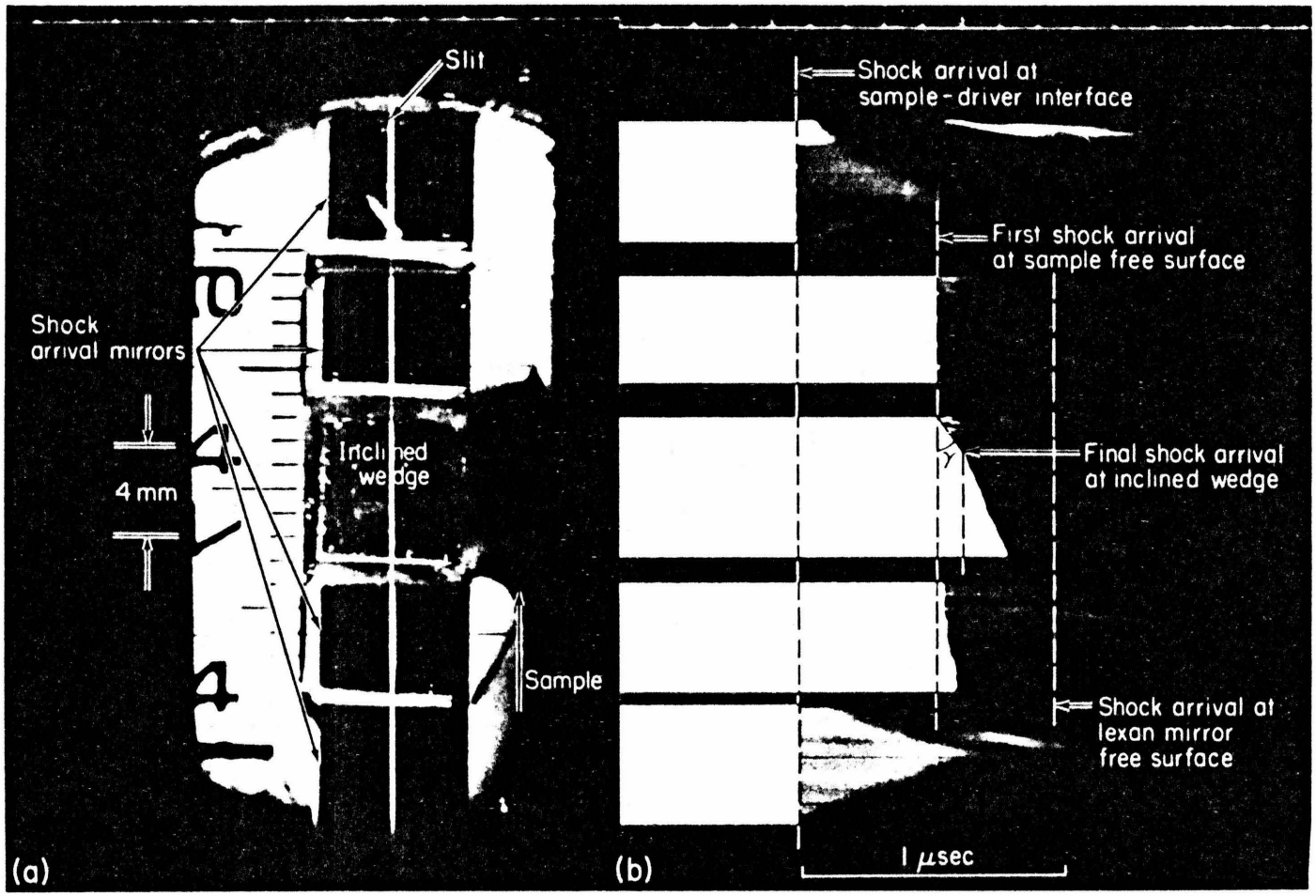

Figure 6-1. (a) Still photograph taken through streak camera showing imaging slit position. (b) Streak image demonstrating two-wave structure recorded by inclined wedge.

obtained from observations of shock-induced loss of mirror reflectivity at successive reflective surfaces as recorded by a rotating-mirror streak camera; an example of such a streak record is shown in Fig. 6-1b.

Pressure-particle velocity and pressure-density states on the sample Hugoniot were calculated from measured projectile and sample shock velocities and known equations of state of 2024 Al and Ta (McQueen et al., 1970) by use of the Rankine-Hugoniot equations and the impedance-match procedure (Rice et al., 1958). For experiments in which a two-wave structure was detected, the free-surface approximation (Walsh and Christian, 1955) was made, i.e., it was assumed that the particle velocity, $u_{p_1} \approx u_{fs}/2$, where the free surface velocity, u_{fs}, is obtained from the inclined mirror extinction angle (Ahrens and Gregson, 1964). The pressure-density state behind the first shock was then calculated from the Rankine-Hugoniot relations. The second shock state was calculated by impedance matching using the velocity of the second shock wave. Loss of reflectivity of the free buffer surface (see Fig. 6-1b) allowed calculation of the buffer mirror shock state, and, hence, sample partial release state by use of experimental Hugoniot data for lexan (Carter and Marsh, 1980) and the Riemann integral (Rice et al., 1958). Free surface velocities, as determined from inclined wedge extinction angle measurements and the Riemann formulation, provided upper bounds for the post-shock zero-pressure density (Lyzenga and Ahrens, 1978).

Results

Experimental results for aragonite Hugoniot and release states are listed in Table 6-2 and presented in particle velocity - shock velocity (u_p, U_s) and density-pressure (ρ,P) diagrams in Figs. 6-2 and 6-3,

Table 6-2

SUMMARY OF HUGONIOT AND RELEASE MEASUREMENTS

Shot	Flyer/ Driver Material	Projectile Velocity, km/sec	Initial Density, g/cc	Hugoniot state[a] Shock Velocity, km/sec	Hugoniot state[a] Particle Velocity, km/sec	Hugoniot state[a] Pressure, GPa	Hugoniot state[a] Density, g/cc	Partial Release State Buffer Shock Velocity, km/sec	Partial Release State Particle Velocity, km/sec	Partial Release State Pressure, GPa	Partial Release State Density, g/cc	Zero-Pressure Release State Free Surface Velocity, km/sec	Zero-Pressure Release State Maximum Post-shock Density, g/cc
382	2024 Al	1.194 ±0.005	2.925 ±0.001	6.26[b] ±0.04	0.41[b] ±0.02	7.45[b] ±0.2	3.13[b] ±0.01						
				4.71 ±0.04	0.60 ±0.02	10.23 ±0.15	3.27 ±0.01	3.53 ±0.04	0.76 ±0.02	3.23 ±0.1	3.23 ±0.1	1.13 ±0.02	3.00 ±0.02
383	2024 Al	0.782 ±0.005	2.929 ±0.001	6.00[c] ±0.08	0.11[c] ±0.01	1.84[c] ±0.1	2.98[c] ±0.01						
				4.92 ±0.1	0.40 ±0.01	6.18 ±0.2	3.18 ±0.04	2.98 ±0.05	0.41 ±0.03	1.47 ±0.1	3.18 ±0.1	0.93 ±0.01	2.78 ±0.01
393	Ta	1.376 ±0.005	2.926 ±0.001	6.85 ±0.09	1.05 ±0.01	20.97 ±0.3	3.45 ±0.01	5.38 ±0.2	1.94 ±0.1	12.51 ±1.3	2.60 ±0.3	1.68 ±0.01	3.24 ±0.04
402	2024 Al	0.934 ±0.005	2.923 ±0.001	5.78[c] ±0.2	0.14[c] ±0.01	2.33[c] ±0.4	2.99[c] ±0.04						
				4.98 ±0.3	0.48 ±0.02	7.47 ±0.5	3.22 ±0.07	3.29 ±0.1	0.61 ±0.06	2.40 ±0.3	3.19 ±0.1	0.80 ±0.02	3.09 ±0.02
423	2024 Al	1.059 ±0.005	2.925 ±0.001	6.29[b] ±0.06	0.30[b] ±0.02	5.55[b] ±0.24	3.07[b] ±0.01						
				5.61 ±0.05	0.51 ±0.01	9.20 ±0.14	3.20 ±0.01	3.48 ±0.1	0.74 ±0.09	3.06 ±0.5	3.12 ±0.1	1.02 ±0.02	2.94 ±0.02
491	2024 Al	1.998 ±0.01	2.928 ±0.001	6.34 ±0.04	1.02 ±0.01	18.16 ±0.1	3.51 ±0.01	4.67 ±0.05	1.70 ±0.06	10.20 ±0.5	2.91 ±0.1	2.58 ±0.01	2.39 ±0.04
494	Ta	1.237 ±0.005	2.933 ±0.001	6.25 ±0.04	0.96 ±0.01	17.54 ±0.16	3.46 ±0.01	4.97 ±0.16	1.68 ±0.1	10.01 ±0.9	2.78 ±0.22	1.87 ±0.01	2.98 ±0.03

Shot	Flyer/ Driver Material	Projectile Velocity, km/sec	Initial Density, g/cc	Hugoniot state [a] Shock Velocity, km/sec	Hugoniot state [a] Particle Velocity, km/sec	Hugoniot state [a] Pressure, GPa	Hugoniot state [a] Density, g/cc	Partial Release State Buffer Shock Velocity, km/sec	Partial Release State Particle Velocity, km/sec	Partial Release State Pressure, GPa	Partial Release State Density, g/cc	Zero-Pressure Release State Free Surface Velocity, km/sec	Zero-Pressure Release State Maximum Post-shock Density, g/cc
496	Ta	2.414 ±0.01	2.928 ±0.001	7.40 ±0.05	1.83 ±0.01	39.74 ±0.3	3.89 ±0.01	6.54 ±0.01	2.68 ±0.01	21.00 ±0.4	3.38 ±0.15	4.03 ±0.01	2.64 ±0.15
497	Ta	1.736 ±0.01	2.932 ±0.001	6.75 ±0.02	1.33 ±0.01	26.32 ±0.17	3.65 ±0.01	5.41 ±0.03	1.96 ±0.02	12.72 ±0.22	3.30 ±0.05	2.68 ±0.01	2.92 ±0.04
498	2024 Al	0.712 ±0.005	2.930 ±0.001	5.66 [c] ±0.09	0.20 [c] ±0.01	3.26 [c] ±0.2	3.04 [c] ±0.05						
				4.51 ±0.09	0.37 ±0.01	5.58 ±0.5	3.16 ±0.06	2.89 ±0.1	0.36 ±0.06	1.23 ±0.26	3.16 ±0.05	0.76 ±0.02	2.91 ±0.05
499	2024 Al	1.550 ±0.01	2.930 ±0.001	6.42 [b] ±0.02	0.41 [b] ±0.02	7.64 [b] ±0.3	3.13 [b] ±0.02						
				5.67 ±0.03	0.76 ±0.03	13.98 ±0.6	3.36 ±0.2	3.93 ±0.01	1.02 ±0.01	4.78 ±0.4	3.28 ±0.05	1.43 ±0.02	3.22 ±0.02
502	Ta	2.063 ±0.01	2.932 ±0.001	7.05 ±0.02	1.58 ±0.01	32.53 ±0.18	3.78 ±0.01	5.98 ±0.04	2.33 ±0.03	16.64 ±0.29	3.33 ±0.04	2.86 ±0.05	3.17 ±0.05

(a) Final shock state unless otherwise noted.

(b) Intermediate deformational shock state.

(c) Hugoniot elastic limit shock state.

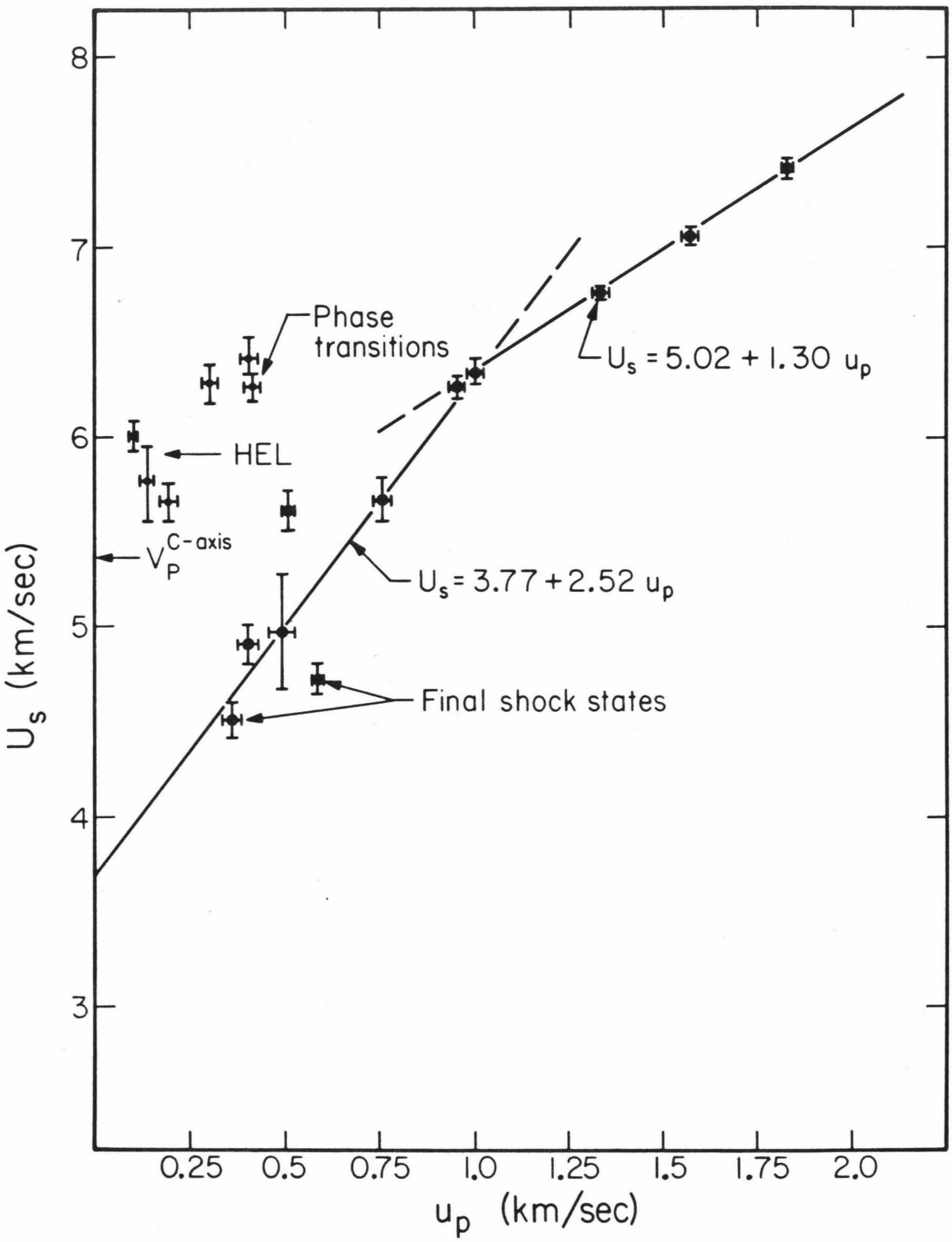

Figure 6-2. Aragonite Hugoniot data in the (u_p,U_s) plane. Large dots represent final shock states. Elastic and intermediate shock states are labelled "HEL" and "Phase transitions", respectively.

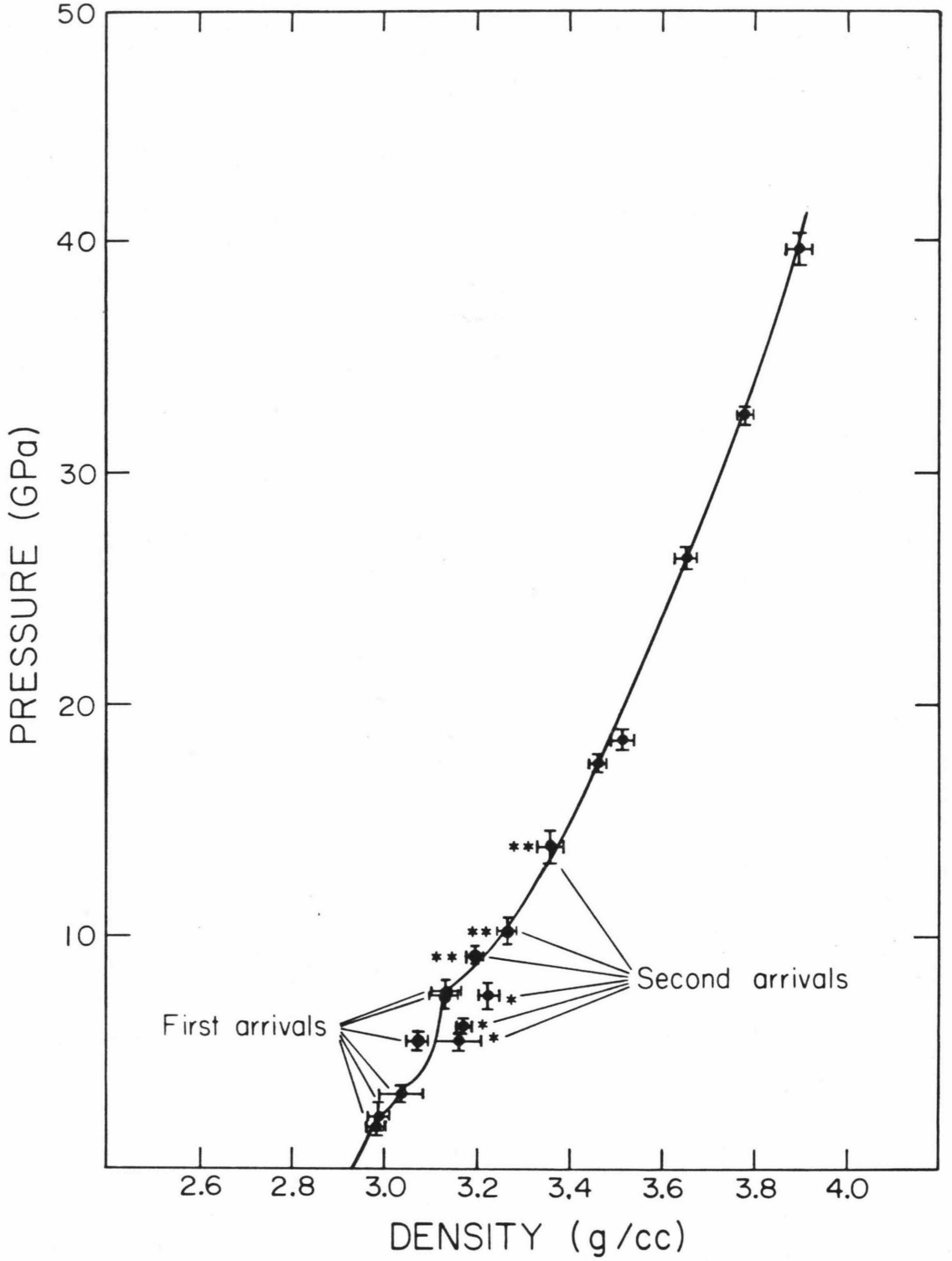

Figure 6-3. Aragonite Hugoniot data in the (ρ,P) plane.

respectively.

In six of the experimental shot records, a two-wave structure, such as that displayed in Fig. 6-1b, was observed. Three of these double-shock experiments, shots 383, 402 and 498, are interpreted as representing an elastic to plastic shock transition. (It is also possible that shot 498 represents a phase transition occurring at $\sim$ 3.3 GPa. However, due to the lack of any corroborative evidence, it will be grouped, for discussion purposes, with the two lowest pressure experiments.) Comparing the shock velocity of the first wave to the longitudinal wave velocity along the c-axis of aragonite identifies this first wave as elastic. The only published single crystal data of which we are aware are those of Voigt (1910). (Bayuk et al., 1974, report polycrystalline aragonite results.) From the elastic stiffness (c_{33}) listed in Voigt's work, a compressional wave velocity along the c-axis is computed from the appropriate equation for an orthorhombic crystal:

$$V_P^{c\text{-axis}} = \sqrt{\frac{c_{33}}{\rho}} = 5.39 \text{ km/sec} \qquad (6\text{-}1)$$

This agrees well with our recent ultrasonic measurement: $V_P^{c\text{-axis}} = 5.39 \pm 0.035$ km/sec (Ken-ichi Kondo, 1981, personal communication). The observed shock velocities of the assumed elastic wave, ranging from 5.67 to 6.00 km/sec, are, as expected (Davison and Graham, 1979), slightly greater than the ultrasonically measured number. An additional argument for the interpretation of these velocities as elastic comes from the agreement of their corresponding shock pressures, 1.8 to 3.3 GPa, with Hugoniot elastic limit pressures of 1.5 to 2.5 GPa determined for single crystal calcite by Ahrens and Gregson (1964).

As seen in Fig. 6-3, the deformational shock states following the elastic wave indicated by a "*" are considerably displaced from the aragonite Hugoniot, as defined below 8 GPa by 6 first arrival states both in the elastic and plastic regime (specifically, first arrivals in shots 382, 383, 402, 423, 498 and 499). However, in double-shock experiments where the first wave is in the plastic regime (shots 382, 423 and 499), second arrival shock states ("**" in Fig. 6-3) are consistent with both the low pressure Hugoniot, as defined in the last sentence, and the high pressure (above 17 GPa) Hugoniot. Thus, the deformational shock states indicated by * in Fig. 6-3 are anomalous with respect to all other experimental points. The reason for these deviations may lie in some undetermined phenomena associated with the elastic to plastic shock transition.

On a shock velocity-particle velocity plot, data for the first deformational waves, from those double-wave experiments in which both shock states are in the plastic regime (shots 382, 423 and 499), form a cluster at U_s values greater than those attributed to the elastic wave, and at low u_p values (see Fig. 6-2). As seen on the pressure-density plot (Fig. 6-3), two of these "intermediate" state values form a distinct cusp at $\sim$ 7.5 GPa which appears to divide the aragonite Hugoniot into a decidedly steeper (albeit poorly defined) low pressure part and a well-defined shallower high pressure part. On the basis of these observations, a phase change in aragonite is tentatively inferred to occur between shock pressures of 5.5 to 7.6 GPa.

As already mentioned, several aspects of the low pressure data remain enigmatic. It would appear from Fig. 6-2 that U_s-u_p values from the second wave-arrivals in the six double-wave experiments together

outline a poorly defined general trend. Such coincidence, however, would be unexpected in light of the interpretation that three of these points (with the lowest u_p values) correspond to an intermediate shock state while the other three represent some higher pressure state. The six second wave arrival points were fit to provide the linear least squares relationship:

$$U_s = 3.77 + 2.52\ u_p \qquad r^2 = 0.81 \tag{6-2}$$

where 3.77 km/sec and 2.52 represent the constants c_o and s, respectively, of the U_s-u_p Hugoniot representation, and r^2 is the square of the correlation coefficient. The intercept of 3.77 km/sec is comparable to the bulk sound velocity of 4 km/sec derived from the bulk modulus given by Voigt (1910). Correcting the data for sample compression or wave interaction effects would move the points in Fig. 6-2 to slightly lower U_s and/or higher u_p values, and the linear regression would be slightly displaced toward the lower U_s side. Due to the minimal effect of such adjustments (see e.g. Ahrens et al., 1968), the large amount of scatter in our data, and the ambiguity in the constitutive relation of aragonite, the data are reported here without such correction. Further justification for the fit of Eq. (6-2) will be provided by the comparison of aragonite and calcite low pressure data (next section).

For particle velocities above 1 km/sec, the U_s-u_p data form a consistent set described by the linear regression:

$$U_s = 5.02 + 1.30\ u_p \qquad r^2 = 0.99 \tag{6-3}$$

(Because of an unclear photographic record, shot 393 results are not included in this fit.) As seen in Fig. 6-2, this latter trend is

distinct from that observed at particle velocities below 1 km/sec, and indicates the onset of greater compressibility in aragonite at the corresponding shock pressure of 18 GPa. This shift to more compressible behavior, reminiscent of mixed phase regimes in silicates (McQueen et al., 1967), does not appear, however, as a decrease in slope above 18 GPa on the pressure-density Hugoniot (Fig. 6-3). Further speculation on the higher pressure half of the aragonite Hugoniot and its relation to that of calcite will be presented in the next section.

Partially released states achieved by rarefaction wave propagation into the aragonite samples from the buffer-sample interface, together with calculated maximum post-shock densities achieved on complete release are plotted in pressure-density space in Fig. 6-4. Two distinct trends are evident. Release paths originating at Hugoniot states at or below $\sim$ 14 GPa are consistently steeper than the Hugoniot at these pressures, and the corresponding maximum post-shock densities suggest density increases upon complete release of up to 10%. (For clarity's sake, release paths for the three lowest pressure Hugoniot points are not shown.) Steep release adiabats, from shock pressures above the suspected onset of a phase transformation, have been observed for a number of silicates, including quartz (Grady et al., 1974), plagioclase feldspar (Ahrens et al., 1969), and olivine (Jackson and Ahrens, 1979), and have been interpreted to indicate retention of the denser high pressure phase during the initial stages of unloading. The same interpretation may be invoked for aragonite released from pressures between 5 and 14 GPa.

With one exception, anomalously shallow release paths are observed upon unloading from Hugoniot shock pressures above 16 GPa. The one

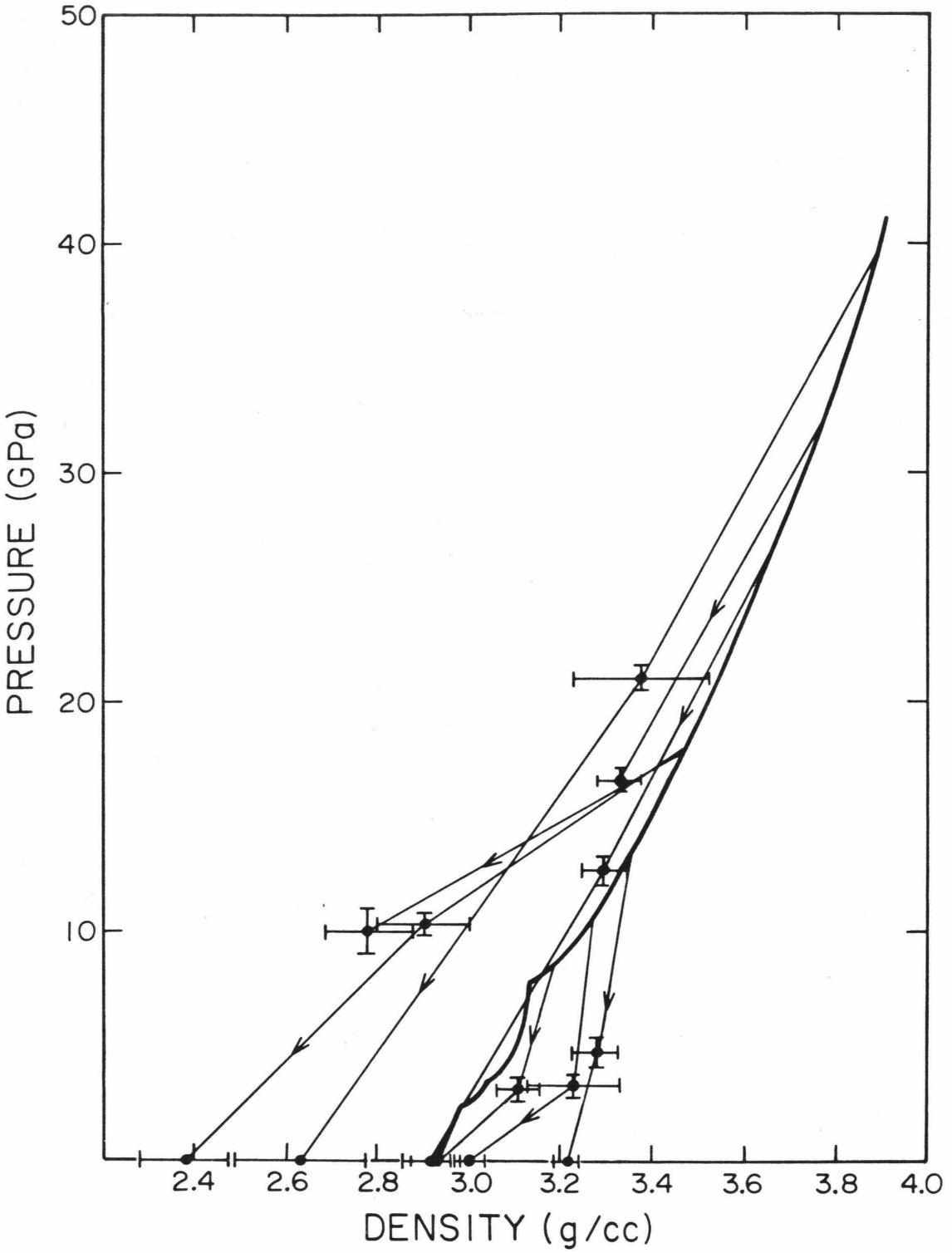

Figure 6-4. Aragonite release adiabat states. Intermediate states determined from shock velocity measurements through buffer mirrors and complete release states from inclined wedge extinction angle measurements.

exception, at ∿ 26 GPa, displays a slope approximately parallel to that of the Hugoniot. Partial vaporization upon release might be expected to produce the observed release paths. Whether or not the phenomena can occur under the pressure-temperature states achieved upon unloading will be discussed in the next section. The calculated maximum post-shock densities for those high pressure experiments do not form an internally consistent set, i.e., there is no continuous relationship between shock pressure and the zero-pressure density. In addition, two of the zero-pressure density values (shots 393 and 494) are inconsistent with the partially released states. The zero-pressure density values that are consistent with the partially released states suggest distentions upon complete unloading of up to ∿ 20%.

Discussion of Aragonite Results and Comparison with Calcite Hugoniots

Considering the plausibility of shock-induced transitions between calcite and aragonite, we will use the comparison of Hugoniot data for both minerals in an attempt to reinforce some of our tentative interpretations of the low pressure aragonite Hugoniot results, and to draw some general conclusions on the shock compression and release behavior of carbonates at high pressure.

Although displaying a large amount of scatter, the low pressure aragonite data, as seen in Figs. 6-2 and 6-3, suggest a Hugoniot elastic limit (HEL) at ∿ 2 GPa and a phase transition between 5.5 and 7.6 GPa. At pressures above those of the inferred phase transition, the aragonite Hugoniot displays a distinctly shallower slope. The single crystal calcite (ρ_o = 2.71 g/cc) Hugoniot (Ahrens and Gregson, 1964; Ahrens et al., 1966), shown in Fig. 6-5 displays an orientationally dependent

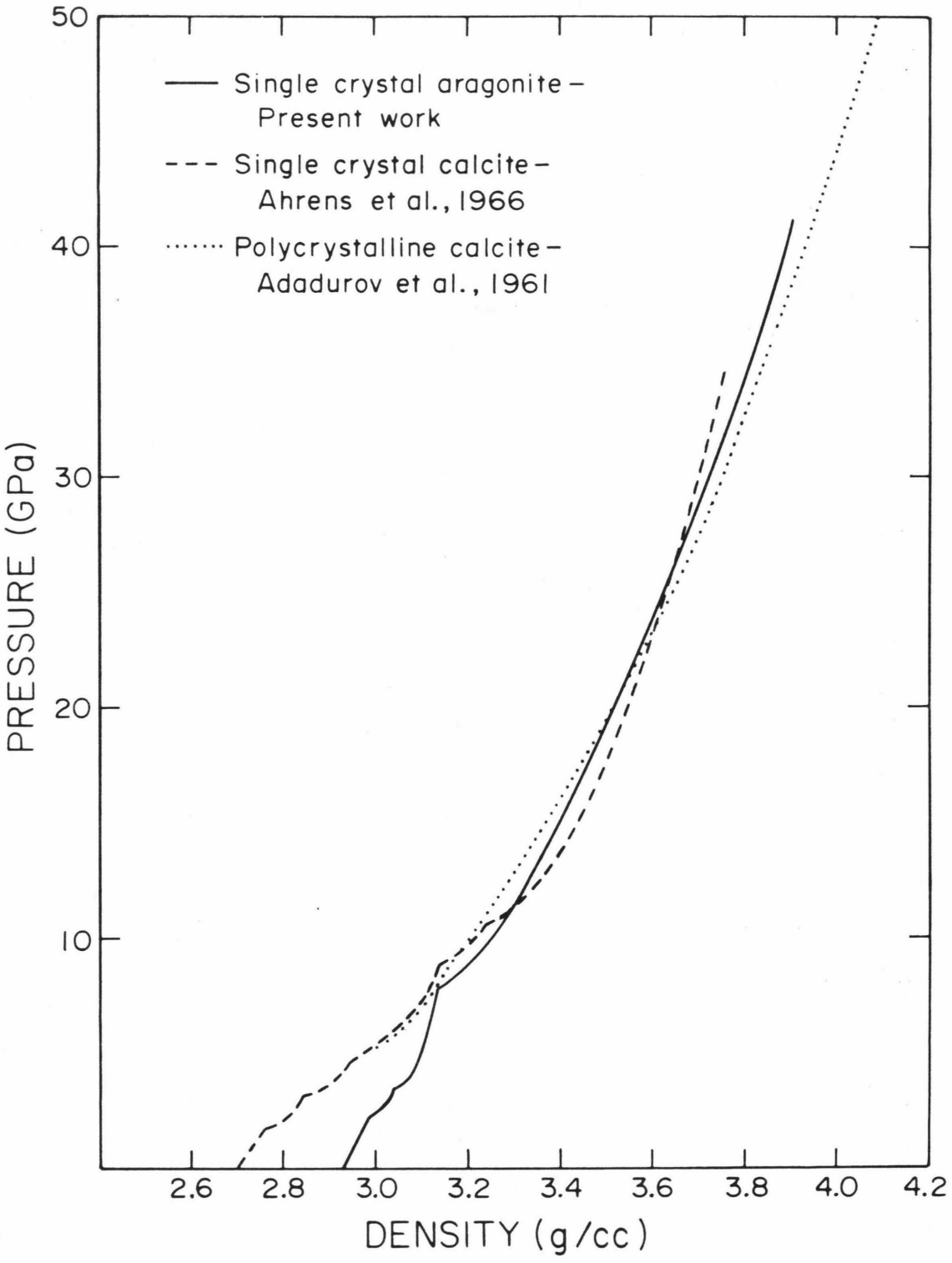

Figure 6-5. Hugoniot data for carbonate minerals and rocks, including present aragonite Hugoniot determination.

HEL between 1.8 and 2.4 GPa and a series of three, or possibly four, cusps below ∿ 10 GPa, indicative of phase transitions in this low pressure region. It is the c-cut calcite Hugoniot that is drawn in Fig. 6-5; above approximately 10 GPa, this curve is representative of a- and b-cut calcite Hugoniot data as well. At 9.5 GPa and 7.5 GPa on the calcite and aragonite Hugoniots, respectively, the densities of these two polymorphs coincide, and at shock pressures above ∿ 10 GPa, their Hugoniots are essentially indistinguishable, suggesting the conversion of both these minerals to the same high pressure phase.

Attempts to characterize the low pressure aragonite transition(s) are hampered by the lack of definitive static compression data on this mineral. However, consideration of low pressure static and dynamic compression data for calcite might lend insight into the nature of this transition (or transitions) and into the possibility and mechanisms of a parallel evolution of calcite and aragonite to a common high pressure phase. Compressional studies on calcite are relatively abundant and date back to the pioneering studies of Bridgman. In 1939, he first observed the transitions from calcite I, the atmospheric pressure phase, to calcite II at 1.44 GPa, and from calcite II to III at 1.77 GPa; both of these transitions occur in the stability field of aragonite. These results have recently been confirmed in volumetric compression studies on single crystal calcite by Singh and Kennedy (1974). Adadurov et al. (1961) claim to have observed three transitions in marble at 1.1, 1.6 and 2.2 GPa; these results, however, have not been duplicated in other static compression measurements. The mechanisms of transition have been investigated by several groups of workers with little agreement in their

conclusions. Jamieson (1957), on the basis of thermodynamic arguments, proposed a second-order calcite I to II transition involving anion disordering similar to that inferred for $NaNO_3$ (Siegel, 1949) and for Sr and Ba carbonates (Lander, 1949). According to Davis (1964), calcite II is not anion disordered but is a minor variation of the calcite I structure. The structure of calcite III is also investigated in this work and is classified as orthorhombic. Merrill and Bassett (1975) claim that the calcite I to II transition involves an 11° rotation of the carbonate groups and a slight displacement of planes of calcium atoms parallel to $(10\bar{1}4)$, resulting in a monoclinic structure. Recently, Brar and Schloessin (1980) considered the calcite I to II to III transitions as rotatory attempts towards the calcite to aragonite transition and found the calcite I to II transition mechanism proposed by Merrill and Bassett to be most consistent with their broader speculative framework.

Evidence for the occurrence of the calcite I to II to III transitions within the micro-to nano-second time scale of shock wave experiments has been noted by several workers for single crystal calcite and calcite rock. As previously mentioned, Ahrens and Gregson (1964) observed three, or possibly four, cusps in the calcite Hugoniot and related these phase transitions to those observed in static experiments. Grady et al (1978) obtained stress-particle velocity profiles for two limestone and a marble rock which indicated the occurrence of one phase transition between 0.6 and 1.2 GPa and another beginning at 2.4 GPa. On the basis of several features of the loading and release wave profiles, they interpret the first (calcite I to II) transition to be displacive and speculate

that the calcite II to III transition is reconstructive.

The calcite to aragonite transformation under conditions of static high pressure has been extensively studied. Jamieson (1953) performed the initial experiments determining the phase boundary to ∿ 0.5 GPa; MacDonald (1956), Crawford and Fyfe (1964) and Irving and Wyllie (1973) among others, have extended the transition boundary to 3.5 GPa (and ∿ 1200°C). The calcite to aragonite transition has also been accomplished by prolonged grinding with mortar and pestle (Jamieson and Goldsmith, 1960). Ahrens and Gregson (1964) and Grady et al. (1978) speculate on the possibility of a calcite to aragonite transition in shock experiments, but can make no conclusions based on their data. Leiserowitz and Schmidt (1966) claim to have produced aragonite in shock recovery experiments on samples of calcite with 10% water added; they do not, however, document their experimental pressures.

Static compression data on aragonite are extremely limited. Bayuk, Volorovich and Yefimova (1974) determined the volumetric compressibility of aragonite up to 1.5 GPa, and Jamieson (1957) used a diamond anvil to raise aragonite to 2.4 GPa; neither irregularities in the compressibility curve nor X-ray evidence for structural re-adjustment were observed. Thus, inferences as to the nature of the 6.5 ± 1 GPa (and possibly a 3.3 GPa) transition recorded in shock experiments can only be based on structural considerations using the calcite Hugoniot as an analogue. The transition from calcite to aragonite involves a 30° rotation of the carbonate groups and a translation of calcium atom planes (Dasgupta, 1963). As we have discussed, the calcite I to II transition may represent the initial step in a series of rotations and translations

leading to the aragonite configuration. It is possible, therefore, that the translation plus rotation scenario occurs in the case of aragonite as well, and may be responsible for the transition at 5.5 to 7.6 GPa. The fact that the U_s-u_p states corresponding to this transition point lie above the fit described by Eq. (6-2) (Fig. 6-2), similar to the pattern observed in the low pressure calcite U_s-u_p data (Ahrens and Gregson, 1964), lends further weight to the argument that the aragonite transition is a minor structural readjustment involving carbonate group rotation and calcium atomic plane displacement. Assuming that the first two cusps on the single crystal calcite Hugoniot (Fig. 6-5) correspond to the calcite I to II and II to III transitions, the third may represent the calcite III to transformed aragonite transformation; alternatively, calcite III may first convert to the STP form of aragonite and undergo further readjustment at higher pressure, possibly at the 9.5 GPa cusp mentioned in Ahrens and Gregson (1964).

Above approximately 10 GPa, the Hugoniots of calcite and aragonite are, within the uncertainties in the data, indistinguishable in the pressure-density plane. However, a significant change in the U_s-u_p plots of both polymorphs is observed at corresponding pressures greater than 10 GPa. Our aragonite U_s-u_p data, together with that of non-porous and porous polycrystalline calcite, are presented in Fig. 6-6; fits for the various data sets are summarized in Table 6-3. Note, first of all the similarity in the slope of the fits to our aragonite and to the Adadurov et al. (1961) marble data at low (below $\sim$ 1 km/sec) particle velocities, which further reinforces our fit to the very scattered low pressure aragonite data. At particle velocities of 0.9 and 1.0 km/sec, the U_s-u_p slopes of calcite (Adadurov et al. data) and aragonite,

Table 6-3

SUMMARY OF CARBONATE HUGONIOT DATA

Sample	Source	ρ_o (g/cc)	c_o (km/sec)	s	Pressure Range (GPa)
Single crystal aragonite	Present work	2.930	3.77	2.52	6 → 18
			5.02	1.30	18 → 40
Polycrystalline calcite	Adadurov, et al., 1961	2.703	3.40	2.00	5 → 13
			3.99	1.32	13 → 51
Polycrystalline calcite	Kalashnikov, et al., 1973	2.665	3.70	1.44	10 → 94
		2.020	1.74	1.61	13 → 71
		1.705	1.15	1.60	10 → 59
Solenhofen limestone	van Thiel, et al., 1977	2.585	3.62	1.39	8 → 90

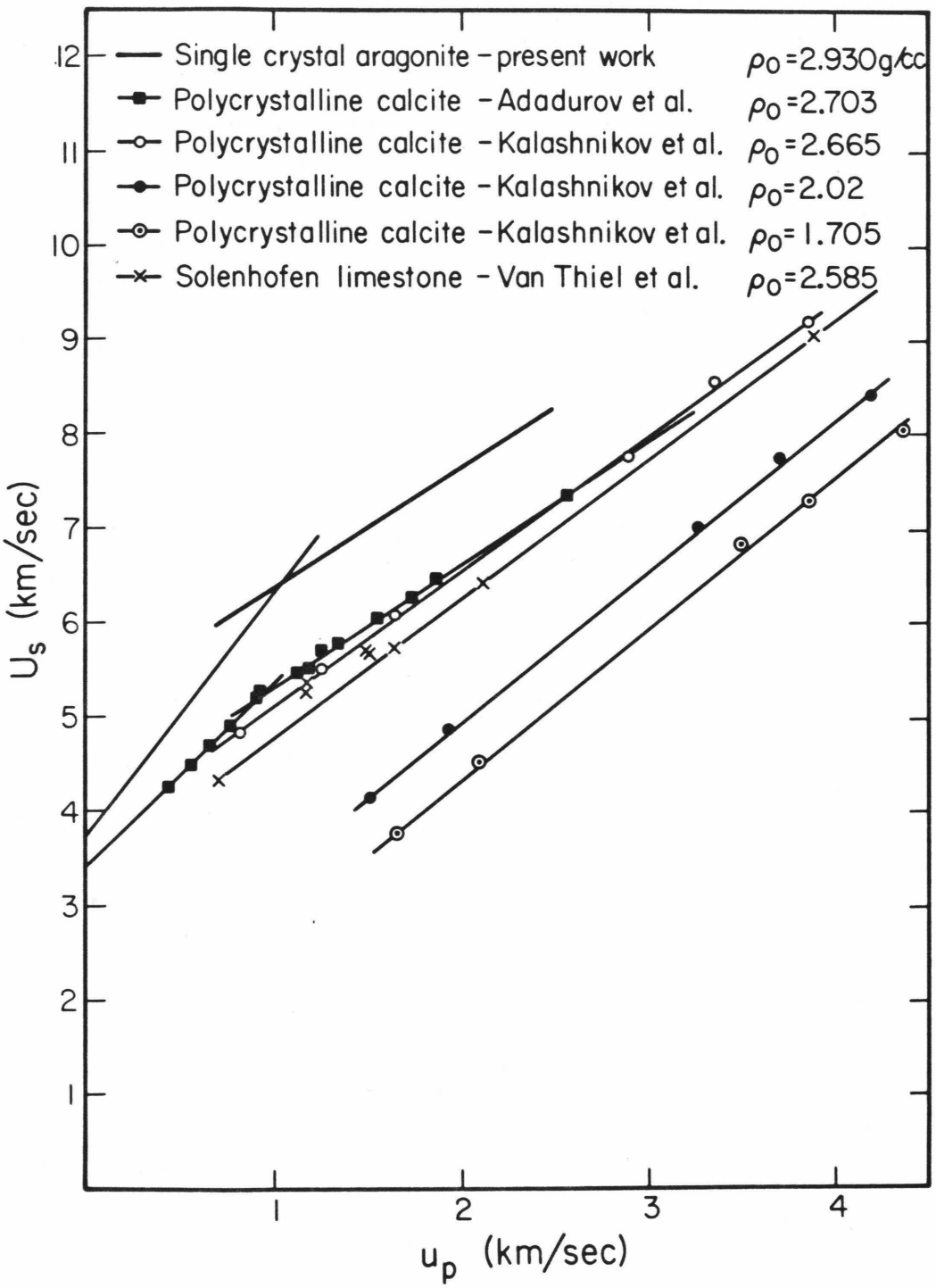

Figure 6-6. Comparison of carbonate Hugoniot data, including porous polycrystalline calcite, in the u_p,U_s) plane. Parameters of fits to the data are presented in Table 3.

respectively, undergo a shift to shallower values within 2% of each other. In fact, the slopes of all the carbonate data above $u_p \approx 1$ km/sec are sub-parallel. This pattern is typically displayed by data sets for materials of varying porosities (see e.g. Carter and Marsh, 1980) whereby increasingly porous sample U_s-u_p fits lie at lower U_s values. Also, the apparent shift of the slope break toward higher u_p values with increasing $CaCO_3$ starting density is consistent with the observation made by Jackson and Ahrens (1979) on porous forsterite data. They speculate that increased internal energies at greater material porosities facilitate the onset of phase transitions at lower shock pressures.

Although the data presented in Fig. 6-6 point strongly to attainment of an identical structure at high pressures by calcite and aragonite, they do not shed light on the nature of this transition. Three possibilities are: 1) transformation to a high pressure phase at $\sim$ 15 GPa and $\sim$ 18 GPa on the calcite and aragonite Hugoniots, respectively, 2) onset of a mixed phase regime at these same pressures, and 3) incipient melting. With regard to the third interpretation, there are, as discussed by McQueen et al. (1967), no features intrinsic to either a U_s-u_p or P-ρ representation of melting along a Hugoniot that would allow unequivocal identification of this phenomenon. The coincidence of a break in the U_s-u_p slope with the intersection of the melting curve and the Hugoniot would, however, provide some indication of melting during shock compression. In an extensive investigation of phase transitions during shock processes, Carter (1973) showed that minor slope changes in the U_s-u_p slopes of Eu, Er and Pb do, in fact, coincide with the calculated melting and experimental Hugoniot curve intersections, and concluded shock melting for these metals. However, the slope change in

the aragonite U_s-u_p Hugoniot is a major discontinuity, and, as will be shown by Hugoniot temperature calculations presented in the following paragraphs, melting does not appear to be a feasible mechanism for the observed behaviour. The second possibility is considered because, very typically, in the case of silicate mineral and rock Hugoniots, a decrease in U_s-u_p slope indicates the onset of a mixed phase regime. The trends displayed by the carbonate data are not inconsistent with this interpretation; however, such an assumed mixed phase region would have an uncharacteristically long duration. As seen in Fig. 6-6, even the most porous data of Kalashnikov et al. (1973) do not deviate from linearity at high u_p values, and his non-porous results would indicate the existence of a mixed phase region between 15 and 94 GPa; the improbability of such a phenomenon leads to rejection of the second possibility. The first possibility, i.e. transition to a high pressure phase, remains a viable explanation.

In order to more thoroughly evaluate the feasibility of these speculations, we will attempt to construct an isentrope for the high pressure $CaCO_3$ phase and use this reference curve to calculate temperatures along the calcite and aragonite Hugoniots. A third-order Eulerian (Birch-Murnaghan) formulation is assumed for the high pressure phase isentrope:

$$P_S(\rho) = \frac{3K}{2}\left[(\rho/\rho_o)^{7/3} - (\rho/\rho_o)^{5/3}\right] \cdot \left[1 + \frac{3}{4}\{K' - 4\}\{(\rho/\rho_o)^{2/3} - 1\}\right] \qquad (6\text{-}4)$$

where ρ_o is the zero-pressure density, and K and K' are the zero-pressure values of the bulk modulus and first pressure derivative,

respectively, of the high pressure phase. This calculated isentrope pressure, P_S, is related to the Hugoniot pressure, P_H, at some given ρ through the Mie-Grüneisen thermal equation of state:

$$P_H = \left[P_S - \gamma\rho\ (E_S + E_{TR})\right] \ / \ \left[1 - \gamma(\rho/\rho_o' - 1)/2\right] \qquad (6\text{-}5)$$

where ρ_o', γ, and E_{TR} refer to the initial density of the shocked material, the Grüneisen parameter, and the energy of transition between the low and high pressure phases at S.T.P., respectively. E_S represents the internal energy change with isentropic compression from the zero-pressure density of the high pressure phase, ρ_o, to some given density, ρ:

$$E_S = \int_{\rho_o}^{\rho} \frac{P_S}{\rho^{*2}}\, d\rho^* \qquad (6\text{-}6)$$

Using the appropriate input parameters of ρ_o, K, K', E_{TR} and γ, it should, therefore, be possible to bring the P_H values calculated from Eq. 6-5 into coincidence with the experimentally determined calcite and aragonite Hugoniot.

As already discussed, static compression data that would allow us to characterize the high pressure carbonate phase is not available; ρ_o, K and K', therefore, remain unconstrained parameters. The energy of transition to the high pressure phase is also unknown. However, a lower bound to E_{TR} may be approximated by the sum of transition energies for the calcite I to II and II to III transitions. Using the data of Singh and Kennedy (1974), an E_{TR} for calcite I to III of 24 joules/g is calculated. As listed in Ahrens et al. (1969), typical estimated E_{TR}'s for a variety of minerals range from 300 to $\sim$ 1000 joules/g. However,

since they refer to transitions occurring at pressures in excess of 30 GPa, whereas the carbonate transitions in question occur at pressures 50% lower, an upper E_{TR} limit of 200 joules/g (for the carbonate transitions) appears reasonable. In our isentrope model calculations, therefore, E_{TR} was varied between 20 and 200 joules/g.

The Grüneisen parameter, assumed to be of the form:

$$\gamma = \gamma_o \, (\rho_o/\rho)^n \qquad (6\text{-}7)$$

was determined from the 2 sets of porous calcite data reported by Kalashnikov et al. (1973). The γ's calculated for both data sets are plotted as a function of ρ in Fig. 6-7. An attempt was made to use Solenhofen limestone (4.6% porous) data but the calculated γ values showed extreme scatter. If inferences may be drawn from two data sets, the results of Fig. 6-7 point to a direct dependence of γ on porosity. Therefore, we used the γ formulation determined from the less porous data set, i.e., $\gamma = 1.53 \, (\frac{\rho_o}{\rho})^{0.6}$. The assumption that γ for the high pressure $CaCO_3$ phase is small is also consistent with the close coincidence of the calcite and aragonite Hugoniots at high pressure. Small variations in γ, however, do not significantly affect the model isentrope calculations.

The self-consistent sets of model parameters that best fit experimental calcite and aragonite Hugoniots are summarized in Table 6-4. It is evident from this table that varying the initial high pressure phase density by 0.1 g/cc profoundly affects the bulk modulus and first pressure derivative values in the model calculations. Performing the calculation with ρ_o greater than 3.1 g/cc would constrain K to very high values, above 100 GPa. On the other hand, the calculations are

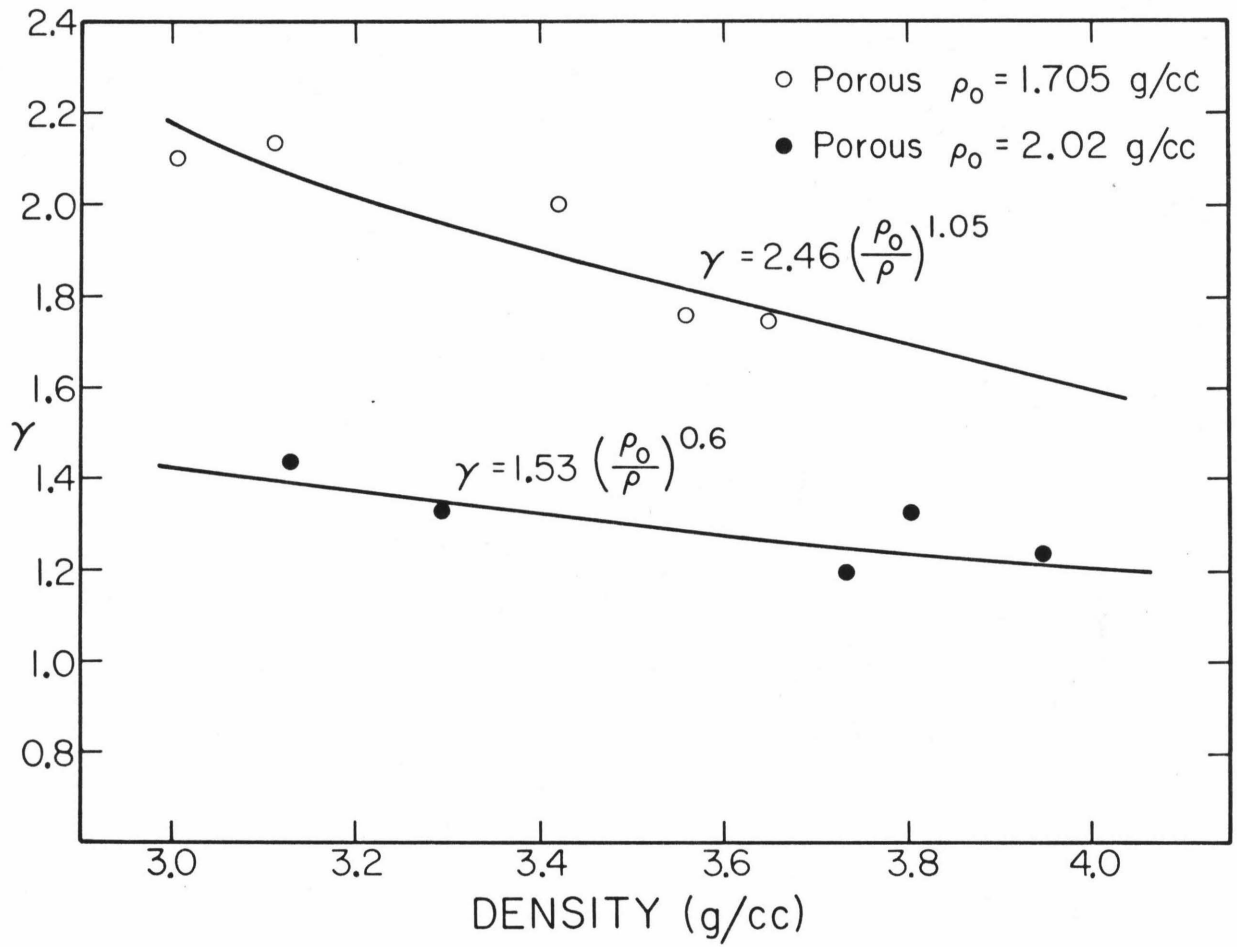

Figure 6-7. Density dependence of Grüneisen's γ, as calculated from porous polycrystalline calcite data of Kalashnikov et al., 1964.

relatively insensitive to changes in E_{TR}. Therefore, even by allowing an E_{TR} of 70 joules/g for the calcite to aragonite transition (assumes calcite III→aragonite transition at 9 GPa), it is not possible to force both calcite and aragonite to the same high pressure phase. Nevertheless, the K/K' values for both polymorphs (at the same E_{TR}, ρ_o conditions) are very similar, and transformation of both polymorphs to the same high pressure phase cannot be discounted. In the Hugoniot temperature calculations described in the following paragraph, the entire range of model isentrope parameters presented in Table 6-4 is considered.

Temperatures along the Hugoniot are determined from:

$$T_H = 298 \exp\left[\int_{\rho_o}^{\rho} \frac{\gamma}{\rho^*} d\rho^*\right] + \frac{E_H - E_S}{C_V} \qquad (6\text{-}8)$$

The first term in this equation is the temperature rise along the high pressure phase isentrope and the second is the temperature difference at some density between this calculated isentrope and the (experimental) Hugoniot. E_S is given by Eq. 6-6, and E_H by the Rankine-Hugoniot conservation equation:

$$E_H - E_0 = 1/2\ (P_0 + P_H)\ (1/\rho_o' - 1/\rho) \qquad (6\text{-}9)$$

where the standard E_0 and P_0 conditions are taken to be equal to 0 and ρ_o' is the initial density of the shocked material. We assume that the heat capacity at constant volume, C_V, is equal to the Dulong-Petit value of 3R, where R is the gas constant. According to experimental heat capacity measurements (Robie et al., 1978), 90% of this Dulong-Petit value is achieved by temperatures of 650 K and 720 K in calcite and aragonite, respectively; thus, our assumption is justified over most of

Table 6-4

$CaCO_3$ HIGH PRESSURE PHASE MODEL ISENTROPE PARAMETERS

		E_{TR} (Joules/g)		
	ρ_o (g/cc)	20	100	200
Aragonite	3.0	77/4.8*	77/5.0	79/4.8
	3.1	98/4.5	98/4.6	98/4.8
Calcite	3.0	79/3.6	79/3.7	75/4.1
	3.1	95/3.5	92/3.8	98/3.4

* Tabulated values represent K(GPa)/K'

the calculated temperature range. Calculated calcite and aragonite Hugoniot temperatures for a range of input parameters are presented in Fig. 6-8. The numbers in parentheses refer to the transition energy, initial density, bulk modulus, and first pressure derivative of the high pressure phase values, respectively, used in the high pressure phase isentrope determinations. The calcite melting curve determined by Irving and Wyllie (1973) is also included in this graph. Any reasonable extrapolation of the melting curve to higher pressures rather decisively speaks against the possibility of melting occurring at $\sim$ 15 GPa and $\sim$ 18 GPa on the calcite and aragonite Hugoniots, respectively.

As noted in the experimental results section, the release adiabats for aragonite indicate a consistent pattern. Release from shock states below $\sim$ 14 GPa occurs along steep paths and suggests densification of up to 10% upon complete release, whereas release from pressures above 16 GPa progresses along unusually shallow paths, suggesting vaporization upon unloading. As discussed in the previous paragraph, theoretical shock temperatures along the aragonite Hugoniot are insufficient to cause melting. In order to investigate the possibility of vaporization upon the release of $CaCO_3$ to ambient pressures, the shock entropy criterion was applied (see e.g. Zel'dovich and Raizier, 1966; Ahrens and O'Keefe, 1972). Briefly, the method compares the entropy value along the release path with the entropy of vaporization at 1 bar. Since release is an isentropic process, the entropy at a release pressure of 1 bar is the same as that of the Hugoniot state. In turn, the entropy along the Hugoniot relative to standard state entropy, ΔS, can be

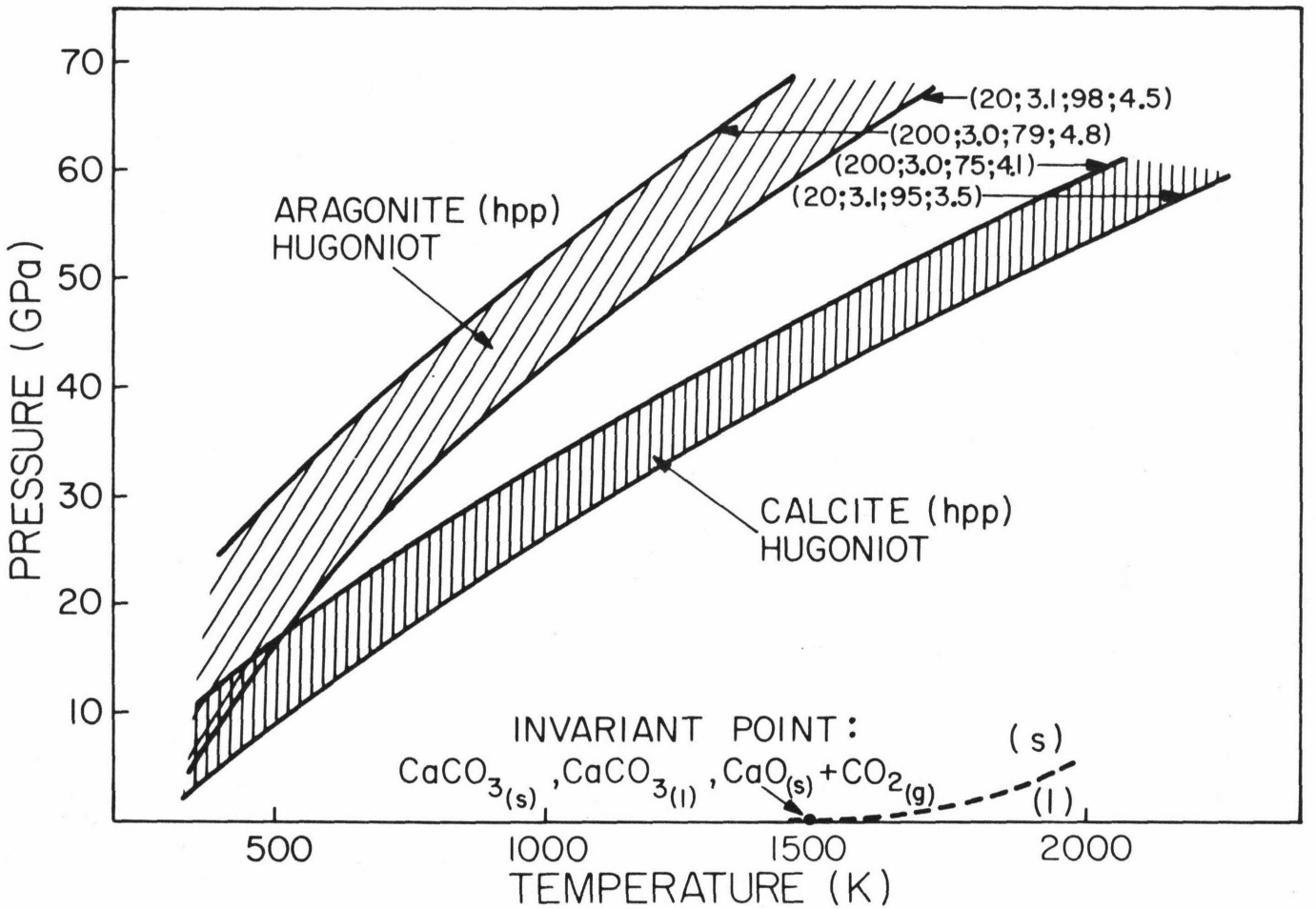

Figure 6-8. Pressure vs. temperature relation along aragonite and calcite Hugoniots. Numbers in parentheses represent (E_{TR}: ρ_o; K; K') values used in model isentrope calculations on which temperature estimates are based; γ was assumed to be of the form: $\gamma = 1.53 \frac{\rho_o}{\rho}^{0.6}$. Calcite melting curve (Irving and Wyllie, 1973) appears in the right of the graph.

determined from the temperature rise between the shock isentrope and the Hugoniot:

$$\Delta S = \int_{T_S}^{T_H} \frac{C_V}{T}\, dT \qquad (6\text{-}10)$$

Determination of incipient and complete vaporization entropies (upon release from pressures above the suspected phase change) requires knowledge of the standard state entropy of the high pressure $CaCO_3$ phase. An estimate of $S^0_{298.15K} = 0.8 \rightarrow 0.83$ joules/g K, corresponding to a high pressure phase ρ_o of $3.1 \rightarrow 3.0$ g/cc, respectively, is based on the systematic relationship, shown in Fig. 6-9, between $S^0_{298.15K}$ and the molar volume of carbonates (Robie et al., 1978). The incipient vaporization criterion involves coincidence of the release state entropy value with the entropy increase achieved in raising a material to its vaporization temperature at 1 bar; according to the experimentally determined vaporization curve (Baker, 1962), vaporization of calcite at 1 bar occurs at 1171 K. Complete vaporization entropy is the sum of the entropy gained in raising the material to its vaporization temperature and the dissociation entropy at that temperature. Calculated post-shock entropies for calcite and aragonite are presented in Fig. 6-10; entropies for complete vaporization, $\Delta S \approx 3$ joules/g K, do not appear to be reached below shock pressures of $\sim$ 100 GPa for either calcite or aragonite. According to this model, then, minimum shock pressures for incipient vaporization are 33 GPa and 55 GPa for calcite and aragonite, respectively. These values are similar to shock pressures required for vaporization as calculated by Kieffer and Simonds (1980) using the waste heat approximation. The agreement adds support to the contention that

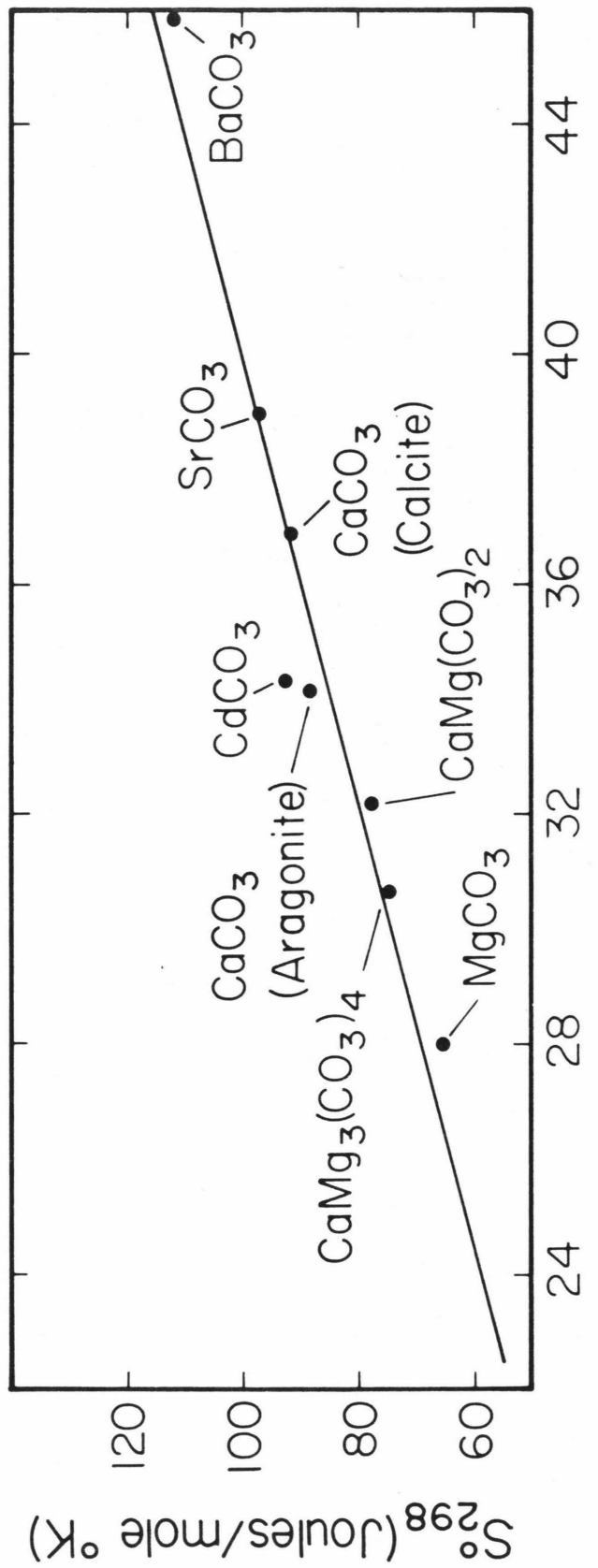

Figure 6-9. Plot showing systematic relationship between standard entropy, $S^{\circ}_{298.15K}$, and molar volume for several carbonate minerals. Used in estimate of $S^{\circ}_{298.15K}$ for speculated high pressure $CaCO_3$ phase.

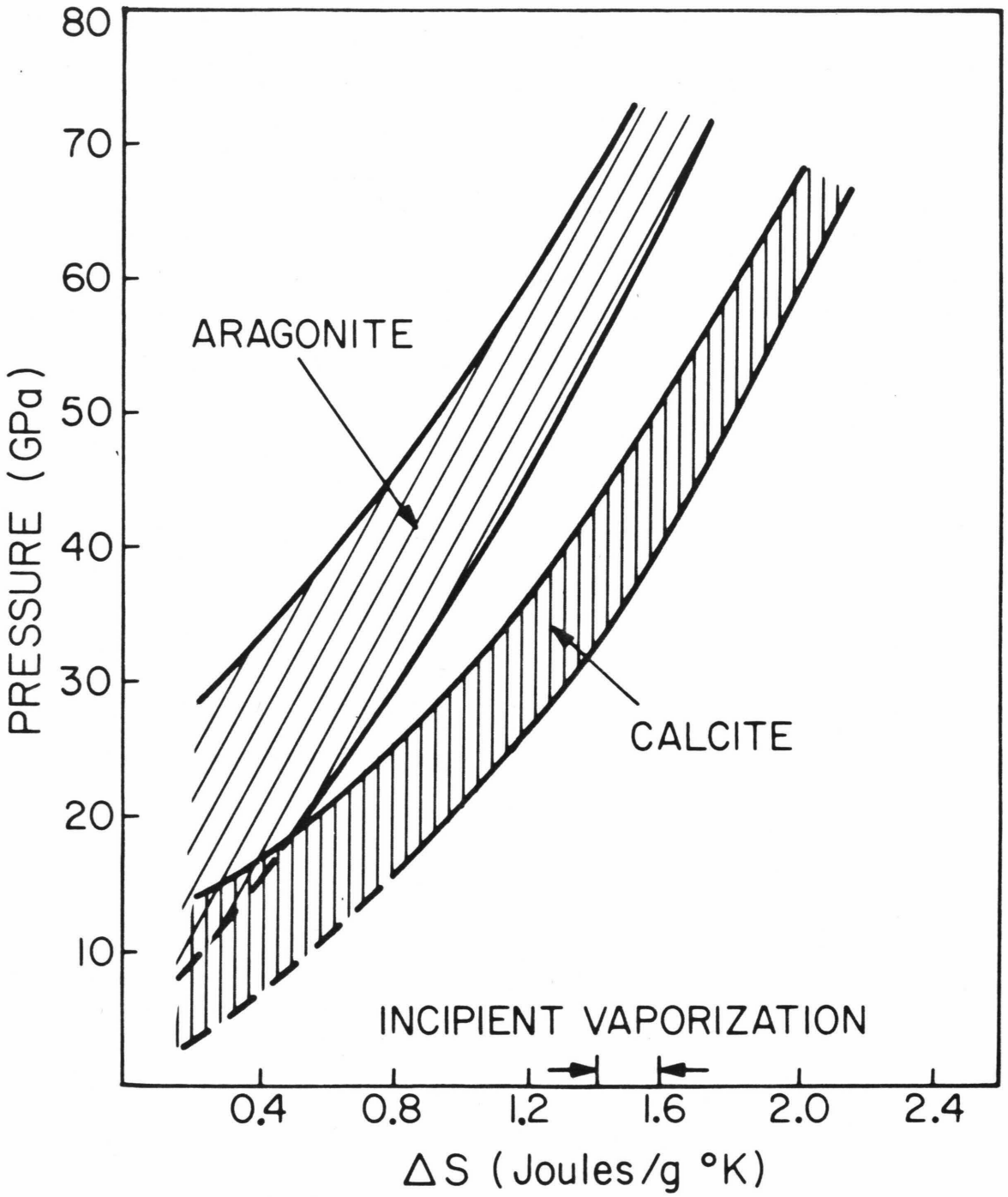

Figure 6-10. Calculated post-shock entropies, relative to standard state entropy, for aragonite and calcite. Parameters used in calculating upper and lower bounds for each phase correspond to the values presented for the top and bottom curves in Fig. 6-8. The entropy for complete vaporization, $\Delta S \approx 3$ Joules/g K, is not achieved at reasonable extrapolations of experimental data.

γ is small.

Thus, although the shock and release state experimental evidence is consistent with the suggested interpretation that shock melting and vaporization upon release characterizes the behavior of carbonates at shock pressures in excess of ~ 16 GPa, theoretical considerations are in pronounced conflict with this interpretation. Possible causes for this discrepancy might be found by considering shock deformational behavior, on the microstructural scale, of brittle, thermally insulating solids. Grady (1980) and Horie (1980) extensively discuss the role of heterogeneous deformation during shock compression. According to these authors, instabilities intrinsic to shock compression processes result in localized regions of intense deformation and extreme temperature gradients which may persist for some time after passage of the shock wave. Thus, even though equilibrium temperature estimates are well below those required for melting, local "hot spot" temperatures may be sufficient to melt material in local shear bands. In fact, such zones of intense local deformation have been observed in shock-recovered materials (see e.g. Jeanloz et al., 1977). Grady (1980) estimates the intensity of local temperature excursions in several minerals including calcite. According to his calculations, a significant fraction of the melting temperature ($T_{local}/T_{melt} > 0.5$) is reached when calcite is shocked to a relatively modest pressure of 4.4 GPa. Although it is difficult to assess the extent to which processes of adiabatic shear and heterogeneous melting influence the Hugoniot results, their effects, at least in a qualitative sense, should be given serious consideration in evaluation of shock compression data.

Summary and Conclusions

The aragonite Hugoniot to 40 GPa can be summarized as follows. The lower portion of the curve is inferred to display a Hugoniot elastic limit between 1.8 and 3.3 GPa and a phase transition, possibly displacive, between 5.5 and 7.6 GPa. Above shock pressures of $\sim$ 10 GPa, the density-pressure curve becomes decidedly shallower and continues in this trend to 40 GPa; the calcite and aragonite Hugoniots in the 10 to 40 GPa range are, within the limits of experimental error, coincident, suggesting the transformation of both polymorphs to a common high pressure phase.

Measured release adiabats for aragonite from shock states below $\sim$ 14 GPa show consistently steep initial unloading paths and final zero-pressure densities up to 10% greater than the initial density. Unloading paths from pressures greater than $\sim$ 16 GPa are unusually shallow, a pattern that is consistent with the interpretation that vaporization occurs upon unloading. Although the experimental results may suggest vaporization upon release from these pressures, theoretical shock temperature and entropy calculations decidedly conflict with this interpretation. Experiments designed to further investigate carbonate, specifically calcite upon decompression are described, and results presented, in the following chapter.

References

Adadurov, G. A., D. B. Balashov, and A. N. Dremin, A study of the volumetric compressibility of marble at high pressures, Bull. Acad. Sci. U.S.S.R., Geophys. Series, No. 5, 463-466, May 1961.

Ahrens, T. J. and V. G. Gregson, Jr., Shock compression of crustal rocks: Data for quartz, calcite, and plagioclase rocks, J. Geophys. Res., 69, 4839-4874, 1964.

Ahrens, T. J., W. H. Gust, and E. B. Royce, Material strength effect in the shock compression of alumina, J. Appl. Phys., 39, 4610-4616, 1968.

Ahrens, T. J., D. L. Anderson and A. E. Ringwood, Equations of state and crystal structures of high-pressure phases of shocked silicates and oxides, Reviews of Geophysics, 7, 667-707, 1969.

Ahrens, T. J., J. H. Lower, and P. L. Lagus, Equation of state of forsterite, J. Geophys. Res., 76, 518-528, 1971.

Ahrens, T. J., J. D. O'Keefe, Shock melting and vaporization of lunar rocks and minerals, The Moon, 4, 214-249, 1972.

Ahrens, T. J., C. F. Petersen, and J. T. Rosenberg, Shock compression of feldspars, J. Geophys. Res., 74, 2727-2746, 1969.

Ahrens, T. J., J. T. Rosenberg, and M. V. Ruderman, Dynamic properties of rocks, Stanford Research Inst. Report DASA 1868, 107-111, 1966.

Baker, E. H., The calcium oxide-carbon dioxide system in the pressure range 1-300 atmospheres, Chem. Soc. J., 464-470, 1962.

Bayuk, Y. I., M. P. Volorovich, and G. A. Yefimova, Ultrasonic studies of phase transitions in calcite at high pressures, Izv. Earth Physics, 8, 59-62, 1974.

Berman, H., A torsion microbalance for the determination of specific gravities of minerals, American Mineralogist, 24, 435-440, 1939.

Booth, M. C., and H. H. Kieffer, Carbonate formation in Marslike environment, J. Geophys. Res., 83, 1809-1815, 1978.

Brar, N. S., and H. H. Schloessin, Mechanisms of calcite I-II-III and calcite ↔ aragonite transitions (abstract), EOS, 61, 379, 1980.

Bridgman, P. W., The high pressure behavior of miscellaneous minerals, Am. J. Sci., 239, 7-18, 1939.

Carter, W. J., Shock wave techniques for the examination of phase transitions, in Phase Transitions-1973 Proceedings of the Conference on Phase Transitions and Their Applications in Materials Science, L. E. Crossi, ed., Pergamon, New York, 223-234, 1973.

Carter, W. J., and S. P. Marsh, Hugoniot equation of state of polymers, Submitted to J. Chem. Phys., 1980.

Crawford, W. A., and W. S. Fyfe, Calcite-Aragonite equilibrium at 100°C, Science, 144, 1569-1570, 1964.

Dasgupta, D. R., The oriented transformation of aragonite into calcite, Min. Mag., 33, 924-928, 1964.

Davis, B. L., X-Ray diffraction data on two high-pressure phases of calcium carbonate, Science, 145, 489-491, 1964.

Davison, L., and R. A. Graham, "Shock compression of solids", Phys. Reports, 55, 255-379, 1979.

Dence, M. R., R.A.F. Grieve, and P. B. Robertson, Terrestrial impact structures: principal characteristics and energy considerations, in Impact and Explosion Cratering, eds. D. J. Roddy, R. O. Pepin and R. B. Merrill, Pergamon Press, pp. 247-275, 1977.

Grady, D. E., Shock deformation of brittle solids, J. Geophys. Res., 85, 913-924, 1980.

Grady, D. E., R. E. Hollenbach, and K. W. Schuler, Compression wave studies on calcite rock, J. Geophys. Res., 83, 1978.

Grady, D. E., W. J. Murri, and G. R. Fowles, Quartz to stishovite: Wave propagation in the mixed phase region, J. Geophys. Res., 79, 332-338, 1974.

Horie, Y., Thermodynamics of dislocations and shock compression of solids, Phys. Rev., 21, 5549-5557, 1980.

Huang, W. L., and P. J. Wyllie, Melting relationships in the systems $CaO-CO_2$ and $MgO-CO_2$ to 33 kilobars, Geochimica et Cosmochimica Acta, 40, 129-132, 1976.

Irving, A. J., and P. J. Wyllie, Melting relationships in $CaO-CO_2$, EPSL, 20, 220-225, 1973.

Jackson, I., and T. J. Ahrens, Shock wave compression of single-crystal forsterite, J. Geophys. Res., 84, 3039-3048, 1979.

Jamieson, J. C., Phase equilibrium in the system calcite-aragonite, J. Chem. Phys., 21, 1385-1390, 1953.

Jamieson, J. C., Introductory studies of high-pressure polymorphism to 24,000 bars by X-ray diffraction with some comments on calcite II, J. Geol., 65, 334-342, 1957.

Jamieson, J. C., and J. R. Goldsmith, Some reactions produced in carbonates by grinding, Am. Mineralogist, 45, 818-827, 1960.

Jeanloz, R., T. J. Ahrens, J. S. Lally, G. L. Nord, Jr., J. M. Christie, and A. H. Heuer, Shock-produced olivine glass: First observation, Science, 197, 457-459, 1977.

Kalashnikov, N. G., M. N. Pavlovskiy, G. V. Simakov, and R. F. Trunin, Dynamic compressibility of calcite-group minerals, Izv. Earth Phys., 2, 23-29, 1973.

Kieffer, S. W., and C. H. Simonds, The role of volatiles in the impact cratering process, Rev. Geophys. and Space Phys., 18, 143-181, 1980.

Lander, J. J., Polymorphism and anion rotational disorder in the alkaline earth carbonates, J. Chem. Phys., 17, 892-901, 1949.

Leiserowitz, L., and G.M.J. Schmidt, Shock-induced irreversible phase transitions in inorganic solids, J. Phys. Chem. Solids, 27, 1453-1457, 1966.

Lewis, J. S., Venus: atmospheric and lithospheric composition, EPSL, 10, 73-80, 1970.

Lyzenga, G., and T. J. Ahrens, The relation between the shock-induced free surface velocity and the post-shock specific volume of solids, J. Appl. Phys., 49, 200-213, 1978.

MacDonald, G.J.T., Experimental determination of calcite-aragonite equilibrium relations at elevated temperatures and pressure, Am. Mineralogist, 41, 744-756, 1956.

McQueen, R. G., S. P. Marsh, and J. N. Fritz, Hugoniot equation of state of twelve rocks, J. Geophys. Res., 72, 4999-5036, 1967.

McQueen, R. G., S. P. Marsh, J. W. Taylor, J. N. Fritz, and W. J. Carter, The equation of state of solids from shock wave studies, in High-Velocity Impact Phenomena ed. R. Kinslow, pp. 293-417, Academic Press, New York, 1970.

Merrill, L., and W. A. Bassett, The crystal structure of $CaCO_3$(II), a high-pressure metastable phase of calcium carbonate, Acta. Cryst., B31, 343-349, 1975.

Rice, M. H., R. G. McQueen, and J. M. Walsh, Compression of solids by strong shock waves, in Solid State Physics, 6, eds. F. Seitz and D. Turnbull, pp. 1-63, Academic Press, New York, 1958.

Robie, R. R., B. S. Hemingway, and J. R. Fisher, Thermodynamic properties of minerals and related substances at 298.15K and 1 bar (10^5 pascals) pressure and at higher temperatures, Geol. Survey Bull. 1952, 298-310, 1978.

Siegel, L. A., Molecular rotation in sodium cyanide and sodium nitrate, J. Chem. Phys., 17, 1146-1150, 1949.

Singh, A. K., and G. C. Kennedy, Compression of calcite to 40 kbar, J. Geophys. Res., 79, 2615-2622, 1974.

van Thiel, M., J. Shaner, and E. Salinas, Report UCRL 50108, Vol. 3, Lawrence Livermore Laboratory, 1977.

Voigt, W., Lehrbuch der Kristallphysik, B. A. Teubner, Leipzig, pp. 410-431, 1910.

Walsh, J. M., and R. H. Christian, Equation of state of metals from shock wave measurements, Phys. Rev., 97, 1544-1556, 1955.

Zel'dovich, Y. B. and Y. P. Raizer, Physics of Shock Waves and High-Temperature Hydrodynamic Phenomena, vol. II, 766-770, Academic Press, New York, 1967.

Chapter 7

SHOCK-INDUCED VAPORIZATION OF CALCITE

Introduction

The determination of shock pressures, and consequently, meteorite impact velocities, required to induce vaporization of carbonates is important for cratering mechanics studies and atmospheric evolution models. The experimental release adiabat results described in Chapter 6 suggest that vaporization occurs upon unloading of aragonite from Hugoniot pressures as low as 18 GPa. However, according to theoretical calculations (presented in the same chapter) prescribing the entropy increase along both aragonite and calcite Hugoniots, incipient vaporization should only occur upon unloading from minimum pressures of 55 and 33 GPa for aragonite and calcite, respectively. In an attempt to resolve this discrepancy, the release behaviour of calcite is experimentally investigated in this study.

Results from two equation of state experiments on single crystal calcite are presented in this chapter. Calcite was chosen because it is more abundant, relative to aragonite, in terrestrial rocks (Strahler, 1971), and because, according to theoretical predictions, it should vaporize upon decompression from lower pressures than calcite (see Fig. 6-9). In addition, observation of shallow release paths for calcite as well as aragonite would be the first step in generalizing the release vaporization phenomenon for carbonate materials.

An expanded version of the release adiabat measurement technique used in the previous chapter was employed in the two experiments reported here. In Chapter 6, aragonite partial release states (in the $P-u_p$ plane) were determined by measuring shock velocities in lexan buffer mirrors and then applying the impedance match procedure (Rice et al., 1958). Using buffer materials of different shock impedances, it is possible to determine release states at several pressures along the sample decompression path. Figure 7-1 illustrates the pressure-particle velocity states determined along a hypothetical release path; the four Hugoniots, other than calcite, sketched in this graph, represent actual Hugoniot data for the various buffer materials used in these release adiabat experiments. Ahrens et al. (1969) used this varying impedance buffer technique to successfully determine the release adiabats of feldspars.

Experimental details

Clear, colorless calcite crystals, variety Iceland spar, with no observable internal fractures, were used in this study. Two samples were cut into rectangles approximately 17 mm long, 14 mm wide and 3 mm thick, and lapped to within 4 to 10 microns uniform thickness. Archimedean densities, determined using reagent grade toluene and the temperature corrections of Berman (1939), were 2.708 g/cc and 2.709 g/cc; individual measurements varied less than $\pm$0.002 g/cc. These densities are within 0.07% of the calcite X-ray density of 2.710 g/cc.

The samples were then mounted on tungsten driver plates so that the lapped surfaces, coincident with the (104) cleavage plane (determined using crystal morphology), would be perpendicular to the gun barrel axis, hence, the shock propopation direction. Two lexan

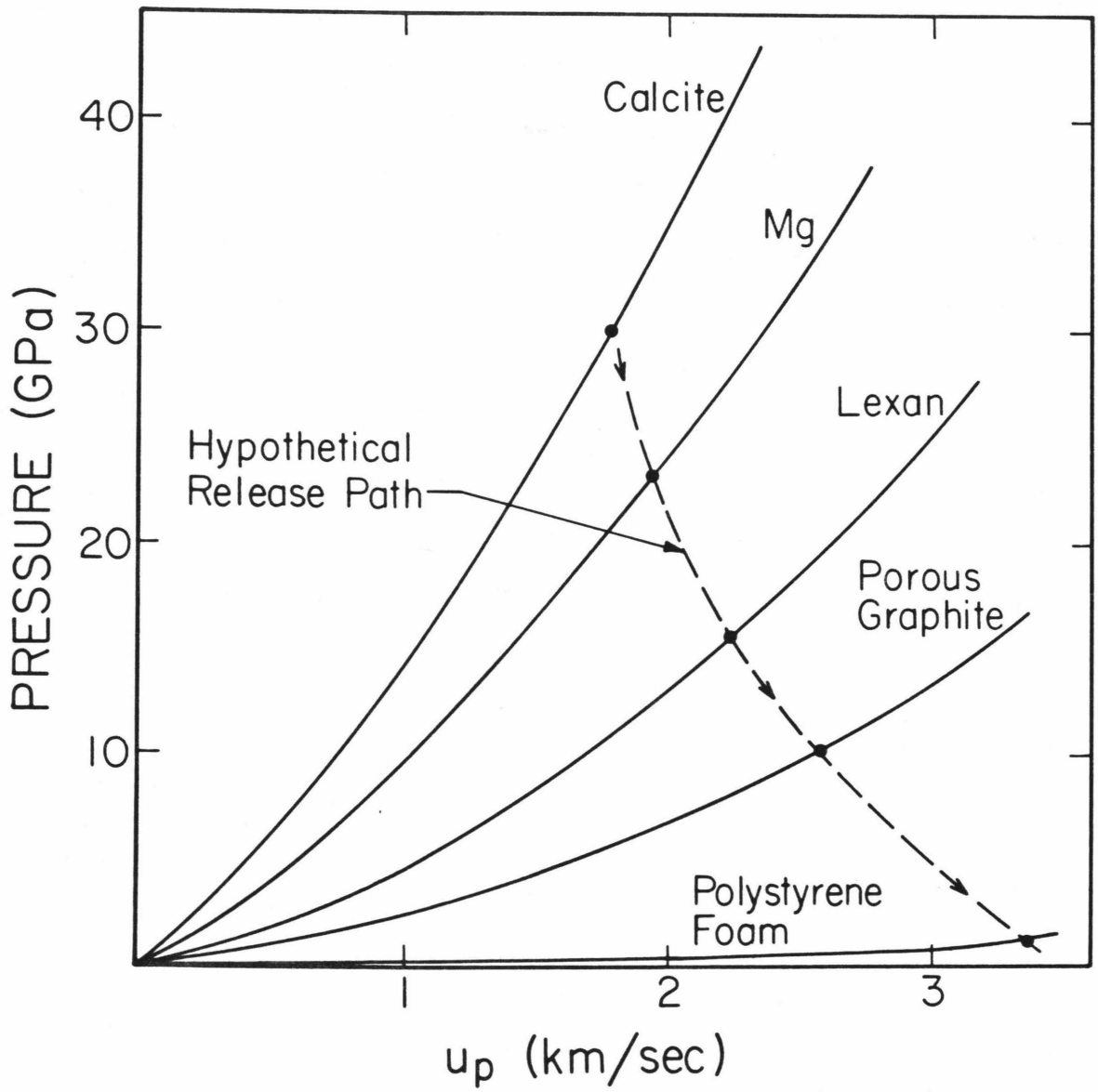

Figure 7-1. Hugoniots of calcite (polycrystalline) and the four buffer materials used in release adiabat experiments; porous graphite and polystyrene foam densities are 1.08 g/cc and 0.055 g/cc, respectively. Dashed line represents possible decompression path.

arrival mirrors were also placed on the driver plate on either side of the calcite sample. An array of 3 different buffer mirrors were then mounted on the calcite crystal. The entire experimental assembly is sketched in Fig. 7-2.

A total of 4 different buffer materials was used in the two experiments: magnesium (AZ31B alloy), lexan, porous graphite (ρ_0=1.08 g/cc), and polystyrene foam (ρ_0=0.055 g/cc). Hugoniots of these materials are shown in Fig. 7-1. Measured densities and the Hugoniot parameter fits are given in Table 7-1; magnesium and lexan density values are Archimedean, and polystyrene foam and porous graphite are bulk densities.

The shock experiments and data analyses were performed as described in Chapter 6. The free surface velocity method, however, is not applicable to the calcite release adiabat experiments because no inclined mirrors were used. Fig. 7-3 shows a characteristic streak record; shock arrivals at various surfaces are indicated on the photograph.

Results

Experimental results for calcite Hugoniot and partial release states, calculated using all buffer material data, are presented in Table 7-2. As discussed in the next section, some of the buffer data, specifically those values calculated using side mounted buffer mirrors, are unreliable; therefore, in the particle velocity-pressure (u_p-P) graph (Fig. 7-4), only center mounted lexan and porous graphite buffer data are plotted. The polystyrene foam values on this graph correspond to treatment (1) in Table 7-2; the two different treatments of the polystyrene foam data, and reasons for preferring

Table 7-1

SUMMARY OF BUFFER MATERIAL HUGONIOT DATA

Buffer	Data Source	ρ_o(g/cc)	c_o(km/sec)	s
Magnesium	Kinslow (1970)	1.78 g/cc ±0.03	4.522	1.242
Lexan	Carter and Marsh (1980)	1.196 g/cc ±	2.33	1.57
(a) Porous Graphite	Marsh (1980)	1.081 g/cc ±0.007	0.79	1.30
(b) Polystyrene Foam	Marsh (1980)	0.056 g/cc ±0.002	0.243	1.118

(a) Obtained from Union Carbide Co., Chicago, IL

(b) Obtained from Tempo Plastic Co., Burbank, CA

Table 7-2

SUMMARY OF HUGONIOT AND RELEASE MEASUREMENTS

Shot	Flyer/Driver Material	Projectile Velocity, km/sec	Initial Sample Density, g/cc	Hugoniot State: Shock Velocity, km/sec	Hugoniot State: Particle Velocity, km/sec	Hugoniot State: Pressure, GPa	Hugoniot State: Density, g/cc	Partial Release States: Buffer Material	Buffer Shock Velocity, km/sec	Particle Velocity, km/sec	Pressure, GPa	Density, g/cc
514	W	2.41 ±0.01	2.709 ±0.002	6.49 ±0.04	2.00 ±0.01	35.23 ±0.25	3.92 ±0.02	Mg (AZ31B)	7.34 ±0.13	2.27 ±0.11	29.63 ±1.94	3.73 ±0.20
								Lexan	6.80 ±0.13	2.85 ±0.08	23.13 ±1.10	3.18 ±0.17
								(1) Polystyrene Foam	6.06 ±0.05	5.20 ±0.04	1.73 ±0.03	1.78 ±0.03
								(2) Polystyrene Foam	4.27 ±0.27	3.61 ±0.24	0.85 ±0.11	3.03 ±0.21
522	W	2.45 ±0.01	2.708 ±0.001	7.05 ±0.12	2.01 ±0.01	38.40 ±0.59	3.79 ±0.03	Lexan	5.69 ±0.15	2.14 ±0.09	14.58 ±1.01	3.78 ±0.04
								Porous Graphite	5.47 ±0.10	3.60 ±0.08	19.92 ±0.79	2.50 ±0.12
								(1) Polystyrene Foam	6.38 ±0.10	5.49 ±0.09	1.93 ±0.06	1.68 ±0.05
								(2) Polystyrene Foam	3.92 ±0.09	3.29 ±0.09	0.71 ±0.04	3.25 ±0.07

(1) Buffer shock velocity calculated using onset point of inward sloping on the foam buffer streak image. (See Fig. 7-3)

(2) Buffer shock velocity calculated using flattest cut-off segment of foam buffer streak image. (See Fig. 7-3)

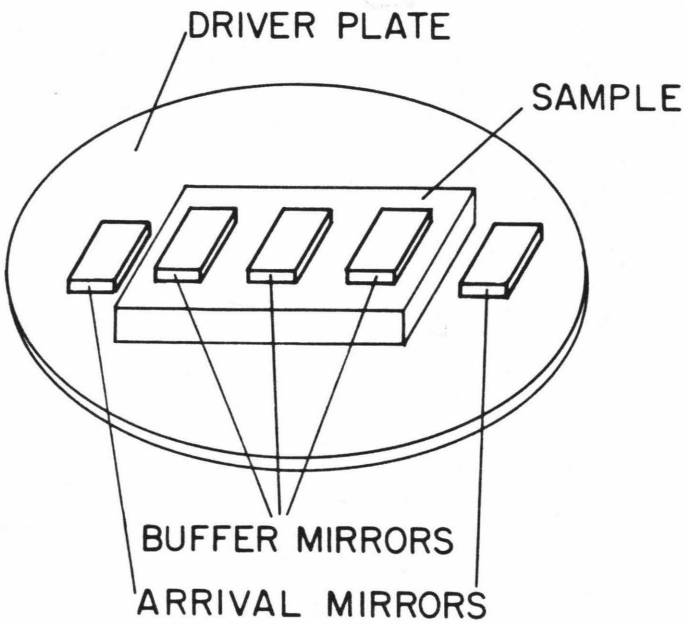

Figure 7-2. Sketch of calcite release adiabat experimental assembly. Buffer mirrors are either lexan, magnesium, porous graphite or polystyrene foam.

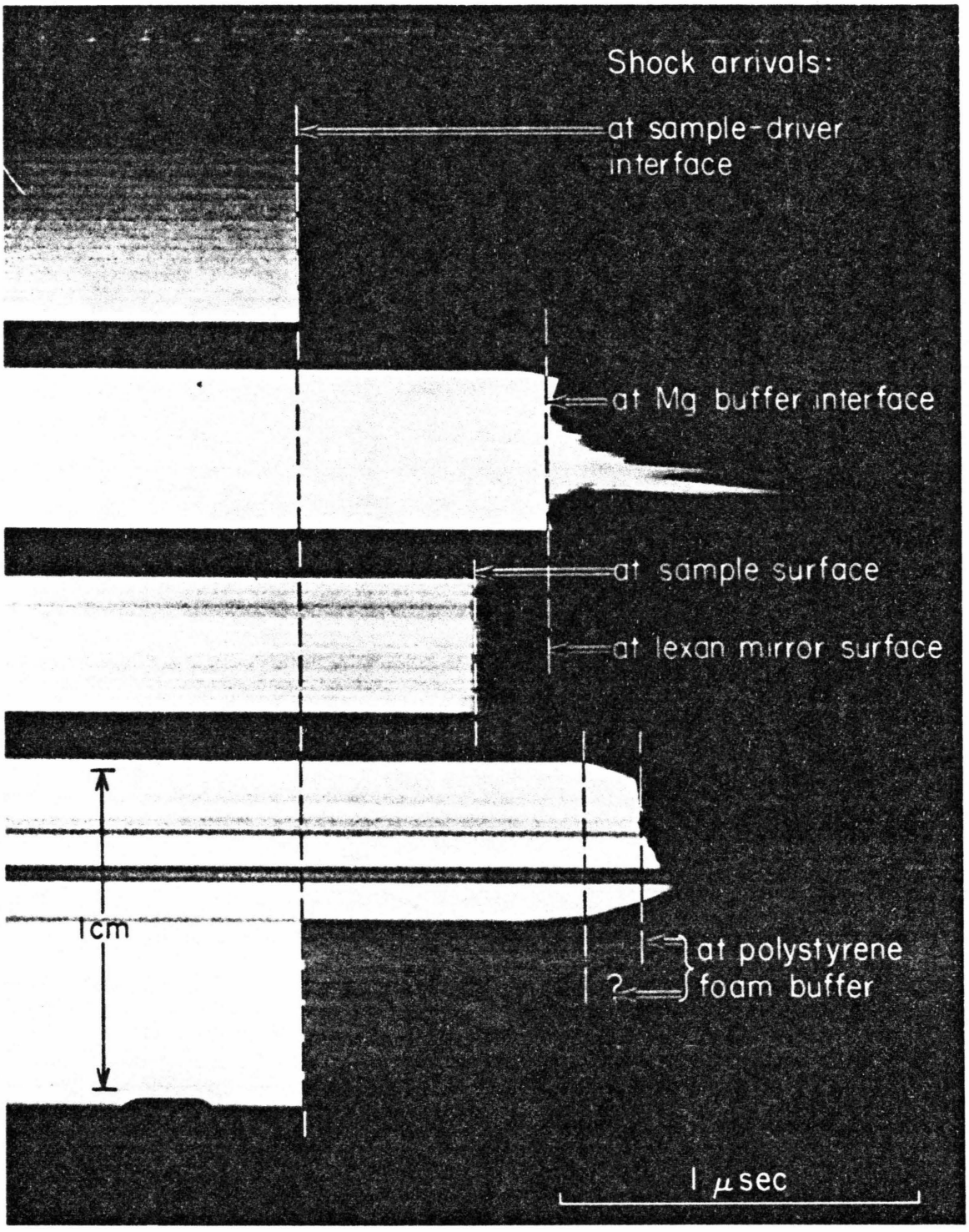

Figure 7-3. Streak image of shot 514 demonstrating shock wave arrivals at sample and buffer mirror surfaces. Polystyrene foam buffer arrival marked "?" corresponds to interpretation (1) in Table 7-2 and text; later foam arrival corresponds to interpretation (2).

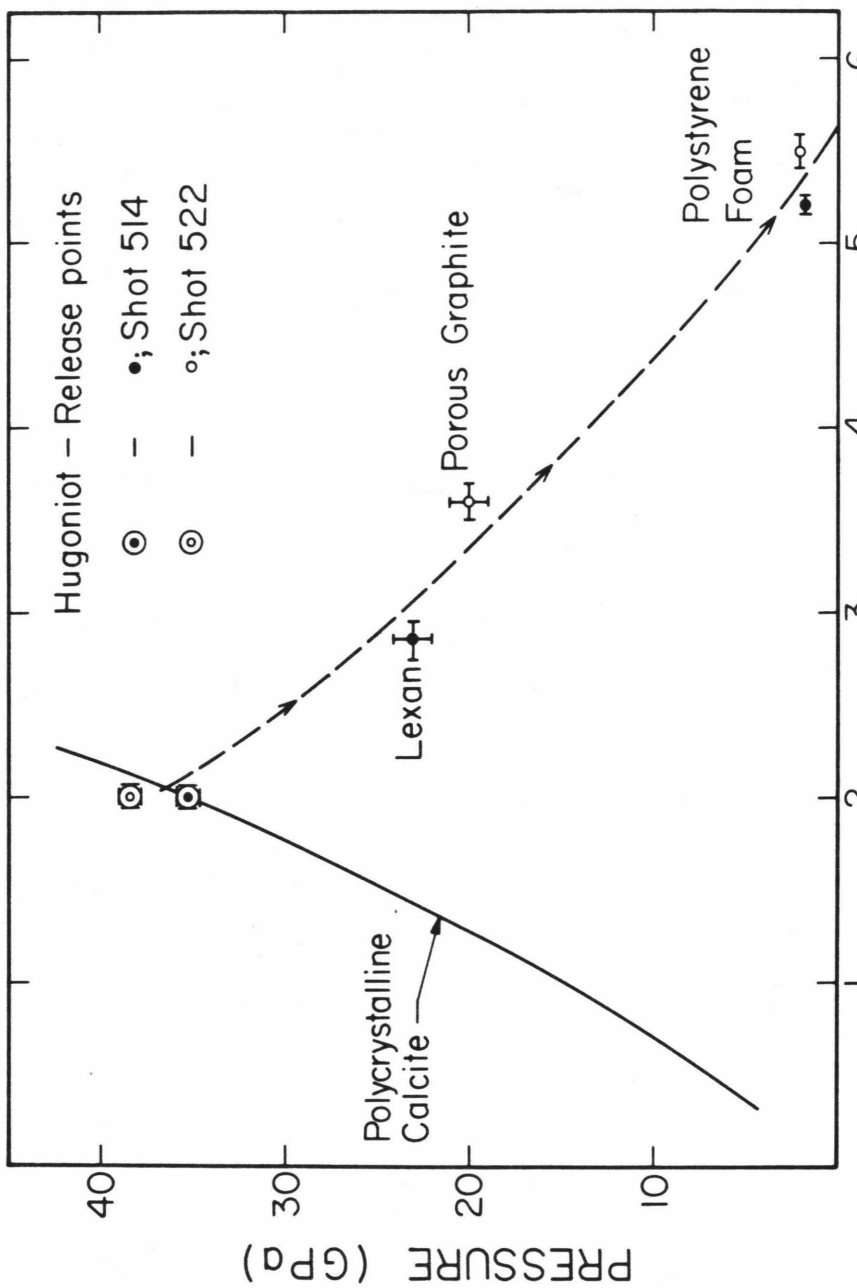

Figure 7-4. Calcite Hugoniot and release data in the (u_p-P) plane. Polystyrene foam partial release states correspond to treatment (1) (see Fig. 7-3 and text).

treatment (1), are discussed in the next section.

In Fig.7-4, note, first of all, the agreement between the two experimental Hugoniot states and the polycrystalline calcite Hugoniot determined by Adadurov et al. (1961). (These points are also consistent with the single crystal calcite Hugoniot of Ahrens and Gregson (1964), to be shown in a later diagram.) Shock pressures achieved in the two experiments are close enough (35.2 and 38.4 GPa), so that very similar release paths are expected, and a single release curve (dashed) is shown in Fig. 7-4.

Hugoniot and partial release states (for the same buffer mirror data used in Fig. 7-4) are presented in a density-pressure (ρ-P) diagram in Fig. 7-5; the densities for the partial release states were calculated using the Riemann integral formulation (Rice et al., 1958). In addition, single and polycrystalline calcite (Ahrens and Gregson, 1964; Adadurov et al., 1961) and CaO (Jeanloz and Ahrens, 1980), Hugoniots are included in this figure. Interpretations of the shallow release adiabats shown in this figure will be presented in the discussion section.

Evaluation of Buffer Mirror Results

In this section, release data for all buffer mirrors is critically assessed and criteria for release adiabat reliability are determined.

All of the partial release adiabat states determined in the two calcite experiments are listed in Table 7-2. This entire set of release data shows not only extreme overall scatter, but inconsistent partial release states determined in the same experiment. The lexan and porous graphite data from shot 522, for example, indicate a highly

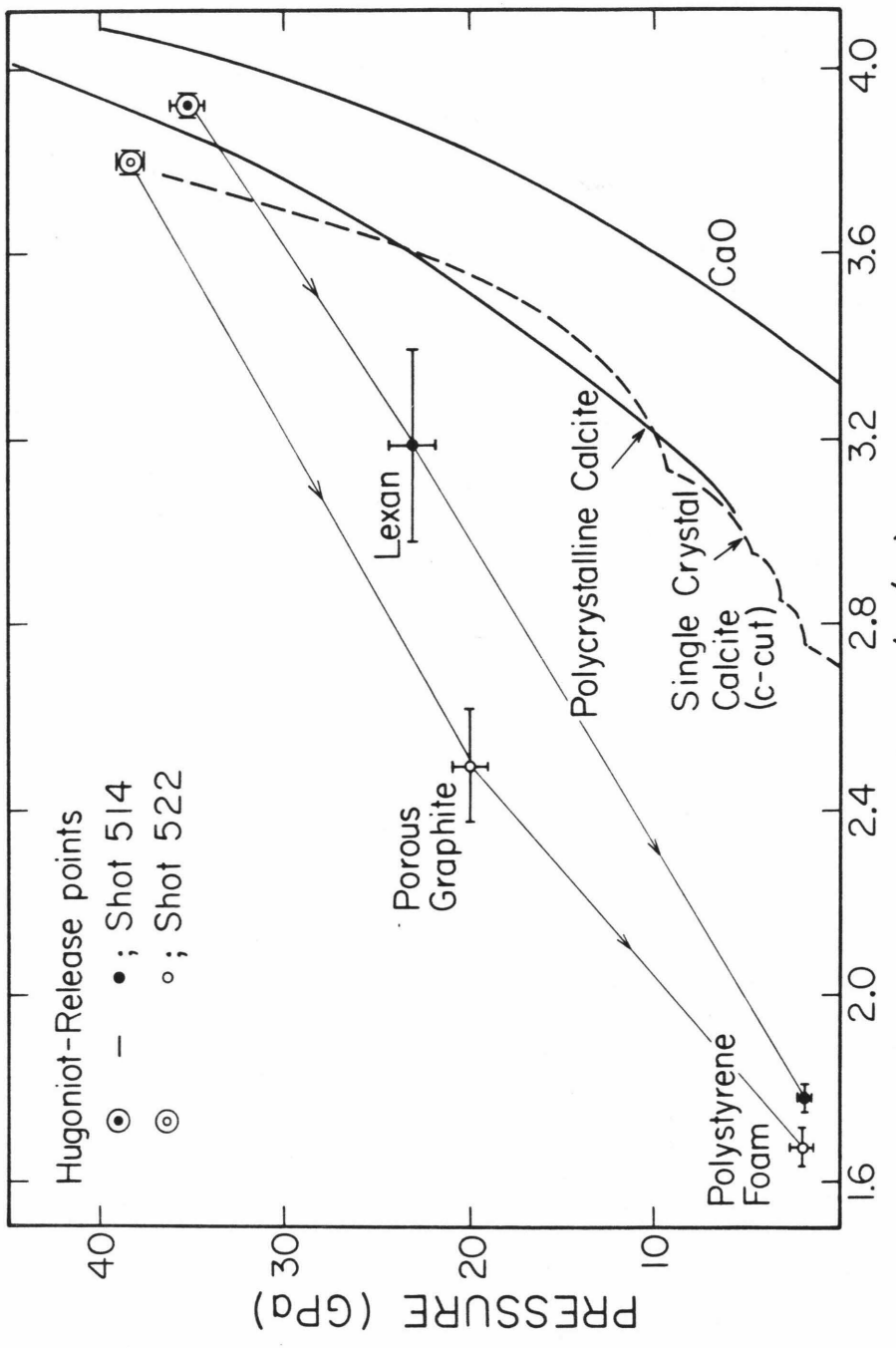

Figure 7-5. Density-pressure plot of calcite Hugoniot and partial release data. Single and polycrystalline calcite Hugoniots are also plotted. Polystyrene foam data corresponds to treatment (1).

improbable release path of a particle velocity increase upon decompression to 20 GPa, followed by a sudden decrease between 20 and 15 GPa. The corresponding density behaviour upon decompression is a density decrease from the Hugoniot pressure to 20 GPa and an abrupt increase, to densities only slightly lower than at the Hugoniot state, between 20 and 15 GPa. The magnesium and lexan release points for shot 514 appear consistent; however, the magnesium datum is at a pressure very close to that of the calcite Hugoniot datum and any incongruity here would probably not be observable.

It is proposed that the partial release adiabat data are dependent on the position of the buffer mirror on the sample. More specifically, it is suggested that the inconsistencies in the partial release states from the two calcite experiments are due to the attenuation of the shock wave entering the buffer material, which, in turn, is caused by sample and buffer related edge effects. A sufficiently attenuated shock wave would not extinguish the reflectivity at the buffer surface. Instead, the observed streak record cut-off may represent the arrival of some later wave (or several superimposed waves). A convincing line of evidence for this argument is the consistency of release data from the lexan and porous graphite buffers in shots 514 and 522, respectively; both these buffers were placed in the center of the sample (see Fig. 7-2) and would have been the least likely to experience any edge attenuation effects.

Considering the polystyrene foam data, a puzzling, but distinctive, streak record was observed for both shots. In Fig. 7-3, the record for shot 514, an inward sloping of the polystyrene foam

buffer streak image (indicated by question mark), followed by a semi-flat cut-off is observed. A similar pattern was observed in the record from shot 522. In addition, the same features were noted in the streak record from a Hugoniot equation of state experiment on the polystyrene foam. In that test, a piece of mylar-covered polystyrene foam was placed directly on, and near the edge of, a tungsten driver plate. The foam Hugoniot density calculated using a shock velocity defined by the semi-flat cut-off (analagous to the later foam arrival indicated in Fig. 7-3) in this equation of state experiment, had a negative value. On the other hand, the Hugoniot state calculated using a shock velocity determined from the streak image slope break (analagous to the point indicated with the question mark in Fig. 7-3) was entirely consistent with the known polystyrene foam Hugoniot. Partial release states for the calcite experiments were calculated using both the slope break and semi-flat cut-off interpretions, indicated as (1) and (2), respectively, in Table 7-2. The polystyrene foam partial release states determined according to interpretation (1) are consistent with shot 514 lexan and shot 522 porous graphite (both center mounted buffers) results. Thus, it is concluded that the appropriate treatment of the polystyrene foam data is according to interpretation (1), and that, in general, reliable partial release data can only be obtained from buffer mirrors mounted in the center of the sample.

Discussion and Conclusions

The shallow release paths drawn in Fig. 7-5 indicate a drastic reduction in the density of calcite upon decompression from shock pressures of approximately 37 GPa. According to polystyrene foam

partial release states, the density of $CaCO_3$ at 0.2 GPa along the release adiabat is 36% lower than the starting material density of 2.71 g/cc. Such a severe decrease in density strongly suggests that dissociation, i.e., release of CO_2, occurs during the decompression process.

In order to estimate the mass fraction of decomposed $CaCO_3$, a mass balance calculation can be performed, using isentropes of the components CO_2, CaO and $CaCO_3$ present during release. An analagous study by Grady et al. (1974) used experimental and calculated release adiabats to investigate the alpha quartz-stishovite mixed phase region. In the very approximate calculation presented here, the CO_2 isotherm and calcite and CaO shock compression curves (rather than isentropes) are used. The single crystal calcite and CaO Hugoniots are from Ahrens and Gregson (1964) and Ahrens and Jeanloz (1980), respectively. The CO_2 isotherm was calculated, using experimental P-V-T data of Shmonov and Shmulovich (1974), for a temperature of 1250 K, The average calculated calcite Hugoniot temperature at a shock pressure of 37 GPa (see Fig. 6-8). The 1250 K isotherm represents maximum possible temperatures upon release, and the dissociated mass fraction calculated using this isotherm, should, therefore, be a minimum estimate. This constraint, however, is modified by the offset, toward lower densities of the isentrope from the isotherm. Since the isotherm best approximates the isentrope at low pressures, the mass balance calculation is performed at 0.2 GPa.

In Fig. 7-6, a log density-log pressure graph, the 1250 K CO_2 isotherm and the $CaCO_3$ and CaO Hugoniots, together with the calcite release adiabat data presented in this chapter, are shown. The

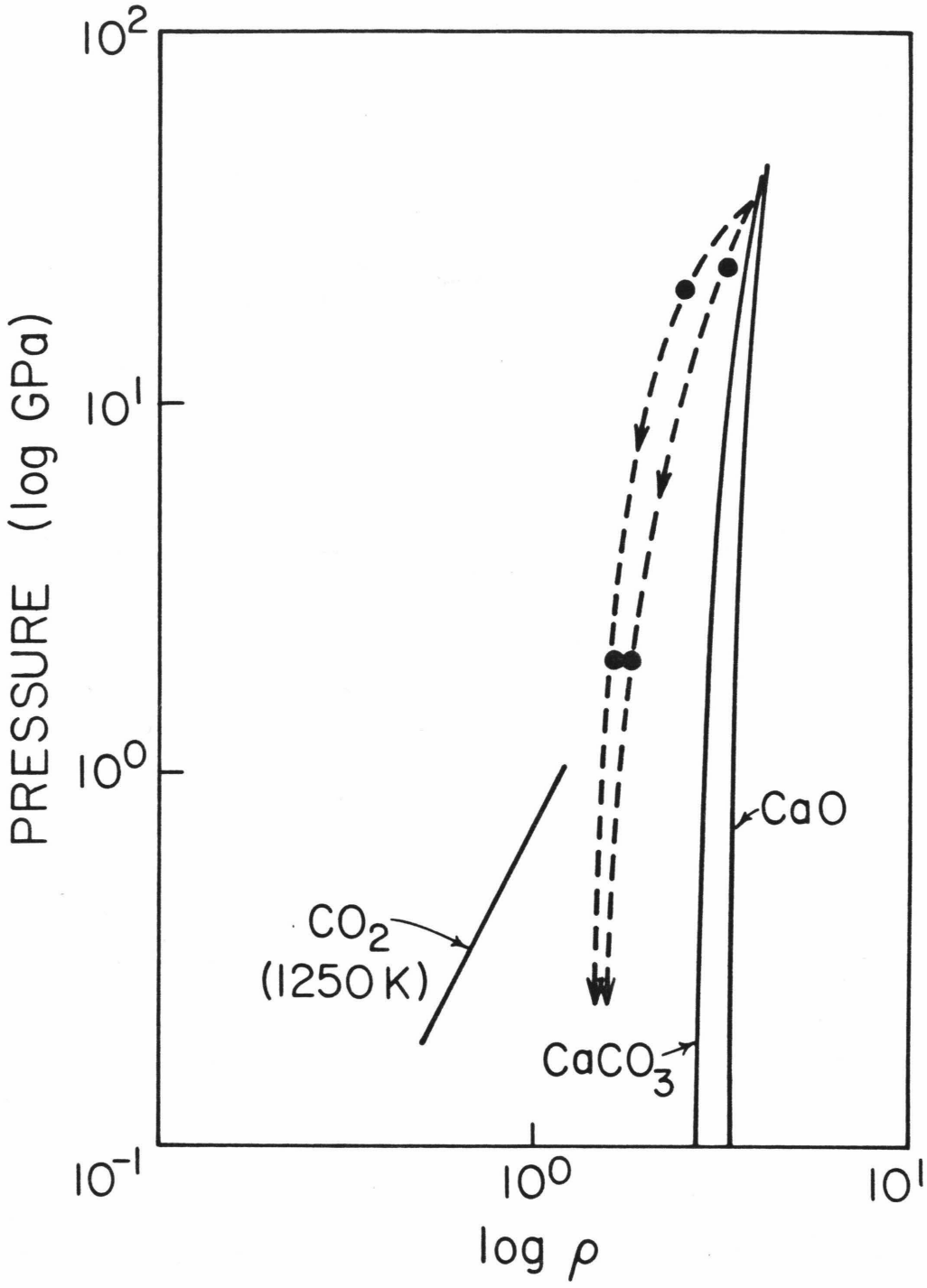

Figure 7-6. Log density-log pressure plot of CaO and calcite (single crystal) Hugoniots and 1250 K CO_2 isotherm. Points represent partial release states (see Table 7-2) and dashed lines are extrapolated decompression curves. Used in mass balance calculation to determine fraction of $CaCO_3$ dissociated upon decompression to 0.2 GPa.

decompression curves are extrapolated to 0.2 GPa. At 0.2 GPa, the densities of the various components according to the compression and release curves in Fig. 7-6 are: CO_2=0.53 g/cc, $CaCO_3$=2.75 g/cc, CaO=3.3 g/cc, and mixture-on-release (average of two curves)=1.55 g/cc. Using these densities and the mass balance equation,

$$\frac{1}{\rho_{mix}} = x\left(\frac{0.44}{\rho_{CO_2}} + \frac{0.56}{\rho_{CaO}}\right) + (1 - x)\left(\frac{1}{\rho_{CaCO_3}}\right) \qquad (7\text{-}1)$$

a value of 0.45 is calculated for x, the mass fraction of $CaCO_3$ that is dissociated at 0.2 GPa along the release adiabat. If 45% of the $CaCO_3$ dissociates upon release from Hugoniot pressures of approxiately 37 GPa, incipient vaporization is likely to occur at significantly lower pressures.

These calcite results and interpretations, therefore, are entirely consistent with the aragonite data presented in Chapter 6, which suggest vaporization occurring upon decompression from pressures as low as 18 GPa. In addition, they agree with calcite solid/vapor recovery experiments (Boslough et al., 1981) in which small quantities (approximately 0.02 sample wt %) of CO_2 vapor, presumably given off by the samples, were measured from calcite shocked to 18 GPa. Release of CO_2 vapor at these low pressures might also explain why conventional solid recovery experiments have been unsuccessful above pressures of approximately 10 GPa. Finally, shock-induced vaporization of carbonates at these relatively low (<40 GPa) pressures would significantly affect cratering mechanics in carbonate targets, accounting for observed differences between crater morphologies in silicate and carbonate terrains.

References

Adadurov, G. A., D. B. Balashov, and A. N. Dremin, A study of the volumetric compressibility of marble at high pressures, Bull. Acad. Sci. U.S.S.R., Geophys. Series, no. 5, 463-466, 1961.

Ahrens, T. J. and V. G. Gregson Jr., Shock compression of crustal rocks: data for quartz, calcite, and plagioclase rocks, J. Geophys. Res., 69, 4839-4874, 1964.

Ahrens, T. J., C. F. Petersen, and J. T. Rosenberg, Shock compression of feldspars, J. Geophys. Res., 74, 2727-2746, 1969.

Berman, H., A torsion microbalance for the determination of specific gravities of minerals, Am. Min., 24, 435-440, 1939.

Boslough, M. B., J. Vizgirda, and T. J. Ahrens, Shock-release of vapor from calcite (abstract) Lunar and Planetary Science XII, 104-105, 1981.

Carter, W. J. and S. P. Marsh, Hugoniot equation of state of polymers, submitted to J. of Chem. Physics, 1980.

Grady, D. E., W. J. Murri, and G. R. Fowles, Quartz to stishovite: Wave propagation in the mixed phase region, J. Geophys. Res., 79, 332-338, 1974.

Jeanloz, R. and T. J. Ahrens, Equations of state of FeO and CaO, Geophys. J. R. Astr. Soc., 62, 505-528, 1980.

Kinslow, R. ed., High-Velocity Impact Phenomena, Academic Press, New York, 1970.

Marsh, S. P. ed., LASL Shock Hugoniot Data, U. of California Press, Berkeley, 1980.

Rice, M. H., R. G. McQueen, and J. M. Walsh, Compression of solids by strong shock waves, in Solid State Physics, vol. 6 (F. Seitz and D. Turnbull, eds.), pp. 1-63, Academic Press, New York, 1958.

Shmonov, V. M. and K. I. Shmulovich, Molal volumes and equation of state of CO_2 at temperatures from 100 to 1000°C and pressures from 2000 to 10,000 bars, Doklady Akad. Nauk USSR, 217, 206-209, 1974.

APPENDIX I

ELECTRON SPIN RESONANCE EXPERIMENTS AND THE ESR SPECTRUM OF Mn^{2+} IN CALCITE

The electron spin resonance, or ESR, technique, used in this study to detect low levels of shock deformation in calcite (Chapter 3), is briefly introduced in this appendix. In addition, details of the ESR experiments and the calcite Mn^{2+} signal are presented. For a thorough treatment of the subject, the reader is referred to Abragam and Bleaney (1970).

The ESR spectroscopic method is able to detect very low concentrations of unpaired electrons and to characterize their energy states. In an ESR experiment, a strong, homogeneous magnetic field is applied across a sample producing alignment of unpaired electron spins either parallel or antiparallel to the magnetic field direction; thus, two groups of unpaired electrons with an energy splitting between them are produced. Simultaneously, microwave frequency radiation is directed onto the sample. If the quantum of energy, $h\nu$, associated with a microwave frequency, ν, equals the energy difference between the two electron groups, this energy will be absorbed by electrons in the lower energy states (i.e., with parallel aligned spins). This resonance condition is expressed as:

$$h\nu = g\beta H \qquad \text{(I-1)}$$

where h is Planck's constant, g is the electron g-value, β is the

electronic Bohr magneton, and H is the applied magnetic field. These electrons will then be excited to the higher energy state, reversing their spins in the process. The energy, or frequency, of absorption is very sensitive to the microenvironment of the free electron; for example, a slight distortion in the surrounding crystal lattice would result in absorption at a frequency shifted from that in the undistorted case.

A diagram of an ESR spectrometer is shown in Fig. I-1. Pertinent features of the instrument include the klystron microwave source, two magnets, and a detector that monitors drops, due to microwave absorption by the sample, in the received power level.

In principle, it is possible to detect absorption energies of different unpaired electrons in a sample by either varying the frequency and holding the magnetic field strength constant or varying the field and holding the frequency constant, according to the resonance condition in Eq. I-1. The latter option is, in practice, the more viable one. Thus, typical ESR spectra record absorption intensity versus magnetic field strength. Fig. I-2 shows the raw absorption, first and second derivative, and phase inverted second derivative powder spectra of Mn^{2+} in calcite (single crystal, variety Iceland spar). Pertinent features of this spectra (the phase inverted second derivative version) are discussed in Chapter 3 and diagrammed in Fig. 3-4.

The ESR spectrum of Mn^{2+} in calcite, first examined by Hurd *et al.* (1954), can be explained in detail in terms of Mn^{2+} occupying Ca^{2+} sites in an axially symmetric crystal field. The effect of an external magnetic field on the energy levels of Mn^{2+} in calcite can be described by the spin Hamiltonian (Hurd *et al.*, 1954):

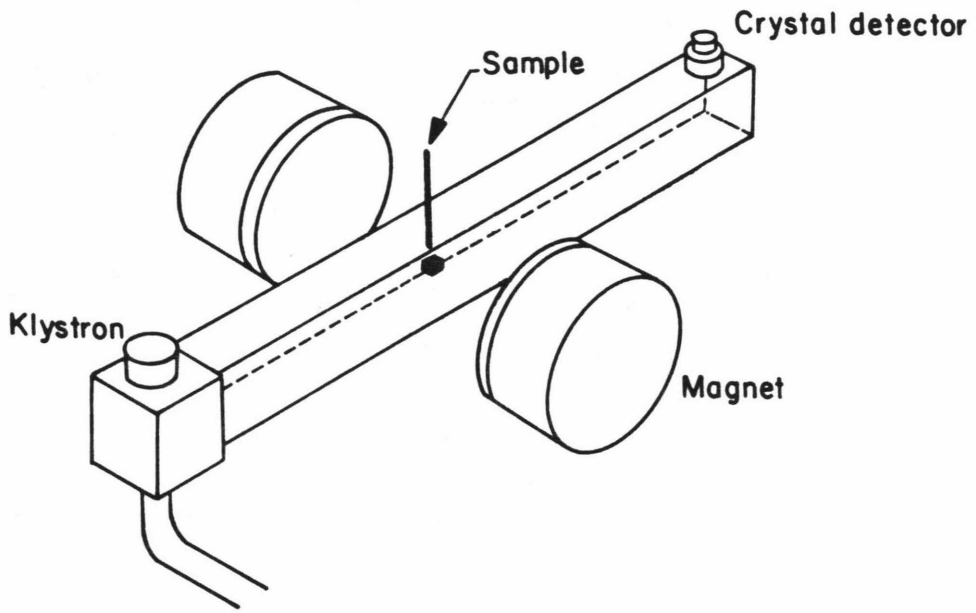

ESR Spectrometer

Figure I-1. Diagram of ESR spectrometer showing field generating magnets, Klystron microwave source and detector.

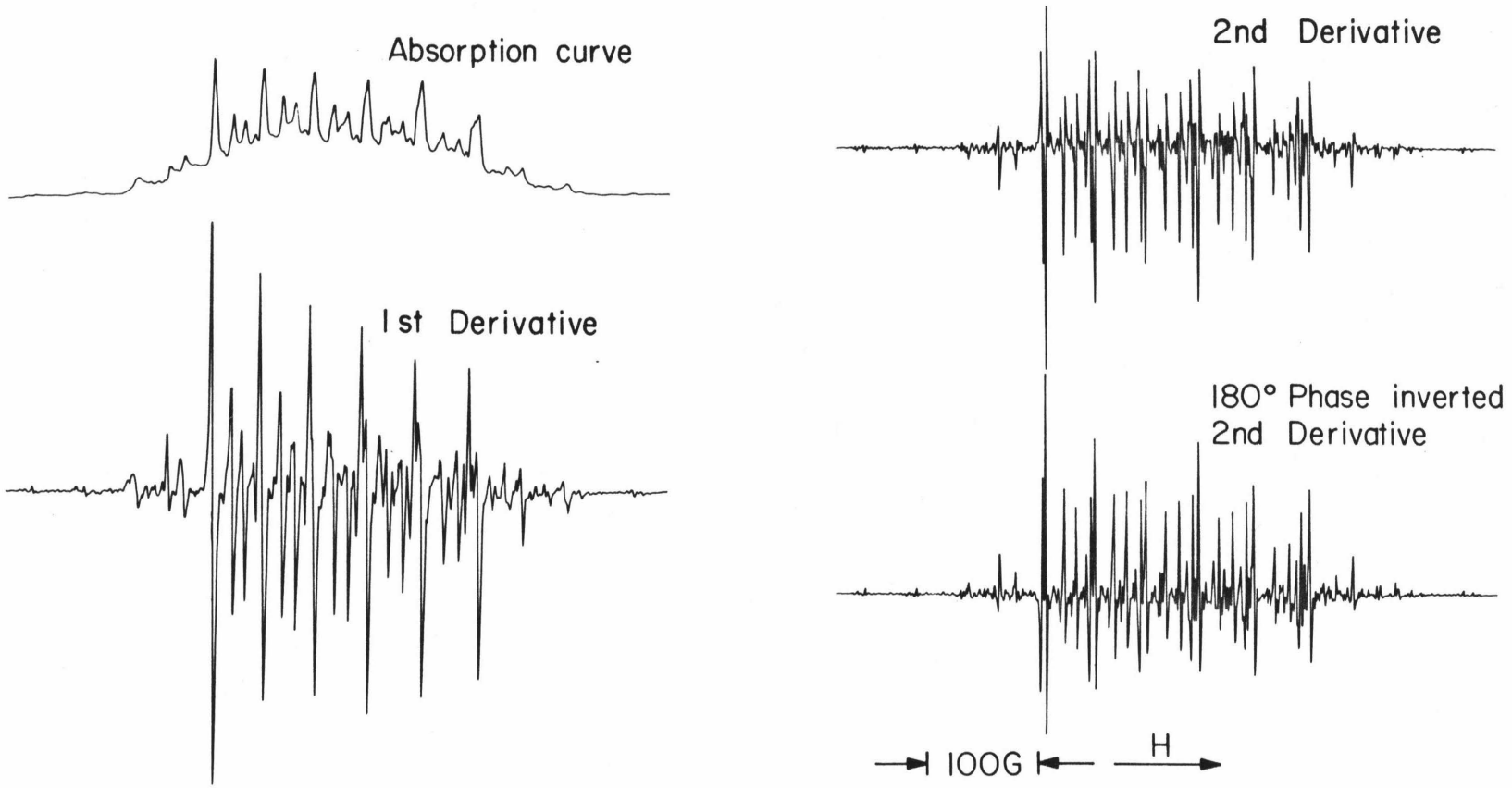

Figure I-2. Raw absorption curve, first and second derivative, and 180° phase inverted second derivative powder spectra of Mn^{2+} in calcite. The ESR spectrometer used in this study was equipped to detect the 180° phase inverted second derivative spectrum. Magnetic field increases to the right; 100 gauss indicated for scale.

$$H = g\beta \vec{H}\cdot\vec{S} + D\left[S_r^2 - \frac{1}{3}S(S+1)\right]$$
$$+ \frac{F}{180}\left[35\,S_r^4 - 30\,S(S+1)S_r^2 + 25\,S_r^2 - 6S(S+1) + 3S^2(S+1)^2\right]$$
$$+ A\,\vec{S}\cdot\vec{I} - \gamma\beta_N\,\vec{H}\cdot\vec{I} \qquad \text{(I-2)}$$

where g is the electron g-value, and β and β_N are the electronic and nuclear Bohr magnetons, respectively. $\vec{H}$ is the applied external magnetic field, $\vec{S}$ is the electron spin vector, and r refers to the crystal C axis of calcite; D and F denote the axial and cubic crystal field splitting parameters, respectively, A is the nuclear hyperfine coupling constant of manganese, $\vec{I}$ is the nuclear spin vector, and γ is the gyromagnetic ratio. For Mn^{2+} there are five unpaired d electrons (total electron spin S=5/2), and the interaction of these electrons with the nuclear spin of ^{55}Mn (I=5/2) will result in a total of (2S+1)(2I+1)=36 energy levels. Only 30 transitions between these energy levels are allowed because of the $\Delta M_s = \pm 1$ and $\Delta m_I = 0$ selection rules:

$$M_s = \pm 5/2 \rightleftarrows \pm 3/2,\ \pm 3/2 \rightleftarrows \pm 1/2,\ \pm 1/2 \rightleftarrows \pm 1/2,$$

and

$$m_I = \pm 5/2 \rightleftarrows \pm 5/2,\ \pm 3/2 \rightleftarrows \pm 3/2,\ \pm 1/2 \rightleftarrows \pm 1/2,$$

where M_s and m_I are the electronic and nuclear magnetic quantum number, respectively, with the external magnetic field as the axis of quantization. The resonance field positions for the 30 allowed transitions calculated from Eq. I-2 using perturbation theory up to third order (Tsay et al., 1972; Blanchard and Chasteen, 1976) as a function of an angle (θ) between the crystal C axis and the external magnetic field become

$$H(\theta) = H_o - \frac{1}{2}D(2M_S-1)\left[3\left(\frac{g_{\parallel}^2}{g^2}\right)\cos^2\theta - 1\right]$$

$$+ \frac{D^2}{2H_o}\left(\frac{g_{\parallel}^2 g_{\perp}^2}{g^4}\right)\cos^2\theta \sin^2\theta \left[4S(S+1) - 24 M_s(M_s-1)-9\right],$$

$$- \frac{D^2}{8H_o}\left(\frac{g_{\perp}^4}{g^4}\right)\sin^4\theta \left[2S(S+1) - 6M_s(M_s-1)-3\right]$$

$$- \frac{F}{144}\left[35\left(\frac{g_{\parallel}^4}{g^4}\right)\cos^4\theta - 30\left(\frac{g_{\parallel}^2}{g^2}\right)\cos^2\theta +3\right]$$

$$X \left[14 M_s^3 - 21 M_s^2 + (19 - 6S(S+1))M_s\right.$$

$$\left. + 3S(S+1)-6\right]$$

$$- KM_I - \left(\frac{B^2 g_{\perp}^2}{4H_o g^2}\right)\left(\frac{A^2 g_{\parallel}^2 + K^2 g^2}{K^2 g^2}\right)\left[I(I+1) + m_I(2M_S - 1 - m_I)\right]$$

$$- \frac{D^2 A m_I}{8H_o^2}\left(\frac{g_{\parallel}}{g}\left\{\left(\frac{g_{\parallel}^2 g_{\perp}^2}{g^4}\right)\sin^2 2\theta \left[3M_s(M_s-1)-2S(S+1)\right.\right.\right.$$

$$\left.\left. - \frac{[S(S+1)]^2}{M_s(M_s-1)}\right]\right.$$

$$\left. + \left(\frac{g_{\perp}^4}{g^4}\right)\sin^4\theta\left[3\left(2M_s^2 - 2M_s^2 + 1\right) - 2S(S+1)\right]\right\}\Bigg) \qquad \text{(I-3)}$$

where D (gauss) = D' (wave number)/$g\beta$, F = F'/$g\beta$,

A = A'/$g\beta$, B = B'/$g\beta$, K = K'/$g\beta$, $(K'g)^2 = (A'g_{\parallel}\cos\theta)^2$

+ $(B'g_{\perp}\sin\theta)^2$, $g^2 = (g_{\parallel}\cos\theta)^2 + (g_{\perp}\sin\theta)^2$ and $H_o = h\nu/g\beta$.

A and B are the nuclear hyperfine coupling constants measured with the external magnetic field parallel and perpendicular to the crystal C axis, respectively, h is Planck's constant, ν is the microwave frequency,

H_0 is the magnetic field, and $g_{\parallel}$ and $g_{\perp}$ are the parallel and perpendicular g-values, respectively.

The ESR spectrum observed for Mn^{2+} in a polycrystalline or powdered sample as shown in Fig. I-2 is due to the superposition of the individual, angularly dependent resonances arising from randomly oriented Mn^{2+} centers. Since the absorption intensity has a strong angular dependence, only those centers which are aligned along certain favorable directions relative to the magnetic field will contribute substantially to the resultant ESR spectrum of such a sample. For Mn^{2+} in calcite the favorable directions occur at $\theta = 90^0$ and $\theta = 43^0$ (Bleaney and Rubins, 1961; Tsay et al., 1972). Thus the predominant spectral features seen in the powder pattern of Mn^{2+} can be analyzed in detail from Eq. (I-3). By fitting the observed resonance positions with the calculated ones, the spin Hamiltonian parameters can be obtained with certainty from detailed analyses of powder patterns. The separation between the two extreme resonance positions that occur at $\theta = 90^0$ (low field peak) and $\theta = 43^0$ (high field peak) for each hyperfine component can be calculated from Eq. (I-3) and is found to be (Blanchard and Chasteen, 1976)

$$\Delta H = (50\ D^2/9\ H_0)\ (1 - (55\ A\ m_I/\ 9\ H_0)). \qquad (I\text{-}4)$$

From Eq. (I-4), an increase in ΔH with increasing D is predicted. Also, due to the change in sign (from positive to negative) of m_I in going from the low field to the high field components, ΔH will be greater for the latter.

The ESR spectra presented in Chapter 3 were recorded, at room temperature, on a Varian E-line Century Series spectrometer operating at X-band frequency (9.1-9.5 GHz) and employing 100 KH_z field modulation.

The spectrometer was equipped to detect the 180° phase inverted second derivative spectrum (see Fig. I-2) of the ESR absorption. This was done by operating the high frequency module in the second harmonic mode and appropriately adjusting the reference phase. In the past, the second derivative ESR method was used as a means of reducing effective linewidth, investigating lineshape (Allen et al., 1964) and studying relaxation processes (Hyde and Thomas, 1974). Here we have applied the approach as a means of eliminating the broad, steep background signal as well as of revealing the resonance positions.

The g-values were determined by comparison with the resonance position of 0.1% DPPH (diphenlylpicrylhydrazyl) dispersed in solid KCl. A ZnS sample containing Mn^{2+} was used to calibrate the linewidth, resonance field and nuclear hyperfine coupling constant of Mn^{2} in carbonate minerals. The gain, modulation amplitude and microwave power were appropriately adjusted well below saturation and distortion.

All of the spectra presented here were made on powder samples. Most samples of Eniwetok limestone consisted of unconsolidated fine fragments, or were easily friable and could be directly placed into 4 mm diameter fused silica ESR tubes. Several samples required slight grinding with mortar and pestle. To test the effect of such grinding, an aliquot of an unconsolidated sample was prepared in this manner; its ESR spectrum was indistinguishable from that of the unground sample. The single crystal calcite samples were also powdered.

References

Abragam, A. and B. Bleaney, Electron Paramagnetic Resonance of Transition Ions , Clarendon Press, Oxford, 1970.

Allen, L. D., H. M. Gladney and S. H. Glarum, Resolution enhancement for spectra of chemical and physical interest, J. Chem. Phys., 40, 3135-3141, 1964.

Blanchard, S. C. and N. D. Chasteen, Electron paramagnetic resonance spectrum of a sea shell, Mytillus edulis, J. Phys. Chem., 80, 1362-1367, 1976.

Bleaney, B. and R. S. Rubins, Explanation of some forbidden transitions in paramagnetic resonance, Proc. Phys. Soc. London, 77, 103-112, 1961.

Hurd, F. K., M. Sachs and W. D. Hershberger, Paramagnetic resonance absorption of Mn^{++} in single crystals of $CaCO_3$, Phys. Rev., 93, 373-380, 1954.

Hyde, J. S. and D. D. Thomas, New EPR methods for the study of very slow motion: application to spin-labeled hemoglobin, Ann. N.Y. Acad. Sci., 222, 680-692, 1974.

Tsay, F., S. L. Manatt and S. I. Chan, Electron spin resonance of manganous ions in frozen methanol solution, Chem. Phys. Lett., 17, 223-226, 1972.

APPENDIX II

X-RAY DIFFRACTION EXPERIMENTAL PROCEDURE

The X-ray powder diffraction method, used in peak broadening analyses and calcite concentration determinations described in Chapters 4 and 5, respectively, is detailed in this appendix.

All samples, i.e., coral core and single and polycrystalline calcite and aragonite, were treated in a uniform fashion. First, the samples were ground, in methyl alcohol, in an agate mortar until powdered. The effect of grinding on the X-ray results (specifically, on the peak broadening measurements) was investigated by comparing spectra of several aliquots of a particular coral sample, one of which was not ground at all, and two others requiring different amounts of grinding; there was no measurable difference in broadening between the three samples. The sample powders were then sieved to pass through a 325, but not a 400 mesh cloth, i.e., a standard size fraction between 38 and 43 microns was obtained. The sieving procedure did not appear to preferentially concentrate any phases, since spectra taken before and after show the same calcite to aragonite and high to low magnesium calcite ratios. Sample powders were then mixed with approximately 9 mg of a silicon powder internal standard (N.B.S. certified 99.9% pure), moistened with methyl alcohol, and compacted into 1 mm deep lexan sample holders with an approximate capacity of 0.07 cc.

The X-ray powder diffractometer scans were obtained on a Norelco

type 12045 B-3 unit operating at 45 Kv, 20 ma, and using nickel filtered copper Kα radiation. A collimating slit of 1° and receiving slit of 0.006° were used. The counting rate was 500 counts per second and the scan speed was 0.25° 2θ per minute. A narrow receiving slit and slow scan speeds were chosen in order to allow resolution of the high and low magnesium calcite peaks and accurate determinations of peak widths. Spectra were obtained on a Leeds and Northrop chart recorder, Speedomax G model. Spectral analyses are described in Chapters 4 and 5.